

REPORT DOCUMENTATION PAGE			Form Approved OASD No. 0704-0188	
<small>Public reporting burden for this collection of information is estimated to average 1 hour per response, including the time for reviewing instructions, searching existing data sources, gathering and maintaining the data needed, and completing and reviewing the collection of information. Send comments regarding this burden estimate or any other aspect of this collection of information, including suggestions for reducing this burden, to Washington Headquarters Services, Directorate for Information Operations and Reports, 1215 Jefferson Davis Highway, Suite 1204, Arlington, VA 22202-4302, and to the Office of Management and Budget, Paperwork Reduction Project (0704-0188), Washington, DC 20503.</small>				
1. AGENCY USE ONLY (Leave blank)		2. REPORT DATE 9/17/01		3. REPORT TYPE AND DATES COVERED Final Report (06/14/99-06/13/01)
4. TITLE AND SUBTITLE The Effect of Curvature on the Evolution of a Boundary Layer Subjected to a Strong Adverse Pressure Gradient				5. FUNDING NUMBERS N00014-99-1-0883
6. AUTHOR(S) Professor Israel J. Wygnanski				
7. PERFORMING ORGANIZATION NAME(S) AND ADDRESS(ES) Department of Aerospace and Mechanical Engineering The College of Engineering and Mines The University of Arizona Tucson, AZ 85721				8. PERFORMING ORGANIZATION REPORT NUMBER
9. SPONSORING / MONITORING AGENCY NAME(S) AND ADDRESS(ES) Office of Naval Research Ballston Centre Tower One 800 North Quincy Street Arlington, VA 22217-5660				10. SPONSORING / MONITORING AGENCY REPORT NUMBER
11. SUPPLEMENTARY NOTES				
12a. DISTRIBUTION / AVAILABILITY STATEMENT  Approved for public release				12b. DISTRIBUTION CODE
13. ABSTRACT (Maximum 200 words)  Negligible wall shear stress provides the criterion that minimizes the distance over which boundary layer can decelerate without separating from the surface. Over the past few years, we have been carefully investigating the boundary layer that is continuously maintained on the verge of separation, without actually being allowed to separate [1]. The experimental facility that was used consists of a contraction, a constant area throat, and a two-dimensional variable geometry expansion inserted into the 2' by 3' test section of a low speed wind tunnel (figure 1). The expansion is constructed of Lexan supported by electric actuators mounted on gimbals and capable of distorting the surface under computer control. The surface geometry can vary over a wide range of pressure gradients and streamline curvature. The transition between the throat and the test surface is accomplished by means of a circular cylinder to which the lexan surface is attached, thereby establishing the initial slope of the test surface. The side-wall boundary layers were removed by using suction and <i>the measurements were made on the boundary layer developing on the curved surface.</i>				
14. SUBJECT TERMS				20010921 107
				15. NUMBER OF PAGES 3 + Attachments
				16. PRICE CODE
17. SECURITY CLASSIFICATION OF REPORT UNCLASSIFIED	18. SECURITY CLASSIFICATION OF THIS PAGE UNCLASSIFIED	19. SECURITY CLASSIFICATION OF ABSTRACT UNCLASSIFIED	20. LIMITATION OF ABSTRACT UL	

# THE EFFECT OF CURVATURE ON THE EVOLUTION OF A BOUNDARY LAYER SUBJECTED TO A STRONG ADVERSE PRESSURE GRADIENT

Final Report Submitted to ONR on Project N00014-99-1-0883

I. Wygnanski,

Department of Aerospace and Mechanical Engineering, The University of Arizona.

August 27, 2001

## OVERVIEW

Negligible wall shear stress provides the criterion that minimizes the distance over which boundary layer can decelerate without separating from the surface. Over the past few years, we have been carefully investigating the boundary layer that is continuously maintained on the verge of separation, without actually being allowed to separate [1]. The experimental facility that was used consists of a contraction, a constant area throat, and a two-dimensional variable geometry expansion inserted into the 2' by 3' test section of a low speed wind tunnel (figure 1). The expansion is constructed of Lexan supported by electric actuators mounted on gimbals and capable of distorting the surface under computer control. The surface geometry can vary over a wide range of pressure gradients and streamline curvature. The transition between the throat and the test surface is accomplished by means of a circular cylinder to which the lexan surface is attached, thereby establishing the initial slope of the test surface. The side-wall boundary layers were removed by using suction and the measurements were made on the boundary layer developing on the curved surface.

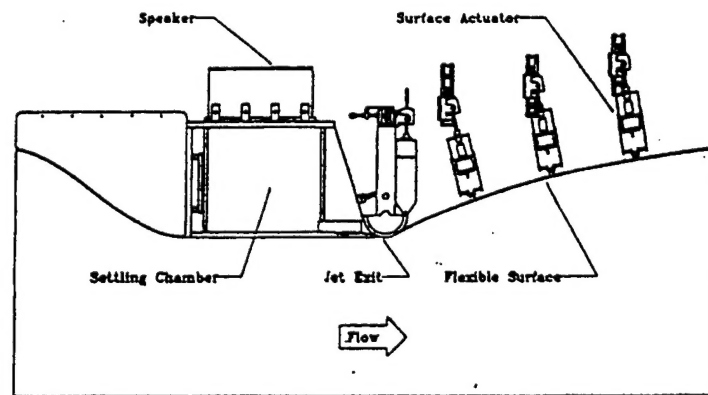


Figure 1. Experimental apparatus.

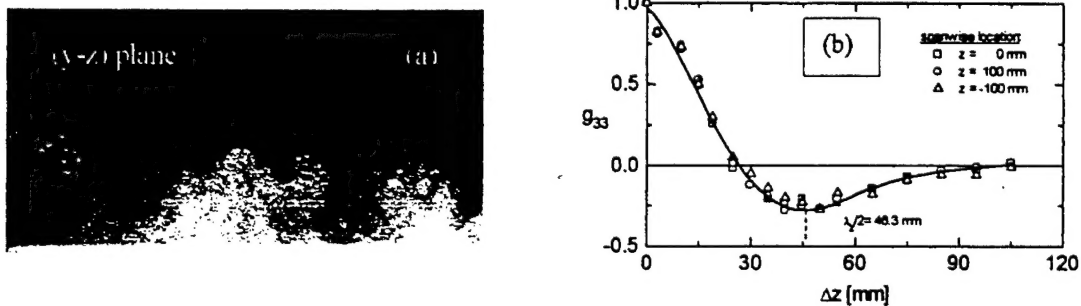
Although the proximity of the uncontrolled flow to separation was determined by trial and error, its compatibility with the two-dimensional boundary layer equations was verified. The experimental results that were accumulated over approximately five years were published in the *Journal of Fluid Mechanics* (See attachment 1.). The accumulated data contradicted past observations and pointed toward a lack of equilibrium between the turbulence and the mean motion. The scaling laws also differed and the observed boundary layer shape factor,  $H$ , was significantly larger than customarily found in flows that were about to separate. Special care had to be taken in validating these results, by using different measurement techniques (e.g. Hot wires and Laser Doppler Velocimeter), because they differ from other data reported in the literature. Most of these differences were finally attributed to surface curvature; therefore, data obtained on a flat surface in an adverse pressure gradient may be of limited practical value.

Another effect that is now attributed to curvature is the response of the flow to plane periodic excitation. In the absence of curvature (e.g. the mixing layer or the turbulent jet flowing over a flat plate) low level excitation increases the spreading rate of the flow and its turbulence intensity. In the present case, external excitation increased  $C_f$  while concomitantly reducing the boundary layer thickness and most significantly the overall turbulence level

(See figure 27 of reference 1-attached.). The understanding of these phenomena may come from a turbulent flow that is dominated by surface curvature [for example, the turbulent wall jet flowing outside a circular cylinder-references 2 & 3 (the latter is attached)]. This flow is susceptible to a centrifugal instability that generates streamwise vortices. The streamwise vortices compete with the spanwise vortices, associated with the spanwise mean vorticity. The latter may be generated through another instability mechanism (e.g. Kelvin-Helmholtz instability whenever the flow possesses an inflectional velocity profile like it does in the present case). The centrifugal instability reduces the spanwise coherence of the propagating large scale eddies and, as a consequence, increases the turbulent intensity. We now believe that plane periodic excitation suppresses the production of turbulence due to the centrifugal instability. Consequently the question arises, what mode of instability is most effective for the control of separation on a concave surface? Perhaps reinforcement of stationary streamwise vortices is preferred over the plane periodic excitation.

The first evidence of presence of the large-scale longitudinal vortices in a turbulent boundary layer along a concave wall was reported by Tani [4]. This finding was later confirmed by the experiment of So and Mellor [5]. They revealed a spanwise variation in the mean velocity that has a preferred wave number related to the Görtler-type of instability. An inviscid stability criterion [6] may be used to identify the boundary layers that are potentially unstable and might generate large-scale streamwise vortices, regardless of the state of the flow (i.e. whether it is laminar or turbulent). For example, the centrifugal instability affects the outer part of the wall jet that adheres to a convex surface. This flow was the first to be investigated because the radius of curvature is constant. It was obvious that it is dominated by curvature. The jet spreads outward much more rapidly than over a corresponding flat surface, and at some locations, the difference in the rate of spread of the two flows might approach an order of magnitude [2 & 3]). Flow visualization (figure 2a), using smoke as tracer particles and a laser-sheet that illuminated the plane normal to the flow direction, clearly revealed the existence of streamwise eddies. The scale of these eddies was in agreement with the scales deduced from the  $g_{33}$  correlations (figure 2b). These measurements were made using two x-wire probes that were separated by a spanwise distance ( $\Delta z$ ) at azimuthal angle

Figure 2. (a) Flow visualization and, (b) cross correlation at  $(\theta - \theta_0) = 160^\circ$ .



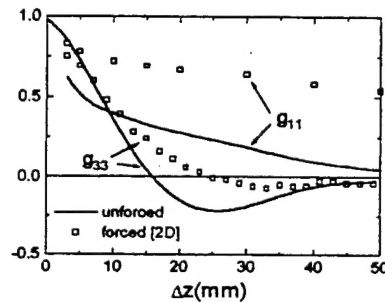
$\theta - \theta_0 = 160^\circ$ , representing the distance from the virtual origin of the jet in this case. The measurements were repeated at various spanwise locations in order to ensure that the existence of streamwise vortices was not associated with any imperfections in the apparatus. The correlations proved to be independent of  $z$ . A simple traverse measuring the  $u_z$ -component of velocity (using an LDA) across the span indicated a periodicity that also agreed well with the correlation measurements obtained by hot wire anemometers. Figure 2b also illustrates how the spanwise wavelength of the longitudinal vortices was determined. When the procedure was repeated at various distances from the nozzle, corresponding to azimuthal angles along the cylinder of  $40^\circ < (\theta - \theta_0) < 180^\circ$ , it became clear that the wave length of the streamwise vortices,  $\lambda_z$  increased with  $\theta$  (See figure 18 in reference 3-attached.). This observation suggests that  $\lambda_z \approx 2 \cdot Y_2$ , which is marked by figure 18, reference 3; scaled with the local width of the flow over the entire range of parameters considered, was contrary to the fundamental assumptions used in attachment [4] where  $\lambda_z$  was assumed to be a constant.

Cross correlation measurements in the presence and the absence of plane excitation emanating from the nozzle revealed a competition between these two modes of instability (figure 3). The  $g_{11}$  correlation shown in the figure

refers to a normalized product of the streamwise velocity component,  $u'_s$  while the  $g_{33}$  correlation refers to the product of the spanwise velocity component. In the example shown, the natural  $g_{33}$  correlation attained a minimum value of  $-0.21$ , when the spanwise separation between the probes was approximately  $25\text{mm}$ . It implies that the average spanwise dimension of a counter rotating pair of the streamwise vortices is  $\approx 50\text{mm}$  at that downstream location. Two-dimensional excitation had a tremendous impact on the three-dimensionality of the flow. The  $g_{11}$  correlation at  $\Delta z = 50\text{mm}$  increased 10 fold (from approximately 0.05 to 0.5). The negative  $g_{33}$  decreased by a factor of 4 and its spanwise location increased to  $\Delta z = 35\text{mm}$ . This suggests a diminution in the strength and coherence of the streamwise vortices and a slight increase in their scale. These results provide justification for the hypothesis of strong competition between two modes of instability observed in the forced turbulent boundary layer along the Stratford ramp.

Calculations have been carried out to evaluate the stability of the turbulent wall jet flowing over a circular

Figure 3. Cross correlation in the presence and the absence of plane excitation;  $\theta - \theta_s = 100^\circ$



cylinder with respect to the Gortler-type perturbations [reference 7 attached]. One assumes that the longitudinal vortices generated are a manifestation of a linear centrifugal instability of the mean velocity profile. It is assumed that the effect of the random (smaller scale) turbulence on these vortices is the same as that on the mean motion, therefore an eddy viscosity  $\nu_t$  was used in the analysis. The appropriate control parameter for this flow is  $Go = \varepsilon * Re_t$ , where  $\varepsilon = Y_2/R$  is the curvature parameter and  $Re_t = Y_2 U_{\infty} / \nu_t$  is the turbulent Reynolds number based on the local characteristic scales of the wall jet and the eddy viscosity that was evaluated from the mean momentum equation. Similar calculations were used to predict the possible generation of streamwise vortices in the turbulent boundary layer over the surface shown in figure 1. The report summing up these calculations is also attached [8]. Although these calculations were intended to support experimental evidence their validity is not certain. The calculations are clouded by not only by some questionable assumptions i.e., the eddy viscosity, but the dominance of the linear process for the streamwise vortices is in doubt (See the conclusions presented in reference 3.).

## CONCLUSIONS

The large coherent structures observed in turbulent shear flows such as the mixing layer, the wall jet, or the turbulent boundary layer in an adverse pressure gradient can be viewed as being the manifestations of the predominant instability modes of these flows. This point of view provides a basis for the enhancement of mixing, and control of separation by periodic excitation. The present data reveals that stationary, streamwise vortices generated by surface curvature can also be associated with stability considerations and in this case a centrifugal instability.

## REFERENCES

1. Elsberry, K. Loeffler, J. Zhou, M.D. and Wygnanski, I. An experimental study of a boundary layer that is maintained on the verge of separation, *J. Fluid Mech.* **423**, (2000), 227-261. **ATTACHMENT 1**
2. Neuendorf, R. and Wygnanski, I.: On a turbulent wall jet flowing over a circular cylinder, *J. Fluid Mech.*, **381** (1999), 1-25.
3. Neuendorf, R. Lourenco, L. and Wygnanski, I.: On large streamwise structures in a wall jet flowing over a circular cylinder, submitted for publication in *J. Fluid Mech.* **ATTACHMENT 2**
4. Tani, I.: Production of longitudinal vortices in the boundary layer along a concave wall, *J. Geophys. Res.* **67**, (1962), 3075-3081.
5. So, R. M. C. and Mellor, G. L.: Experiment on the turbulent boundary layers on a concave wall. *Aero. Q.* **26**, (1975), 25-40.
6. Floryan, J. M.: Gortler instability of boundary layers over concave and convex walls, *Phys. Fluids* **29**, (1986), 2380-2387.
7. Likhachev, O., Neuendorf, R. and Wygnanski, I.: On streamwise vortices in a turbulent wall jet that flows over a convex surface in *Phys. Fluids* **13**, (2001), 1822-1825. **ATTACHMENT 3**
8. Likhachev, O., Stability Analysis of laminar and turbulent boundary layer with streamwise curvature **ATTACHMENT 4**



# An experimental study of a boundary layer that is maintained on the verge of separation

By K. ELSBERRY<sup>†</sup>, J. LOEFFLER<sup>‡</sup>, M. D. ZHOU  
 AND I. WYGNANSKI<sup>¶</sup>

Department of Aerospace and Mechanical Engineering, University of Arizona,  
 Tucson, AZ, 85721, USA

(Received 27 April 1999 and in revised form 28 April 2000)

A boundary layer maintained as close as possible to separation over an extended distance was produced, in accordance with the concept of Stratford. The resulting layer was two-dimensional in the mean, had nearly a constant shape factor of 2.5 and approximately linear streamwise growth of its integral length scales. The flow exhibited a definite non-equilibrium character, indicated by the different scales required for collapse of the mean velocity and turbulence intensity profiles. It was also very sensitive to the thickness of the upstream boundary layer. External excitation was imposed for diagnostic purposes and as a tool for delaying separation. The oscillatory momentum level of  $c_{\mu} \approx 0.1\%$  was tested for its ability to increase the skin friction  $c_f$  at the prescribed geometry. Various frequencies, corresponding to the Strouhal number  $0.008 < f\theta_0/U_{ref} < 0.064$ , were used for the free stream reference velocity of  $U_{ref} = 15 \text{ m s}^{-1}$  and for two different inflow conditions. Notable increase (close to 60%) in  $c_f$  was observed at higher frequencies that did not undergo maximum amplification. The increase in  $c_f$  was accompanied by a reduction in the boundary layer thickness and in the shape factor  $H$ . The latter decreased in one case from 2.5 to 2.1. The overall turbulence level in the boundary layer decreased due to the addition of plane external perturbations.

## 1. Introduction

The behaviour of boundary layers subjected to severe adverse pressure gradient is of great technological interest. Adverse pressure gradients occur whenever a solid surface turns away from the mean flow direction, as it does near the trailing edges of airfoils or at the termination of streamlined bodies such as submarines or ships. Adverse pressure gradients also occur in diverging channels, exemplified in aeronautical applications by inlets to engines. It is generally desirable to minimize the distance over which the deceleration takes place but this desire is tempered by the requirement to avoid separation and flow reversal. For example, airfoil designers would like to minimize the length of the pressure recovery section in order to maximize the fraction of the airfoil chord that can sustain natural laminar flow. For streamlined bodies, a rapid truncation provides more useable volume per unit surface area and greater structural efficiency. For diffusers, a reduction in duct length reduces weight and lost volume.

Separation results in large total pressure losses, buffet, loss of lift and loss of control.

<sup>†</sup> Present Address: Raytheon Missile Systems Company, Tucson, AZ 85734-1337, USA.

<sup>‡</sup> Present Address: Eurocopter, Germany.

<sup>¶</sup> Also Lazarus Professor of Aerodynamics, Faculty of Engineering, University of Tel-Aviv.

It has to be avoided but so does a conservative, large and overweight design. These competing priorities have led several investigators to examine the largest adverse pressure gradient that can be sustained without causing separation. Stratford (1959a) proposed that a turbulent boundary layer providing a maximum rate of pressure recovery has to have a zero wall stress over its entire length. He began by conceptually dividing the velocity profile into two parts: an outer part, that merely loses dynamic head in direct proportion to the increase in static pressure, and an inner part that maintains an equilibrium between the transverse gradient of the shear stress and the stream-wise pressure gradient. The mixing length hypothesis was invoked as well as some assumptions about the general shape of the velocity profile in order to derive an equation for the pressure recovery that corresponds to an imminent, continuous separation. In Stratford (1959b) this analysis was backed by an experiment in which a stable turbulent boundary layer with a 'near zero skin friction' was generated. Stratford's experiment was limited by the available instrumentation (Pitot tubes) and was marred by a lack of two-dimensionality. The concept, however, led the way to a novel design of airfoils for high lift (Liebeck 1973) because it provides the maximum pressure rise that a boundary layer can sustain without separation, in the shortest possible distance.

Spangenberg, Rowland & Mease (1967) attempted to produce such a flow on a flat surface by using a vented wind-tunnel wall and an adjustable 'end-gate' at the end of their test section. Their results cast doubt on some of the theoretical claims of Stratford, particularly with regard to the existence of a region of linear variation of the dynamic head with increasing distance from the wall. Furthermore, they produced two very different sets of data with approximately the same pressure distribution suggesting that, in addition to factors usually considered, the inflow conditions influence the behaviour of the boundary layer near separation. Notably, the case with lower skin friction exhibited greater loss of mean kinetic energy.

Dengel & Fernholz (1990, hereafter referred to as DF) examined the sensitivity of a turbulent boundary layer near separation to small differences in pressure gradient by using the same technique as Spangenberg *et al.* (1967). Their measurements were carried out on a large cylinder thus reducing the difficulties associated with two-dimensionality. One of their tests generated a region where the boundary layer possessed a zero averaged skin friction. In this region, the flow reversed its direction next to the surface roughly 50% of the total time. Another experiment of note is by Skare & Krogstad (1994, hereafter referred to as SK) who concentrated on the equilibrium aspects of a boundary layer that is subjected to a severe adverse pressure gradient but does not approach separation. Their measured skin friction coefficient,  $c_f$ , in the region of interest was  $5.7 \times 10^{-4}$  and the shape factor of the boundary layer  $H = 2$ . It is worth noting that only Stratford made his measurements on the boundary layer evolving over the curved surface. There are many other experiments focusing on the process of separation (e.g. Perry & Schofield 1973; Simpson 1989; Patrick 1987) but they will not be discussed in the present context. The purpose of the research to be described is to consider the boundary layer that is maintained on the brink of separation without actually detaching fully from the surface over a significant distance or time. The measurements were conducted on a curved surface in parallel with numerical experiments of H. Fasel and closure models of C. Speziale in the hope that the data be used to validate models needed to simulate flows in large adverse pressure gradients.

All the experiments involving active control of separation were carried out on conventionally designed airfoils, wings or diffusers. Separation occurred naturally at

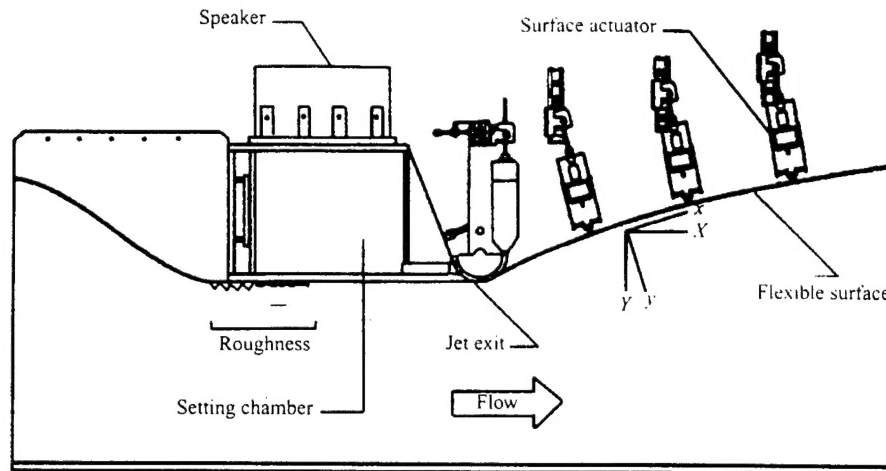


FIGURE 1. Experimental facility.

off-design conditions due to excessive incidence, flap deflections, too low Reynolds numbers or too high Mach Numbers. Active flow control (AFC, Wygnanski 1997) enabled the flow remain attached beyond the conventional design limits of the prescribed configuration and thus improve the performance.

A historical perspective on many aspects of flow control is documented in the books edited by Lachmann (1961) and written by Chang (1976). More recent surveys on passive and active flow management methods were carried out by Gad el Hak & Bushnell (1991) and by Fernholz (1993). Both articles discuss active and passive management techniques of turbulent shear flows and their respective merits. All, however, take the design of a wing, an airfoil or a streamlined body, that was based on a steady flow assumption as given. They reveal, therefore, that active flow control is only a concept but not a technology because it does not provide an engineer with integrated design criteria that optimize the shape of a streamlined body with built-in actuators for prescribed actuation levels and frequencies.

The present experiment also describes the effects of periodic excitation on the boundary layer parameters such as skin friction and shape factor under prescribed boundary and inflow conditions. It is but a first step in the process of determining the optimum shape of the surface that is capable of maintaining a boundary layer on the brink of separation for a prescribed level of periodic excitation. In the next step the original parameters of the flow will be restored (while maintaining the external actuation) by changing and adjusting the geometry of the surface.

## 2. Apparatus and experimental conditions

The experimental facility consists of a two-dimensional contraction, a constant-area throat, and a two-dimensional variable-geometry expansion inserted into the 0.61 m by 0.92 m test section of a closed-loop, low speed wind tunnel at the University of Arizona (figure 1). The expansion is constructed of 3.2 mm thick Lexan and is supported by six electric actuators. The actuators are driven by step motors via lead-screws. This allows precise computer controlled motion of the surface. The gimbals allow the surface geometry to be varied over very wide limits in both the streamwise and cross-stream directions.

The transition between the throat and the test surface is accomplished by means of a 15.24 cm diameter cylinder. The cylinder is also provided with an electric actuator that enables the initial slope of the test surface to be changed. This cylinder causes the form of the adverse pressure gradient to deviate somewhat from the ideal Stratford pressure distribution, which is discontinuous at the initiation of the adverse pressure gradient. The present geometry is, however, more representative of likely applications. The shape of the flexible surface is approximately described by the following:

$$\text{case A} \quad Y = 0.39696 + 0.38091X - 8.925 \times 10^{-5}X^2 - 6.8277 \times 10^{-6}X^3,$$

where  $X$  and  $Y$  are defined in this context as being parallel and normal to the floor of the tunnel, respectively, and are measured from the beginning of the flexible surface. For all measurements reported here the velocity in the tunnel was set at  $U_{ref} = 15 \text{ ms}^{-1}$ , measured by a Pitot tube in the constant-area throat section of the test apparatus (figure 1) and sufficiently far upstream of the divergence. Since the flow accelerated near the initiation of the divergence, the inflow conditions were specified at a location at which the free stream velocity (in the absence of excitation) reached its maximum value,  $U_0$  (see §4). Streamline coordinates ( $x, y$ ) are used to analyse the data; thus the initial momentum thickness of the boundary layer

$$\theta_0 = \int \frac{U}{U_0} \left(1 - \frac{U}{U_0}\right) dy$$

measured at the  $x$ -location where the free-stream velocity was  $U_0$ , was 2.3 mm. Many distances in the direction of streaming are referred to the virtual origin of the flow,  $x_0$ , where the extrapolated curve of the local momentum thickness,  $\theta$ , would have vanished.

The significance of changing the inflow conditions on the evolution of the ensuing boundary layer was also assessed in this experiment. Roughness strips glued to the narrow, straight surface upstream of the divergent section (figure 1) changed  $\theta_0$  from 2.3 mm to 4.5 mm. Thereafter the shape of the divergent surface had to be adjusted slightly to maintain the flow on the verge of continuous separation. The shape of the new configuration is

$$\text{case B} \quad Y = 0.35189 + 0.40782X - 1.33 \times 10^{-3}X^2 - 1.03879 \times 10^{-7}X^3.$$

All the data required for making the balance of turbulent energy were for case A. The data were generally acquired at a frequency of 2 KHz but for assessing the dissipation the sampling rate this was increased to 20 KHz.

Preliminary work indicated that sidewall interference was likely to pose a significant difficulty because the interaction of the boundary layer on the sidewalls with the boundary layer on the test surface causes premature separation. This was initially avoided by adding fences to both sides of the test surface, thereby initiating a fresh boundary layer at the leading edge of the fence. Although this provided a solution to the problem, it did not ensure success at various inflow conditions. Therefore a narrow suction slot was cut into each sidewall, at the start of the expansion section and was connected to an independent low pressure source. This arrangement allowed the sidewall boundary layers to be removed, maintaining two-dimensional flow even at the most distant measuring location downstream. This was checked in several ways; by using multiple static pressure taps distributed along the span, by measurements of  $\overline{W}$  and measurements of  $\overline{u'w'}$ , and by integration of the two-dimensional boundary layer equations to obtain the value of  $\overline{u'v'}$  that agrees with direct measurement. The mean value of the spanwise component of velocity did not exceed 1% of the

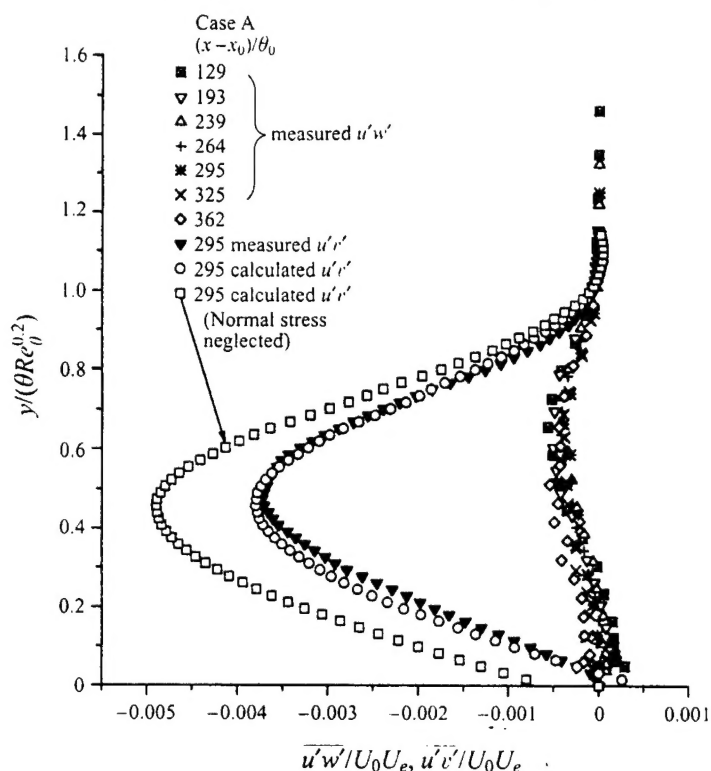


FIGURE 2. Spanwise and longitudinal Reynolds stresses for different downstream locations.

streamwise mean velocity at any measured location. Given the uncertainty in the probe angle with respect to the mean flow it was concluded that the spanwise mean velocity component was essentially zero. The value of the spanwise Reynolds stress,  $\overline{u'w'}$ , is presented in figure 2. The peak of this quantity is more than one order of magnitude smaller than the peak of the corresponding longitudinal quantity in spite of the presence of streamwise vortices arising from the concave curvature of the surface. Finally, the Reynolds stress calculated by integrating the two-dimensional momentum equation (5.2), using the measured streamwise component of velocity  $U$ , the continuity equation  $V(y) = -\int_0^y (\partial U / \partial x) dy$ , and the measured normal stresses  $(u'^2 - v'^2)$ , agrees very well with the directly measured Reynolds stress (figure 2). All these tests confirm the two-dimensionality of the flow and prove the reliability of the measurements.

The pressure distribution was initially obtained by increasing the divergence of the surface until any further increase led to total separation. At each stage of increased divergence it was necessary to determine the asymptotic value of the sidewall suction. This was done by placing a hot-wire probe at the most downstream location used in the experiment and varying the suction until further increases did not alter the observed velocity. Any attempt to increase the rate of pressure recovery beyond this value was unsuccessful regardless of the level of suction from the sidewalls. Tufts glued to the surface of the ramp indicated that periodic back-flow was present.

The high turbulence intensity and the sensitivity of the flow to external disturbances demanded a special support for the probe holders used in the study. The support must have a high stiffness to mass ratio, minimal blockage, and the ability to vary the



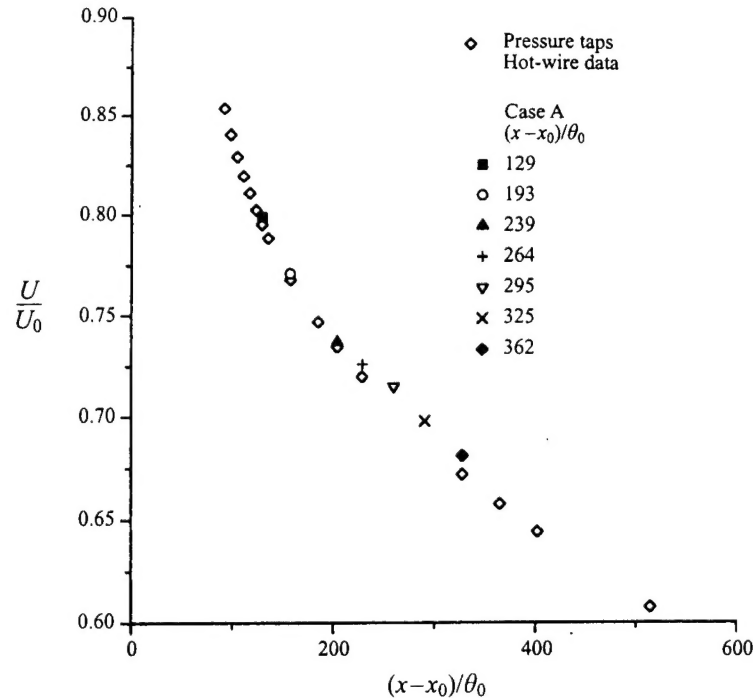


FIGURE 3. Deceleration of the flow for the thin inflow condition (case A).

probe angle (to calibrate x-wire probes and to allow for wall curvature). The support is of an open, girder construction originally proposed by D. W. Bechert (private communication) and it is essentially immune to aeroelastic vibrations.

Previous experimental observations (Simpson 1989) suggested that prior to complete separation from the surface, there is a region where the mean flow still proceeds downstream but in which the turbulent fluctuations produce periods of reversed flow. The fraction of time that the flow proceeds upstream in a region close to the wall,  $\gamma$ , has been used to define the mean separation location. A common formulation is that incipient detachment has occurred when the probabilities of forward and reverse flow are equal (Simpson 1989). This definition was deemed most appropriate when attempting to reproduce a boundary layer matching the Stratford concept. However, it proved to be unworkable because the flow is sensitive to random perturbations in the laboratory and could detach itself suddenly without apparent cause. We had therefore to content ourselves with a flow that was stable but was close enough to separation. The proximity of the flow to separation was therefore determined from the mean velocity profiles plotted in wall coordinates.

The deceleration of the flow for the thin inflow condition (case A) is shown in figure 3. The close agreement between the velocity inferred from the pressure distribution and the external velocity measured with a hot wire indicates that the boundary layer approximation can be applied.

Harmonic oscillations were introduced to the flow field through a thin slot close to the initiation of the adverse pressure gradient. Although these oscillations originated from a loudspeaker located on top of the settling chamber, they emerged as vortical

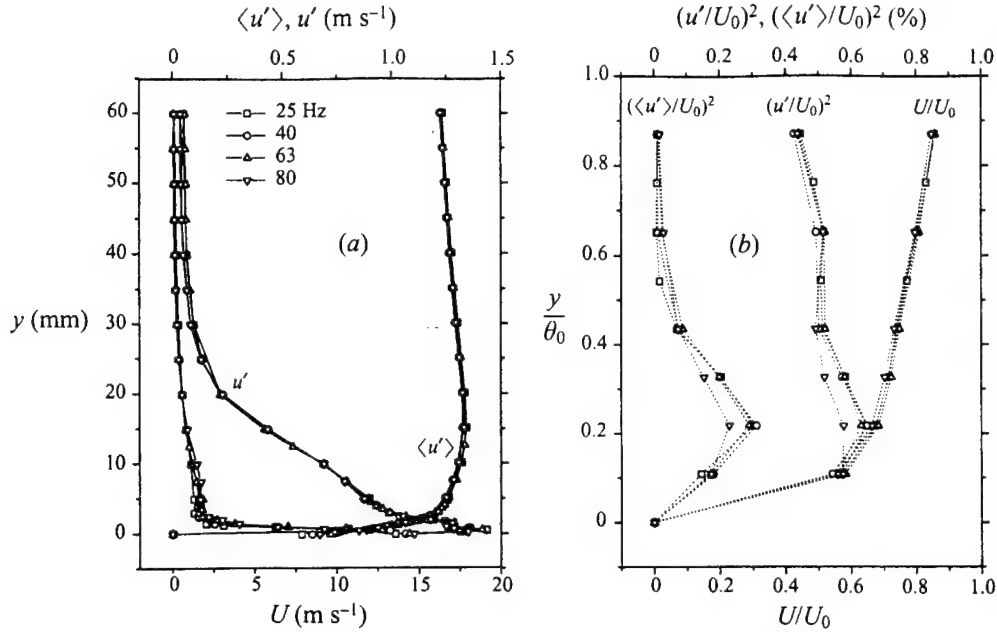


FIGURE 4. The effect of external excitation on the inflow conditions.

perturbations in the flow. All efforts were made to seal the settling chamber and provide two-dimensional perturbations with zero net mass flux.

The inflow conditions for all forcing frequencies are shown in figure 4. For the determination of the forcing level, the distribution of the phase-locked and ensemble-averaged r.m.s. value of the streamwise velocity component was integrated with respect to the normal coordinate. The integral value was then normalized by the momentum deficit at this location

$$c_\mu = \frac{\int_0^\infty \overline{u'^2} dy}{U_0^2 \theta_0}. \quad (2.1)$$

A value of  $c_\mu \approx 0.1\%$  was achieved for all forcing frequencies regardless of the differences in the detailed distribution of the phased-locked amplitudes near the slot (figure 4b). The value of  $\theta_0$  near the slot was obtained from extrapolation of the momentum thickness, measured while the flow was not forced, to the location at which the free-stream velocity attained its maximum value,  $U_0$  (this gave  $\theta_0 = 2.3$  mm for case A and 4.5 mm for case B).

### 3. Instrumentation and data reliability

The primary instrument used for the study was the constant-temperature hot-wire anemometer (HW). Single, normal wires and x-wire arrays were used and the data were sampled at 2 KHz except for dissipation measurements where the sampling rate was increased to 20 KHz. This instrument remains the best choice when a statistical description of the flow is required, in spite of the availability of a laser Doppler velocimeter (LDV) and a particle image velocimeter (PIV). The overall reliability of the hot-wire data was demonstrated in figure 2 where balance of the momentum

equation provided a good comparison between the measured and the calculated Reynolds stress. However, the instantaneous velocity vector can deviate significantly from the mean flow direction close to the surface. Special care was therefore taken with the calibration of the x-probes that measured the  $V$  component of velocity. In particular, it was desirable to extend the calibration over the full effective range of a  $45^\circ$  x-wire sensor (i.e. to  $\pm 40^\circ$ ). In order to obtain acceptable accuracy a look-up table approach, derived from Leupetow, Bruer & Haritonidis (1988) was adopted for calibrating the x-wire. This technique involves the use of successive polynomial fits to the raw calibration data in order to characterize the  $U$  and  $V$  velocity components in terms of the two wire voltages. One may also compare the results obtained with an x-wire to results obtained by a single-wire probe for the streamwise velocity component. The agreement between the two sets of data was excellent, providing some validation of x-wire calibration technique.

Finally, the normally operated stationary hot-wire probe cannot recognize flow reversal and it rectifies the voltage output. The calibration technique allows points exceeding the angular limits of the calibration to be readily identified. The fraction of time that the angle between the instantaneous velocity vector and the hot wire exceeded the calibration limits is negligible provided  $y/\theta \geq 0.25$ . This fraction increases rapidly below  $y/\theta = 0.25$  but at this level the hot-wire probe remains within the calibration limits 93% of the time. Although it is clear that the region of uncertainty is so thin ( $y/\theta < 0.25$ ) that it is insignificant in the overall momentum budget and scaling considerations, a detailed comparison between data obtained with a single hot wire and an LDV was made. A single wire that was parallel to the surface was chosen for the test because of its small size and its ability to be brought very close to the solid surface. Simultaneous measurements of mean velocity with both instruments validated the data taken earlier with hot wires only (figure 5). There is an excellent agreement between the mean velocity profiles acquired with the LDV and the hot wire even in regions that are very close to the wall. The LDV was able to provide sufficiently accurate, high-resolution data in the linear region next to the surface (figure 5a), from which the friction velocity,  $u_\tau = \sqrt{\tau_w/\rho}$ , could be estimated ( $u_\tau^2 = \nu \partial U / \partial y$ ). However, the value of  $u_\tau$  obtained in this way was somewhat higher (by approximately 10%) than the one obtained by using the Clauser method (i.e. the universal, logarithmic law of the wall). Using the friction velocity estimated from figure 5 the short logarithmic relation fitting the data is  $u^+ = 5.5 \log y^+ + 2$ . The agreement between the hot wire and the LDV data when both are plotted in wall variables (see figure 5b) is impressive in view of the anticipated adverse effects resulting from hot-wire rectification. The distributions of the streamwise component of the velocity fluctuations are plotted in figure 5(c). The r.m.s. values measured by the LDV system are higher in general, since flow reversal is now taken into account. Surprisingly however, the differences are not large, indicating that the flow reverses relatively rarely. The comparison between the hot-wire data and the LDV was repeated at five different streamwise locations with equally good results.

The surface pressure distribution was obtained by connecting a pressure transducer to surface-pressure taps via a Scannivalve. Pressure taps were placed in three parallel rows along the expansion for additional confirmation of two-dimensionality.

#### 4. Mean flow

The development of the mean flow in the direction of streaming for the two initial conditions (cases A and B) considered, is shown in figure 6. The streamwise distance

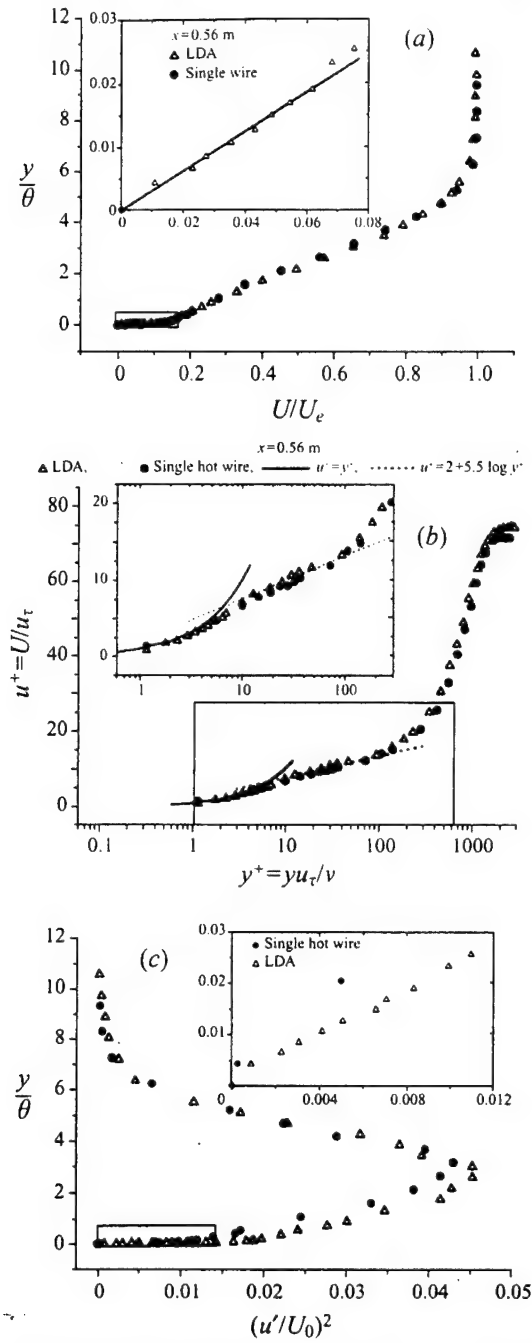


FIGURE 5. Mean and fluctuation velocities measured with the LDV and the hot wire.

is measured from a virtual origin defined by extrapolating the momentum thickness,

$$\theta = \int \frac{U}{U_e} \left(1 - \frac{U}{U_e}\right) dy,$$

to zero (where  $U_e$  is the local free-stream velocity). The reference velocity and length

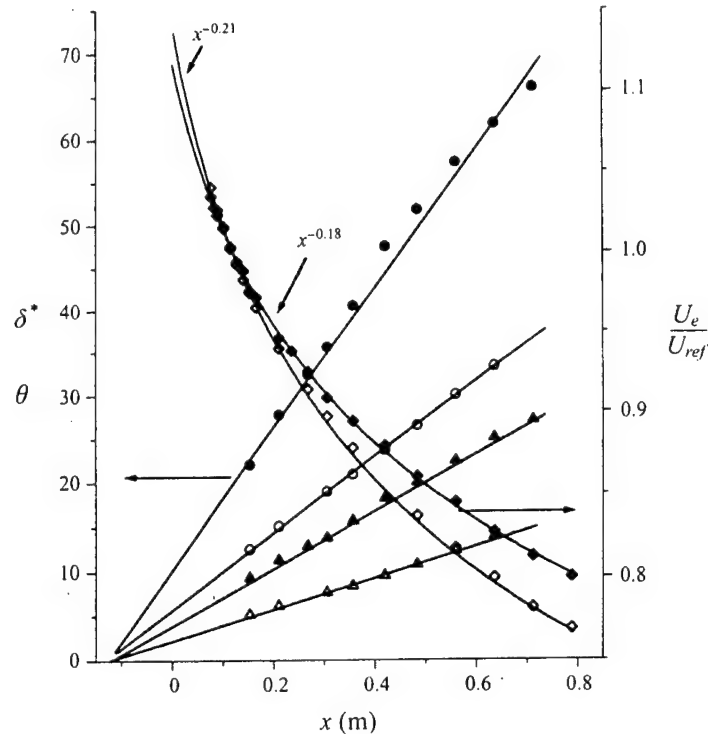


FIGURE 6. Development of the mean flow in the direction of streaming for the two initial conditions (cases A and B):  $\triangle$ ,  $\blacktriangle$ ;  $\circ$ ,  $\bullet$   $\delta^*$ ;  $\diamond$ ,  $\blacklozenge$ ,  $U_e/U_{ref}$ . Open symbols:  $\theta_0 = 2.3$  mm, solid symbols:  $\theta_0 = 4.5$  mm.

scales used throughout this article are defined as the maximum measured free-stream velocity,  $U_0$ , and the extrapolated momentum thickness,  $\theta_0$ , at the location of the free-stream velocity maximum, respectively. The flow accelerated upstream of the ramp, resulting in values of  $U_0 = 17.8 \text{ m s}^{-1}$  and  $16.7 \text{ m s}^{-1}$  with corresponding values of 2.3 mm and 4.5 mm for  $\theta_0$ , for the two cases A and B considered. This is some 15–20% higher than the  $15 \text{ m s}^{-1}$  measured by the Pitot tube that was located further upstream in the throat, suggesting that the transition from the flat surface to the ramp was perhaps too rapid when compared to an ideal airfoil design using the Stratford concept. The distance between the location at which the free-stream velocity is maximum and the virtual origin of the flow where  $\theta = 0$  (located at  $x = -0.133$  m) is denoted by  $x_0$ .

The free-stream velocity varies as  $(x - x_0)^{-0.21}$  and  $(x - x_0)^{-0.18}$  for cases A and B respectively when the streamwise distance is measured from the virtual origin (figure 6). The results presented cover a distance of approximately  $200\theta_0$ . Over that distance the free-stream velocity,  $U_e$ , was reduced by 12% from its initial reference velocity value  $U_0$ . The data presented by DF span a distance over which the free-stream velocity decelerated by 4% only. The equilibrium region in SK's experiment covered a distance of  $\Delta x/\theta_0 = 57$  corresponding to a deceleration  $\Delta U_e/U_0 = 6.7\%$ .

The flow spreads out linearly with increasing  $x$  (e.g.  $d\theta/dx = \text{constant}$ , figure 6). The initial thickness of the boundary layer has, however, an enormous effect on the flow divergence although the difference in the pressure gradient between cases A and B is small. The sensitivity of the flow to the initial boundary layer thickness can be



explained by using the momentum integral equation:

$$\frac{d\theta}{dx} + (H + 2) \frac{\theta}{U_e} \frac{dU_e}{dx} = \frac{c_f}{2}, \quad (4.1)$$

where the experimental data give:  $\theta \propto x$  and  $U_e \propto x^{-n}$  and the skin friction  $c_f \rightarrow 0$ . The group  $(H + 2)\theta/U_e dU_e/dx = \text{constant}$  also represents the rate of spread of this boundary layer. Substituting the measured values for  $H$  and  $n$ , one gets

$$(d\theta/dx)_B = 1.72(d\theta/dx)_A.$$

The experimental comparison of the growth rate of  $\theta$  between cases A and B yielded a slightly larger constant of 1.84 instead of the 1.72 anticipated. We should mention that the virtual origins for both flows were almost identical.†

The sensitivity of this boundary layer to inflow (upstream) conditions sheds some new light on previous observations and explains some of the discrepancies among them. Spangenberg *et al.* (1967) generated two very different boundary layers (the differences were most apparent in the turbulent intensities measured and in their distribution across the flow) by changing the upstream pressure gradient very slightly. DF made similar observations; since they had a fine control over their upstream pressure gradient they could change the sign of  $c_f$  by this procedure. In the region in which measurements were presented (i.e. for  $x > 1.13$  m) the pressure gradient for all three cases they considered was identical. The slight differences in the upstream pressure gradient that they introduced altered the initial thickness of the boundary layers (see figure 3 of DF) and thus changed the character and direction of the entire flow.

The assumption that the initial thickness of such a boundary layer represents the most significant parameter governing its growth enabled us to collapse the rate of spread of the dimensionless  $(\theta/\theta_0)$  of DF, SK and the present two experiments, onto a single curve (figure 7). The displacement thickness,  $\delta^* = \int (1 - U/U_e) dy$ , that also spreads out linearly in the direction of streaming, is plotted in figure 6. Its rate of spread is almost twice as large for case B than for case A, nevertheless  $(\delta^*/\theta_0)$  collapses the present experimental results onto those of DF (figure 7). The results of SK are somewhat lower because their flow was not on the verge of separation. Their shape factor,  $H = \delta^*/\theta$ , was approximately 2 while for the present data  $H$  varies slightly with distance and with the case being considered. The assumption of a constant shape factor of 2.45 and 2.55 for case A and B respectively represents most of the data. These values of the shape factor are in close agreement with the observations of Stratford (1959*b*) and have been traditionally used as a criterion for separation.

Mean velocity profiles are presented in figure 8 for cases A and B: but the symbols plotted are for case B only; the mean velocity profiles for case A are represented by the dash-dot line. The mean velocity profiles appear to be approximately self-similar when scaled by the local external velocity,  $U_e$ , and the boundary layer momentum thickness. The mean velocity gradient near the wall is small but finite and it is slightly larger for case A (see insert in figure 8) suggesting that the flow in case B is closer to separation. Spangenberg *et al.* (1967) also observed a finite velocity gradient near the surface. When the mean velocity profiles are plotted in wall variables, using

† One of the reviewers brought to our attention the similarity analysis of George & Castillo (1993) and Castillo & George (2000) who used a different similarity analysis and a different length scale. After the preparation of this paper we recast some of our data in those variables in order to provide a more meaningful discussion of those scales in the future. The results are given in the Addendum.

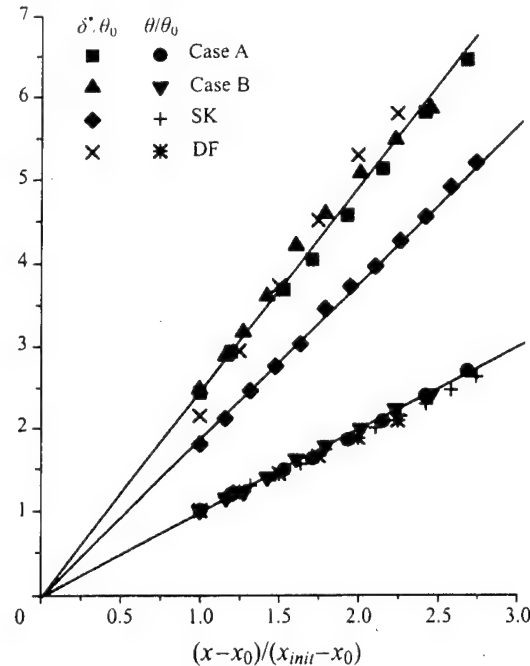


FIGURE 7. Displacement thickness and momentum thickness of the boundary layer versus downstream location for different experimental realizations.

the Clauser method to define a friction velocity  $u_\tau$  (figure 9a), a very large wake component emerges. The value of  $u_+ = U/u_\tau$ , near the edge of the boundary layer indicates the imminence of the approaching separation. While values ranging from 70 to 80 were observed in case A, they reached 95 for case B data, both numbers comfortably exceeding the values of  $u_\tau$  obtained by Spangenberg *et al.* (1967). The largest value of  $u_+$  for a zero-pressure-gradient boundary is approximately 25. These results were obtained by assuming, *a priori*, that the inner part of the velocity profiles obeyed the universal law of the wall. In that respect they differ from the velocity profile presented in figure 5(b), where  $u_\tau$  was estimated from the linear part of the law of the wall measured using a LDV.

The entire velocity profile could be adequately represented by Coles' law of the wake, i.e.

$$u_+ = 5.5 + 5.5 \log_{10} \left( \frac{yu_\tau}{\nu} \right) + \Pi \sin^2 \left( \frac{\pi y}{2\delta} \right). \quad (4.2)$$

Nishri (1996) found that  $\Pi$  is a linear function of  $(c_f)^{-1/2}$ . The results of the present experiment appear to confirm this conclusion (figure 9b). It should be noted, however, that the law of the wake did not match the experimental profile very well at the first measurement station. The variations in the shape factor and the friction coefficient with  $x$  are shown in figure 9(c). Ideally both  $H$  values should be constant when  $c_f \rightarrow 0$ ; although they are not, their variation with  $x$  is small. It is clear that a decrease in  $c_f$  is accompanied by an increase in  $H$ . There is a difference in the estimated values of  $c_f$  between case A where  $c_f = 3.4 \times 10^{-4}$  and B where  $c_f = 2.5 \times 10^{-4}$ . The very low skin friction described allows one to neglect the right-hand side of the integral momentum equation (4.1). Substitution of the experimental values for  $H$ , for  $\theta$  and for  $d\theta/dx$  into this equation with  $c_f = 0$  implies that  $U_e \propto x^{-0.22}$  for case A. This result is in

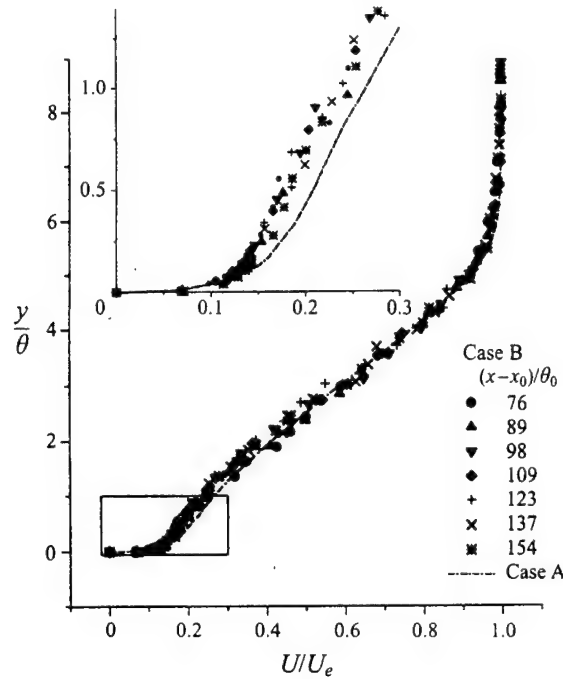


FIGURE 8. Mean velocity profiles for cases A and B.

good agreement with the experimental value, suggesting that the flow is adequately two-dimensional. Further checks on flow two-dimensionality will be described below.

### 5. Turbulence intensities and scaling

The intensities of the normal and longitudinal components of the turbulent fluctuations are plotted in figure 10(a, b) using the same length and velocity scales that were used for the mean velocity profile. In contrast to a zero-pressure-gradient boundary layer, there is very little turbulent activity close to the wall; the largest turbulence intensity occurs close to the inflection of the mean velocity profile. The field is highly anisotropic with the longitudinal component of the turbulence intensity for case A being three times greater than the transverse component. The locally normalized turbulence intensity increases with downstream distance and the location of its maximum moves further away from the surface. The Reynolds stresses behave in a similar manner although they seem to increase more moderately with  $x$  than  $\overline{u'^2}/U_e^2$  does (figure 10c). The turbulence, therefore, is not in equilibrium with the mean flow.

Since the mean velocity profile is approximately self-similar, i.e.

$$\frac{U}{U_e} = f'\left(\frac{y}{\theta}\right), \quad (5.1)$$

the scaling of the Reynolds stress and turbulent intensities should be determined by substituting (5.1) into the two-dimensional mean momentum equation

$$U \frac{\partial U}{\partial x} + V \frac{\partial U}{\partial y} + \frac{\partial}{\partial x} (\overline{u'^2} - \overline{v'^2}) + \frac{\partial}{\partial y} \overline{u'v'} - U_e \frac{dU_e}{dx} = 0. \quad (5.2)$$

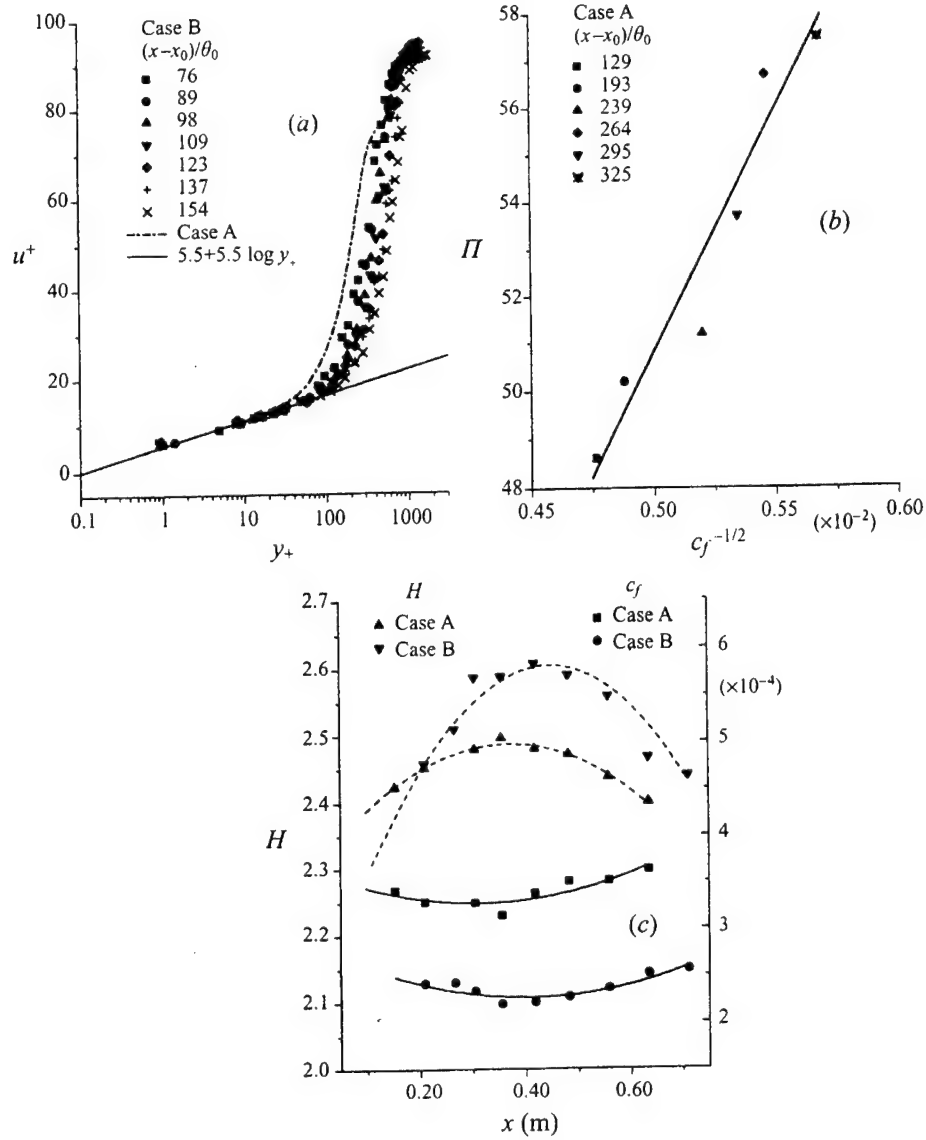


FIGURE 9. (a) Mean velocity profiles in wall variables; (b) the wake parameter,  $\Pi$ , of the wake law versus the skin friction coefficient; (c) variation of the shape factor and the friction coefficient with  $x$ .

The equation that results from this substitution is

$$U_e \frac{dU_e}{dx} (f'^2 - ff'' - 1) - \frac{U_e^2}{\theta} \frac{d\theta}{dx} ff'' + \frac{\partial}{\partial x} (\overline{u'^2} - \overline{v'^2}) + \frac{\partial}{\partial y} \overline{u'v'} = 0. \quad (5.3)$$

By assuming that the similarity scales can be expressed by power laws of  $x$ , i.e.  $U_e \propto x^{-n}$  and  $\theta \propto x^m$ , then

$$U_e \frac{dU_e}{dx} \propto \frac{U_e^2}{\theta} \propto x^{-2n-1},$$

implying that, even if similarity of the inertial terms holds true, it does not provide

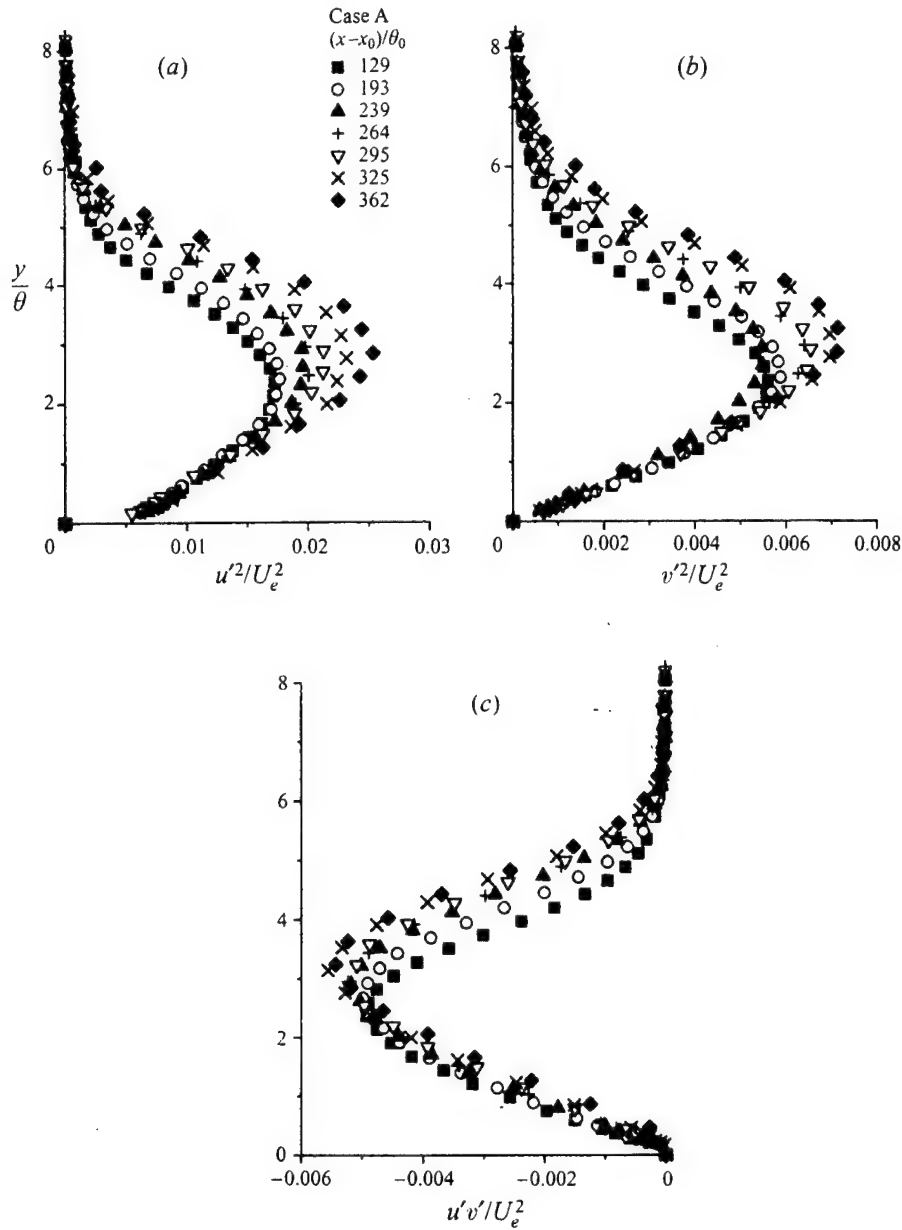


FIGURE 10. Intensities of the normal and longitudinal components of the turbulent fluctuations and the Reynolds stresses normalized with the mean velocity scales.

information about the rate of spread of the momentum thickness  $m$ . Experiments clearly indicate that  $\theta \propto x$  and therefore  $(U_e^2/\theta)d\theta/dx$  should vary as  $x^{-1.42}$  for case A and as  $x^{-1.36}$  for case B. In order to determine  $m$  an assumption must be made about the development of the Reynolds stress. The generally accepted choice is

$$\overline{u'v'} = U_e^2 g_{12}(y/\theta) \quad (5.4)$$

because in the traditional self-similar equilibrium flows all turbulent quantities scale



in the same way as the inertial terms (the analysis of Castillo & George is excepted). Examination of the data (figure 10) reveals, however, that this is not appropriate. An alternative representation,

$$\overline{u^2} = U_0^2 g_{11}(y/\theta), \quad \overline{v^2} = U_0^2 g_{22}(y/\theta), \quad \overline{u'v'} = U_0^2 g_{12}(y/\theta), \quad (5.5)$$

collapses the maxima of the normal stresses (e.g.  $(\overline{u^2}/U_0^2)_{\max}$ ) onto a single value that does not occur at a single  $(y/\theta)$  location; however, it also implies that  $m = 2n + 1$ , which contradicts the observation that  $\theta \propto x$  (i.e.  $m = 1$ ).

The approximate exponent for which the divergence of the maxima in the turbulence intensities away from the surface with increasing  $x$  stops was found to be  $\theta^{1.2}$ , provided only two significant figures were considered. This dependence on  $\theta$  may be obtained by multiplying the non-dimensional  $(y/\theta)$  location used for the mean velocity profiles by a local Reynolds number ( $Re_\theta = U_e \theta / \nu$ ), raised to the  $-0.2$  power. Figure 11 demonstrates the improvement in the non-dimensional turbulence profiles when the new length scale is combined with  $U_0$  (a constant velocity) as the velocity scale. The turbulence intensity measured for case B also scaled with the same variables; however, it was 40% higher (figure 11a). This implies that identical scaling is applicable to both cases although the proportionality constants may differ depending on the inflow conditions (i.e.  $\theta \propto x$ ;  $\theta_A = C_A x$  and  $\theta_B = C_B x$ ).

For consistency reasons one may assume that the turbulent length scale is also appropriate for scaling the mean velocity profile, i.e.

$$\frac{U}{U_e} = f' \left( \frac{y}{\theta} Re_\theta^{-0.2} \right) = f'(cyx^{-k}) \quad (5.6)$$

and substitute (5.6) into the two-dimensional mean momentum equation to give

$$U_e \frac{dU_e}{dx} (f'^2 - ff'') - 1 - C \frac{U_e^2}{\theta} \frac{d\theta}{dx} ff'' + \frac{\partial}{\partial x} (\overline{u^2} - \overline{v^2}) + \frac{\partial}{\partial y} \overline{u'v'} = 0, \quad (5.7)$$

where  $C$  is a constant depending on  $c$  and  $k$  defined in equation (5.6). This equation still scales the inertia terms in the same way as before, however,

$$U_e \frac{dU_e}{dx} \propto \frac{U_e^2}{\theta} \frac{d\theta}{dx} \propto x^{-1.4} \quad (5.8)$$

and it leads to the requirement that  $(\partial/\partial y)(\overline{u'v'}) \propto x^{-1.4}$ . The intensity scale that satisfies this requirement is the product of the reference velocity and the local external velocity,  $U_0 U_e$  (i.e.  $\overline{u'v'} = U_0 U_e g_{12}((y/\theta) Re_\theta^{-0.2})$ , see figure 11(d).

Figure 12 depicts the mean velocity profiles when scaled by the turbulent length scale  $L = \theta Re_\theta^{0.2}$ . Although the similarity of the inner region is improved, the outer part of the profile shows some deviation from similarity, particularly for case A. The data for case B are displaced and agree quite well with the proposed scaling. In this case the similarity of the outer flow is better. The deviations from self-similarity may be due to the normal stress terms, which are relatively important in the present flow. The intensity scale used for the turbulent fluctuations implies that

$$\frac{\partial}{\partial x} (\overline{u^2} - \overline{v^2}) \propto x^{-1} \phi \left( \frac{y}{\theta} Re_\theta^{-0.2} \right), \quad (5.9)$$

and it is not consistent with the development of the inertial terms and the Reynolds stress. The normal stress term (5.9) is often neglected in boundary layer flows because of the boundary layer approximation and the tendency of turbulent flow to isotropy.

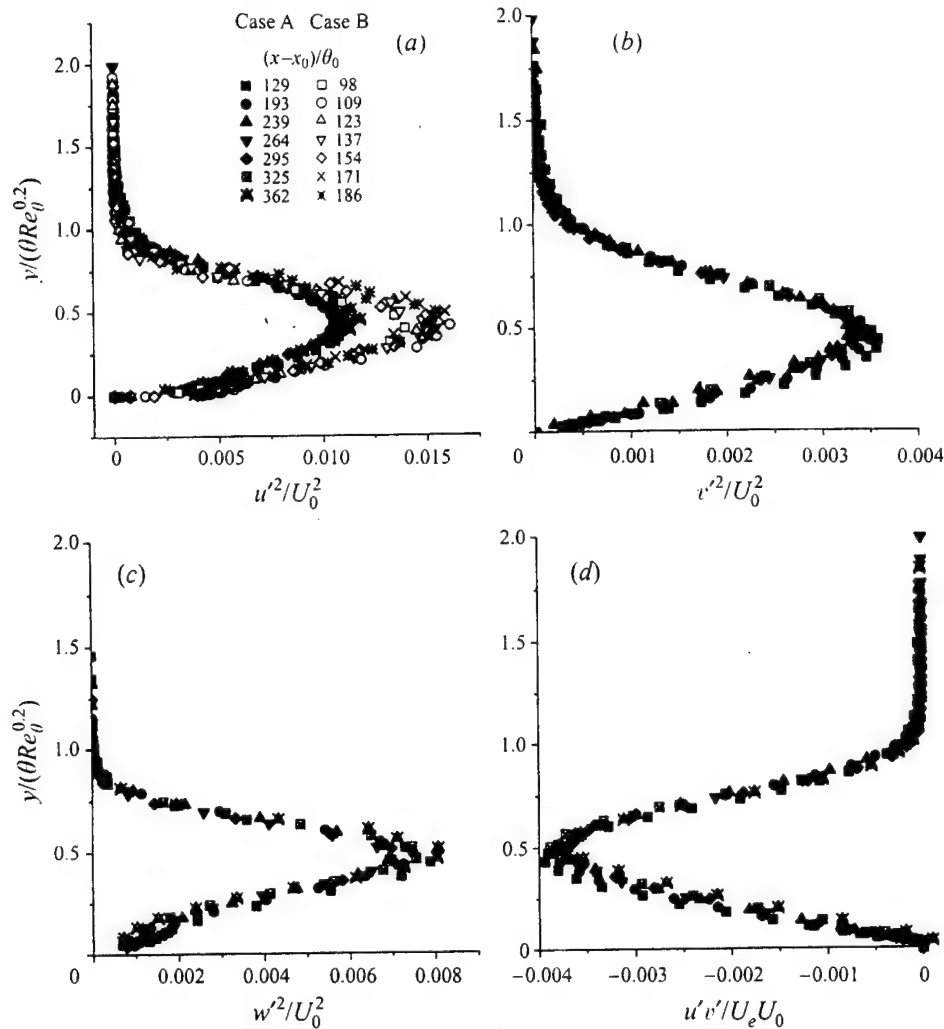


FIGURE 11. Non-dimensional turbulence profiles scaled by the new length scale,  $L = \theta Re_\theta^{0.2}$ , and a constant velocity  $U_0$ .

In this case, however, it contributes as much as 30% to the momentum budget (see figure 2).

The fact that the turbulence intensity, the Reynolds stress and the mean velocity do not share a common velocity scale indicates a lack of local equilibrium between the mean flow and the turbulent motion. Thus the flow is not self-preserving in the sense suggested by Townsend. The present scaling is consistent with the momentum equation and it may be associated with the curvature of the surface. There is also a reorganization among the energy-containing eddies because the simple Reynolds stress correlation  $\overline{u'v'}/(\sqrt{u'^2}\sqrt{v'^2})$  is neither a constant across the flow as it is in absence of pressure gradient (i.e.  $\overline{u'v'}/(\sqrt{u'^2}\sqrt{v'^2}) \approx 0.4$ ) nor does it remain constant with increasing downstream distance. This is also inconsistent with the assumptions made in simple turbulence models (Bradshaw, Ferriss & Atwell 1967) and implies that the phase relation between the  $u'$  and  $v'$  fluctuations is constantly changing in

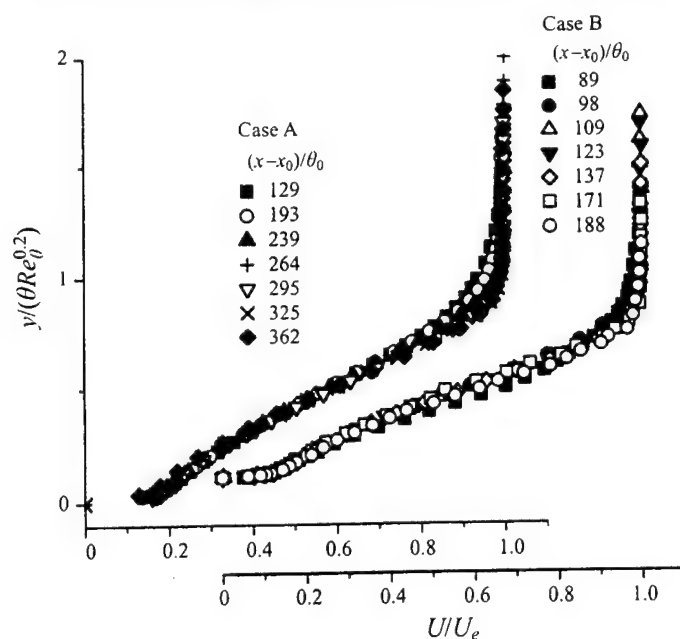


FIGURE 12. Mean velocity profiles scaled by the turbulent length scale  $L$  for the thin and the thick upstream boundary layers (cases A and B).

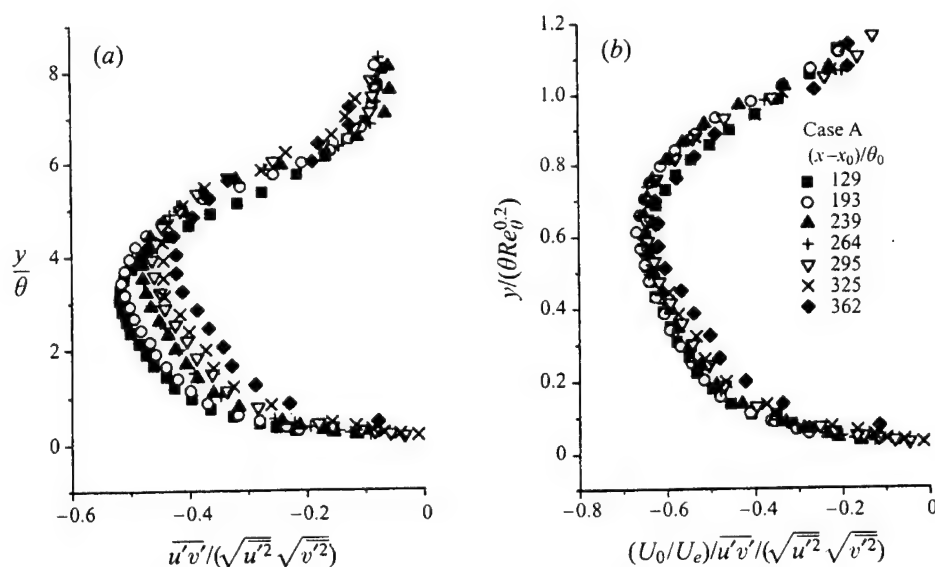


FIGURE 13. Reynolds stress correlation across the flow scaled by: (a) the local momentum thickness; (b) the turbulent length scale  $L$  and re-normalized with the factor  $U_0/U_e$ .

this flow. For this reason the quantity  $(U_0/U_e)\overline{u'v'}/(\sqrt{\overline{u'^2}}\sqrt{\overline{v'^2}})$  is plotted in figure 13. The similarity of these data is consistent with the above-mentioned scaling and it implies a preferred stretching of the larger and more energetic spanwise eddies.

The skewness factor of the velocity fluctuations is plotted in figure 14 (the subscript 1 corresponds to the streamwise velocity component; 2 corresponds to the normal

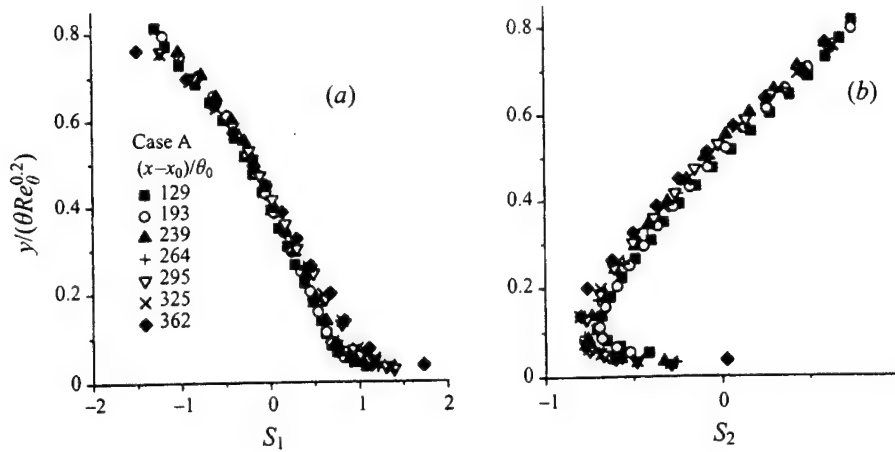


FIGURE 14. Skewness factor of the velocity fluctuations: (a) streamwise velocity component; (b) the normal component.

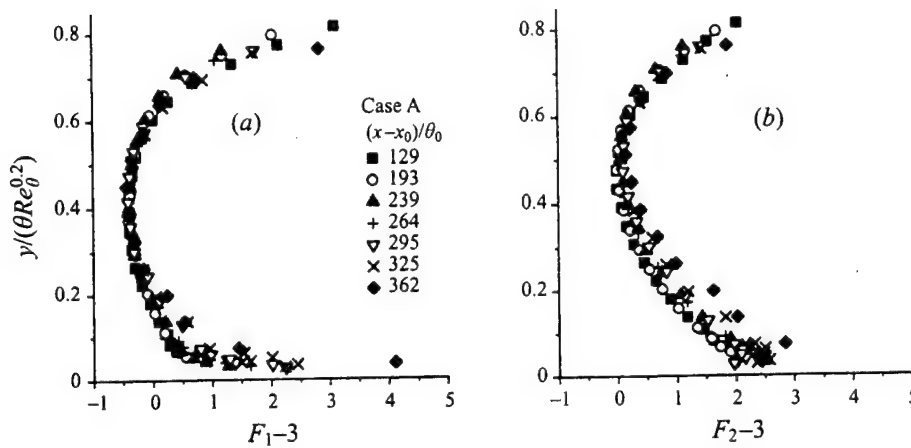


FIGURE 15. Flatness factor of the velocity fluctuations.

component). A non-zero value of this quantity indicates that the probability density function of the fluctuations is non-Gaussian. The skewness profiles exhibit good similarity when the turbulence length scale is used for their normalization; the large increase of the skewness very close to the wall may be partially due to the influence of rectification of the hot-wire sensor. The next higher statistical moment, the flatness factor, is shown as figure 15. A deviation of this value from the Gaussian value of 3 is frequently used as an indicator of intermittency or of the presence of large coherent structures. The reasonable collapse of this quantity when using the turbulence length scale supports the conclusion that the mean coordinate of the laminar-turbulent interface normalized by the local disturbance thickness increases in the streamwise direction. This, in turn, suggests that the scale of the large eddies grows more rapidly than the boundary layer thickness.

The advection speed of the turbulent eddies was measured using the time-space correlation technique at four different downstream locations and at two different normalized  $y$  coordinates (figure 16). The results show that eddies of all physical

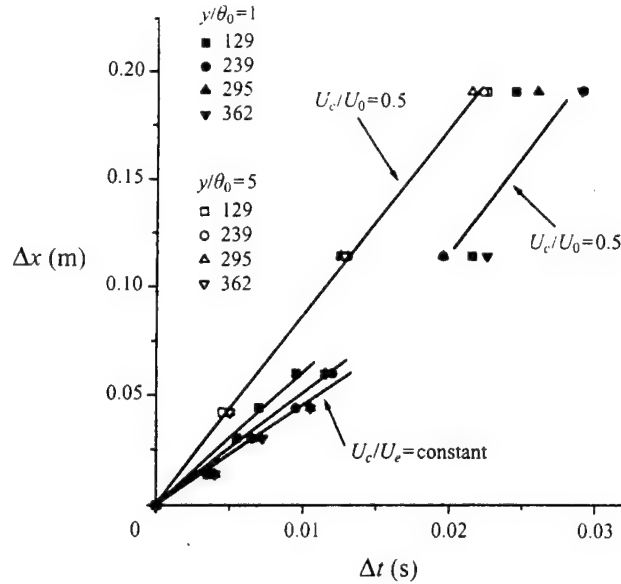


FIGURE 16. Advection speed of the turbulent eddies.

scales propagate at a constant velocity in the outer part of the boundary layer. In the inner layer, physically smaller eddies appear to be advected at a velocity proportional to the local free-stream velocity while larger eddies move at the same constant velocity observed in the outer part of the flow. This suggests that there may be two important scales in the flow; however, to distinguish between them may require instantaneous information along a plane (by using a PIV) rather than two-point information.

## 6. Turbulent kinetic energy budgets

The energy budgets of the present flow were found to differ radically from what is seen in a zero-pressure-gradient boundary layer, where the turbulence energy is concentrated close to its source of production, the intense shear near the wall. For the present flow the role of the wall appears to be greatly reduced.

The conventional turbulent kinetic energy equation expressed in indicial notation is

$$U_j \frac{\partial}{\partial x_j} \left( \frac{1}{2} \overline{u_i u_i} \right) = - \frac{\partial}{\partial x_j} \left( \overline{u_j p} + \frac{1}{2} \overline{u_i u_i u_j} - \frac{2}{Re} \overline{u_i S_{ij}} \right) - \overline{u_i u_j S_{ij}} - \frac{2}{Re} \overline{S_{ij} S_{ij}}, \quad (6.1)$$

$$\text{where } u_i \equiv U_i + u'_i, \quad s_{ij} \equiv \frac{1}{2} \left( \frac{\partial u_i}{\partial x_j} + \frac{\partial u_j}{\partial x_i} \right), \quad S_{ij} \equiv \frac{1}{2} \left( \frac{\partial U_i}{\partial x_j} + \frac{\partial U_j}{\partial x_i} \right).$$

The term on the left-hand side is the rate of transport of turbulent kinetic energy by the mean motion. The first term on the right represents the transport of turbulent energy by pressure fluctuations, velocity fluctuations, and viscous stresses respectively. The viscous term is negligible compared to the remaining terms and was not included in the energy balance. The pressure transport term is not directly measurable; it is obtained from knowledge of the remaining terms. The second term on the right represents the production of turbulence by the interaction of velocity fluctuations and



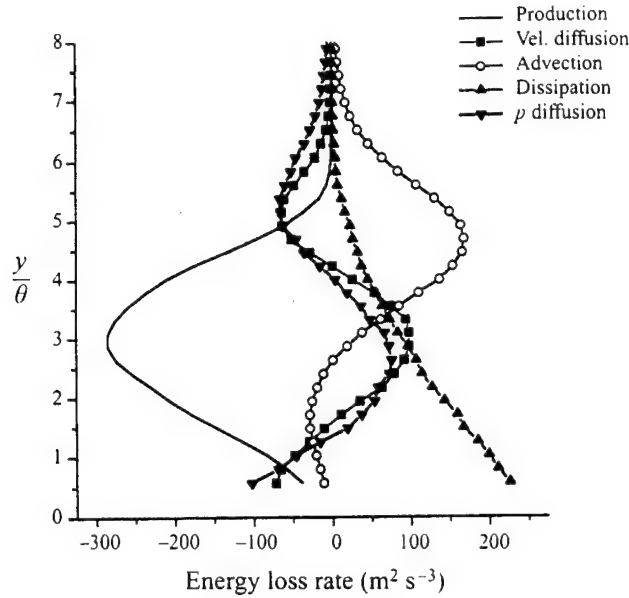


FIGURE 17. Turbulent kinetic energy balance for location  $(x - x_0)/\theta_0 = 295$  (case A).

mean strain. The final term on the right-hand side is the dissipation of turbulent energy into thermal energy through the action of viscosity. Several different approximations are used when measuring these terms.

The second term on the right-hand side of equation (6.1) is simplified for a two-dimensional mean flow to

$$\text{Production} = (u'^2 - v'^2) \frac{\partial U}{\partial x} + \overline{u'v'} \frac{\partial U}{\partial x}, \quad (6.2)$$

and is dominated by the term involving the Reynolds stress. Production is plotted along with the other terms of equation (6.1) in figure 17 for  $(x - x_0)/\theta_0 = 295$ . The production of turbulence energy has a strong maximum around  $y/\theta = 3$  where both the mean gradient and the velocity correlation  $\overline{u'v'}$  have their respective maxima. This is also the location of the inflection in the mean velocity profile as well as the maxima of  $u'$  and  $v'$ . The correspondence of the inflection point and the production maximum indicates that the flow is dominated by a single inflectional instability, confirming the results of stability theory that show that the peak of the amplitudes of the harmonic oscillations occurs at the same  $y$ -location. The hot-wire anemometer is well suited to the exploration of this important region. Because of small uncertainty in the data taken at  $y/\theta < 0.25$  (see figure 5) this region was excluded from the energy budget.

The estimation of dissipation requires the use of an approximation because the energy-dissipating eddies are too small to be properly resolved by conventional x-wire probes. Since the turbulence intensity is large, Heskestad's (1965) modification of Taylor's hypothesis was used to obtain the spatial derivative from the measured temporal derivative. This modification replaces the local mean with the instantaneous velocity, i.e.

$$\frac{\partial u_i}{\partial t} = -u \frac{\partial u'_i}{\partial x_j} \quad (6.3)$$

rather than

$$\frac{\partial u_i}{\partial t} = -U \frac{\partial u'_i}{\partial x_j} \quad (6.4)$$

Heskestad's approximation is considered to be more accurate when large velocity fluctuations are present. The energy-dissipating motions were considered to be isotropic, which allows the turbulent strain rate tensor to be replaced by

$$\text{Dissipation} = 15 \left( \overline{\frac{\partial u_1}{\partial x}} \right)^2 \quad (6.5)$$

The dissipation increases monotonically toward the wall, suggesting that a careful exploration of this region is needed in order to understand this process next to the surface. Dissipation seems to be entirely divorced from production and in this respect it resembles the dissipation term in a wake, where the wake centreline corresponds to the surface in the present flow.

For a two-dimensional boundary layer, the convection term becomes

$$\text{Convection} = \frac{1}{2} U \frac{\partial \overline{q'^2}}{\partial x} + \frac{1}{2} V \frac{\partial \overline{q'^2}}{\partial y} \quad \text{where} \quad \overline{q'^2} = \overline{u'_i u'_i} \quad (6.6)$$

Although the turbulence intensity plotted in non-dimensional coordinates does not vary with downstream distance, the rapid growth of the boundary layer results in a large spatial gradient of  $q'^2$ ; the first term in equation (6.6) therefore dominates the advection. The peak of advection occurs at about  $y/\theta = 4.5$ , a relatively small distance inside the boundary layer. In this respect the convection term again resembles the wake rather than the equilibrium boundary layer (see Townsend 1976, pp. 206–207, 293). However, advection is considerably weaker in the inner part of the layer; this contrasts dramatically with the wake, where advection is very strong near the centreline. The advection term is relatively important for the present flow because turbulence produced near the inflection is convected outwards, where dissipation is inadequate to destroy it. This is in contrast to the zero-pressure-gradient case where approximate equilibrium exists between dissipation and production; at present production near the surface is the only term that is dominated by the  $x$ -derivative because  $\partial u/\partial y$  vanishes. The strong advection may be associated with a more rapid increase in the turbulent length scale relative to the mean length scale.

The diffusion of energy by velocity fluctuations in a two-dimensional boundary layer is given by

$$\text{Diffusion} = \frac{1}{2} \left( \frac{\partial}{\partial y} \overline{v' q'^2} + \frac{\partial}{\partial x} \overline{u' q'^2} \right), \quad (6.7)$$

$$q'^2 = u'^2 + v'^2 + w'^2.$$

The second term is usually negligible in boundary layer type flows; this proved to be the case here. Of the six terms in equation (6.7) four were measured. Previous experiments showed  $\overline{w'^2}$  to be approximately twice  $\overline{v'^2}$  so  $\overline{v' w'^2}$  was taken to be equal to  $2\overline{v'^3}$  and  $\overline{u' w'^2}$  was taken to be the same as  $2\overline{u' v'^2}$ . The velocity fluctuations are seen to transport turbulent energy away from its peak (located at about  $y/\theta = 3$ ) toward the surface and toward the edge of the boundary layer. The pressure term is obtained by subtracting the remaining terms on the right-hand side of equation (6.1) from those on the left-hand side. Pressure transport has the same sign and approximately the same magnitude as the velocity transport term in the outer part of the layer. This again is analogous to the wake (see, for example, Hinze 1959), although the

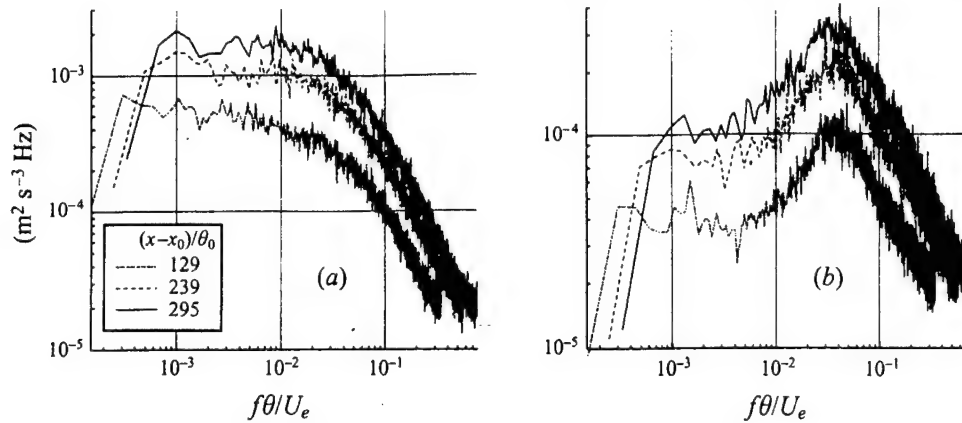


FIGURE 18. Power spectra of the velocity fluctuations at  $y/\theta = 5$  for three downstream locations and for: (a)  $u'$  and (b)  $v'$  velocity components.

pressure transport term has a greater significance in this flow, particularly as the wall is approached.

In order to identify and determine the scaling parameters of the large coherent structures in the flow, power spectra of the velocity fluctuations were measured (figure 18). In order to reduce the variance of the spectral estimate, the time series of approximately three minutes of length, were divided into 64 equal segments. The power spectrum was then computed for each segment, and the segments were averaged. Only those time records obtained in the outer part of the boundary layer show highly distinctive peaks, and then only for the normal component of the fluctuations,  $v'$ . The Strouhal number of this peak, being approximately 0.04, closely matches the Strouhal number observed in the mixing layer. This supports the view that the outer part of the present flow resembles a mixing layer that in the mean is in contact with the surface. Furthermore, since the shear layer is dominated by a single, inflectional instability we expect the same to hold true for the present flow. No peak is apparent in the  $u'$ -spectrum at any depth of the boundary layer. The spectra exhibit good overall similarity in terms of the predominant frequencies; the general increase in power with downstream distance shown is a result of the broadening of the non-dimensional fluctuation profiles.

## 7. The effects of periodic excitation

### 7.1. The thin forced boundary layer (case A)

The influence of harmonic excitation on the mean flow for case A is shown in figure 19. The increase in streamwise velocities close to the wall suggests that momentum is transferred from the outside toward the inner region. The shape of the velocity profiles becomes fuller when compared with the unforced case, implying that the flow is no longer on the verge of separation. Although the strongest effect of forcing is observed near the surface, the thickness of the boundary layer was also reduced (figure 20). A comparison between the different frequencies of excitation reveals that the mean flow was most receptive to a forcing at 63 Hz, which corresponds to a dimensionless frequency that is based on inflow conditions of  $f\theta_0/U_0 = 0.008$ . However, the average local dimensionless frequency in the region of interest (i.e. for  $150 < (x - x_0)/\theta_0 < 350$ ) corresponding to the 63 Hz excitation is five times larger

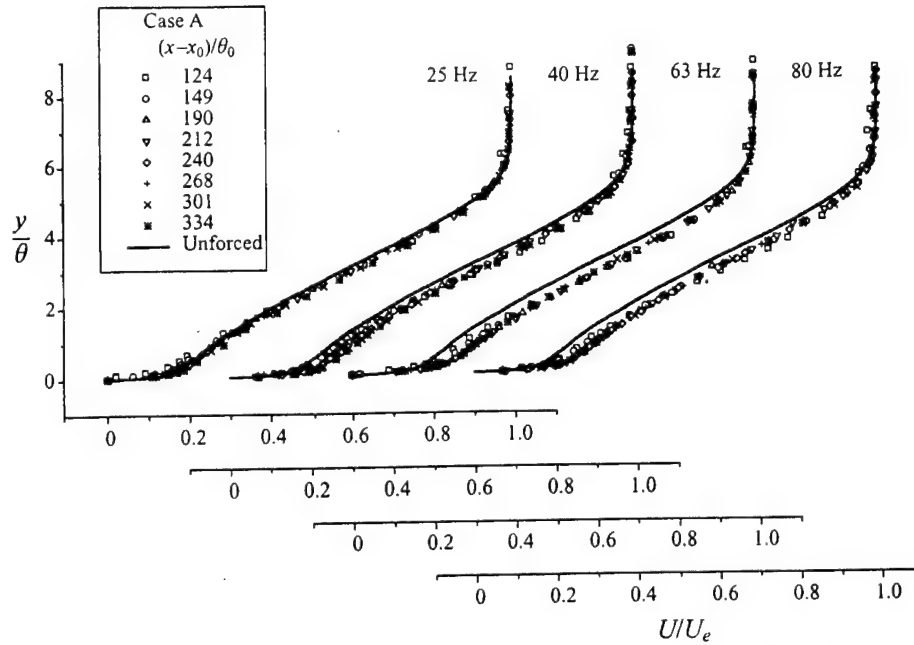


FIGURE 19. The effect of various frequencies of excitation on the mean flow distortion.

(i.e.  $f\theta/U_e = 0.04$ ). For the case of the classical mixing layer between two parallel streams in the absence of pressure gradient this frequency would correspond to the harmonic plane disturbance that had undergone the highest possible amplification by the flow. As can be judged from figure 20, the momentum thickness is not affected by the addition of excitation. This is due to the fact that the most significant change in the mean velocity occurred close to the wall (i.e. in a region in which the velocity is low) and thus the value of the integrand  $(U/U_e(1 - U/U_e))$  is insensitive to these changes. On the other hand, the periodic addition of momentum causes a decrease in displacement thickness that is also maximum at  $f\theta_0/U_0 = 0.008$  and amounts to 16% of the local  $\delta^*$ . Thus the boundary layer becomes thinner, and the velocity profile slightly fuller, when high-momentum fluid coming from the outer region is mixed with the fluid in the inner region. The impact of the harmonic excitation on the turbulent intensities may be seen in figure 21. The maximum level of the turbulence intensity was reduced as a result of the excitation at all the forcing frequencies considered; however, the reduction is also highest for the 63 Hz ( $f\theta_0/U_0 = 0.008$ ) excitation. A slightly higher level of fluctuations can be observed close to the wall; however, the accuracy of these hot-wire data is questionable due to possible rectification of the hot-wire response during flow reversals. The observed increase in  $u'$  may in fact serve as an indication that the overall duration of the reverse flow periods has diminished due to the excitation because degree of rectification was possibly reduced.

The mean velocity distribution scaled by the friction velocity  $u_\tau$  with respect to the wall variable  $y_+ = yU_\tau/\nu$  is presented in figure 22 for two streamwise locations. It is evident that higher-frequency excitation reduced the maximum value of  $(u_+)_{\max} = U_e/u_\tau$  from its initial value of 80 to approximately 65. The linear region of this semi-logarithmic plot was also used to estimate the friction velocity and to calculate the friction coefficient  $c_f = 2(u_\tau/U_e)^2$  as well. The impact of harmonic excitation on skin friction is summarized in figure 23(a). The lowest excitation frequency had

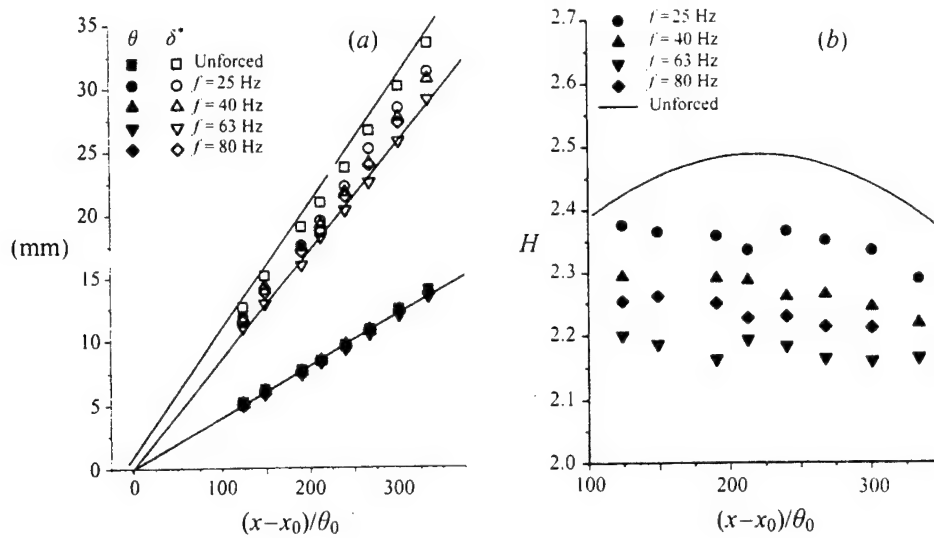


FIGURE 20. The effect of excitation on the integral parameters of the flow.

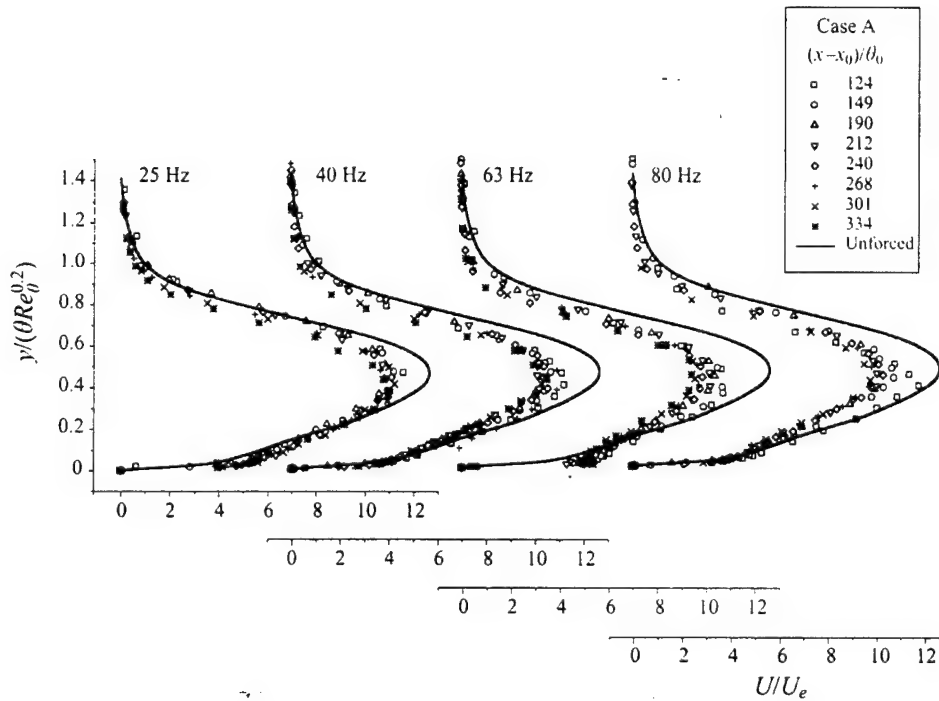


FIGURE 21. The effect of excitation on the turbulence level in the flow.

no effect on  $c_f$  for all the  $x$  values considered; however, when the frequency was increased to 40 Hz,  $c_f$  increased almost monotonically with increasing distance. At the excitation frequency of 63 Hz  $c_f$  was essentially constant throughout and was approximately 60% higher than for the unexcited flow. This increase is a direct result of the momentum transferred to the mean flow near the surface by the large eddies.

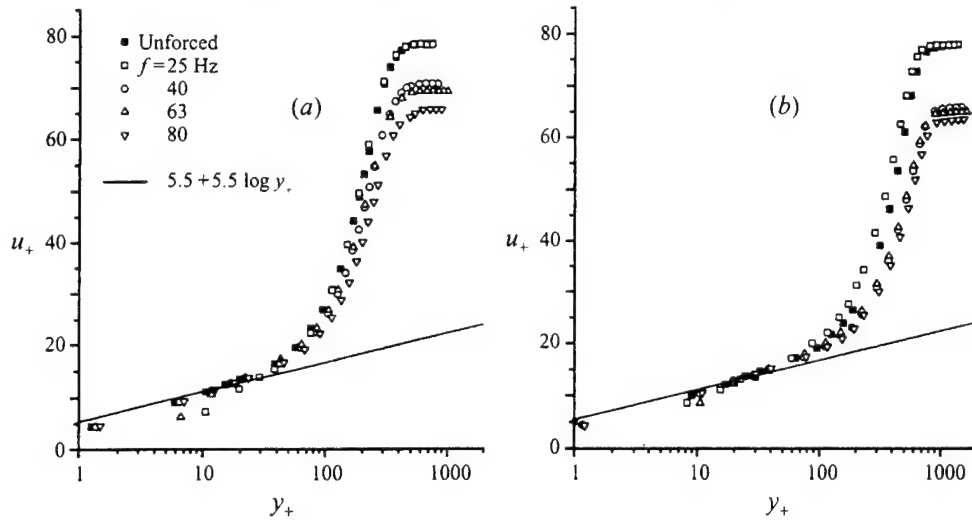


FIGURE 22. The effect of excitation on the wake component in the velocity profile.  
(a)  $(x - x_0)/\theta_0 = 124$ , (b)  $(x - x_0)/\theta_0 = 301$ .

The average skin friction over the measured interval is plotted in figure 23(b) together with the shape factor,  $H$ . The latter also decreased due to the excitation.

In order to determine growth and decay of the perturbations introduced the coherent energy was calculated according to

$$\left. \begin{aligned} \text{total coherent energy} & \quad \int_0^\infty \langle u' \rangle^2(x, y) dy / \int_0^\infty \langle u' \rangle_f^2(x_0, y) dy, \\ \text{contribution of fundamental} & \quad \int_0^\infty \langle u' \rangle_f^2(x, y) dy / \int_0^\infty \langle u' \rangle_f^2(x_0, y) dy, \\ \text{contribution of 1st harmonic} & \quad \int_0^\infty \langle u' \rangle_{2f}^2(x, y) dy / \int_0^\infty \langle u' \rangle_f^2(x_0, y) dy. \end{aligned} \right\} \quad (7.1)$$

The results are plotted in figure 24. Surprisingly, the modes that have undergone the highest amplification, like the 25 Hz mode (figure 24b), had no significant effect on the mean flow. Decaying modes (like the 63 Hz excitation) on the other hand distorted the mean velocity profile and removed the flow from the brink of separation. It seems that the first harmonic of the forcing frequency (figure 24c) plays an important role in distorting the mean flow.

### 7.2. The thick forced boundary layer (case B)

In the second test the upstream boundary layer was artificially thickened to  $\theta_0 = 4.5$  mm, through the addition of roughness. The flow was now forced at two different frequencies and two forcing levels. In order to retain dimensionless frequencies  $F = f\theta/U_e$  comparable with the former case, the forcing frequencies had to be lowered since the average local momentum thickness was effectively doubled (see figure 6) while the velocity of the free stream remained unaltered. The data presented contain two excitation frequencies: 25 and 40 Hz. The actual forcing level had to be increased as a consequence of the normalization defined in equation (2.1). The results presented correspond to  $c_\mu = 0.06\%$  and to  $c_\mu = 0.11\%$ . The excitation accelerated the flow near the slot, particularly for the higher forcing level. It also generated strong harmonic

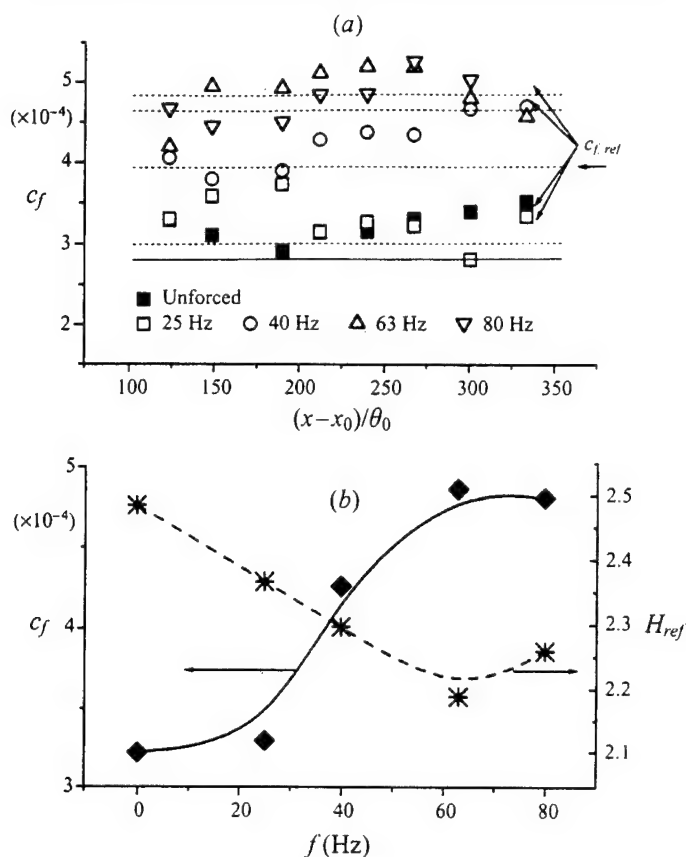


FIGURE 23. The effect of excitation on the skin friction and on  $H$ .  
The range of integration in (b) is:  $(x_2 - x_1)/\theta_0 = 210$ .

frequencies at the beginning of the ramp. For the higher  $c_{\mu}$ , the first harmonic frequency is even more energetic than the fundamental.

The influence of the harmonic excitation on the shape of the mean velocity profile may be seen in figure 25. The results are similar to the thin,  $\theta_0 = 2.3$  mm, inflow conditions. The value of the excited reduced frequencies  $f\theta_0/U_0 > 0.008$  distorted the mean velocity near the surface by increasing its value. Now, however, the entire velocity profile appears to be fuller when compared to the results of figure 19. While the increase in the initial, dimensionless forcing frequency from 0.007 to 0.011 does not alter the ensuing mean velocity profile, the forcing level does. A higher forcing level (filled symbols) results in a fuller shape of the mean velocity profile. Both forcing levels remove the flow from the brink of separation.

Figure 26 summarizes the impact of the excitation on the integral length scales of the flow. In contrast to the thin boundary layer experiment, the rate of spread of the momentum thickness,  $\theta$ , was now decreased slightly by the periodic excitation. This is particularly obvious at larger values of  $x$ . The displacement thickness  $\delta^*$  is affected more by the increase in amplitude than by the change in the frequency, for the two frequencies considered. At the lower amplitude the reduction in  $(d\delta^*/dx)$  was 12% relative to its unforced value while for the higher amplitudes this reduction reached 20% of its unforced value. As a consequence the shape factor,  $H$  (figure 26c), was

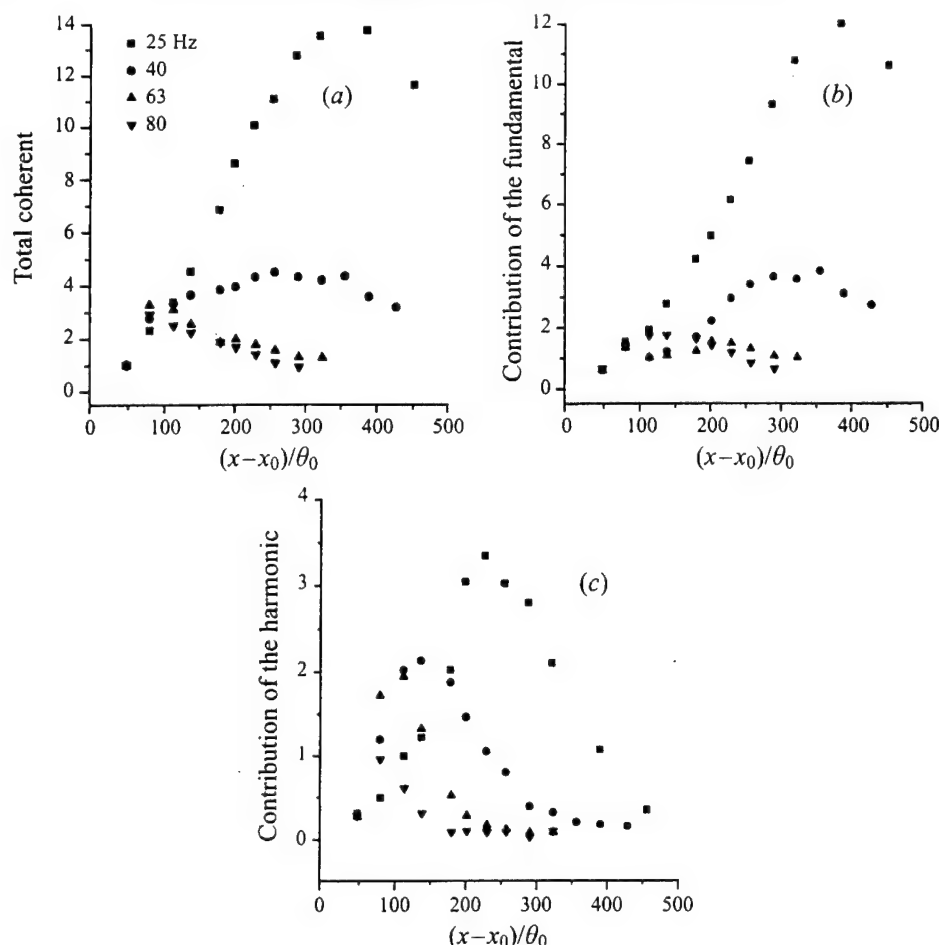


FIGURE 24. The amplification and decay of the imposed perturbations.

reduced from its initial value of 2.5 to 2.35 or 2.1 depending on the amplitude of the excitation. The value of  $H$ , however, increases with increasing  $x$  while the concomitant value of the friction coefficient (figure 26*b*) decreases with distance. This suggests that the flow will eventually approach the brink of separation (at large values of  $x$ ) in spite of the level of the plane harmonic excitation that was applied. One may speculate that the effect of decaying perturbations on the mean flow will eventually decrease at larger distances.

The distributions of turbulent fluctuations for the two forcing frequencies and two forcing levels are plotted in figure 27. Plane harmonic perturbations again reduced the level of the turbulent fluctuations and the reduction increased with increasing the input level. If turbulent intensity is a measure of the approaching separation then the reduction of this intensity signifies stabilization of the flow. One may also note that the scaling proposed in § 5 also applies to externally excited flows.

The local amplitudes of the forced perturbations and their harmonics, the amplification factors and the mean velocity field (both with and without the imposed excitation) could provide one with sufficient data to predict the effects of excitation on this flow. It is clear that the mean velocity profile that possesses an inflection



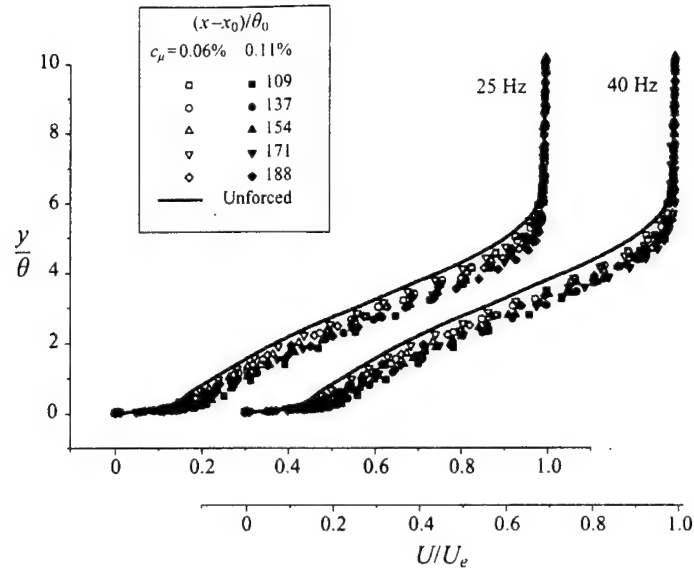


FIGURE 25. The distortion of the mean velocity profiles by periodic excitation of case B.

point is very unstable in the inviscid sense and contributes to the amplification of the imposed perturbations. A classical stability model can thus be used, provided the divergence of the flow is accounted for in the same way as for the mixing layer (e.g. Gaster, Kit & Wygnanski 1985). One may also account for the distortion of the mean flow by considering the leading nonlinear interactions. This was not attempted in the work presented here.

### 8. Further comparison with previous investigations

Finding a suitable basis for comparison with the results obtained by previous experimenters proved difficult. In the case of Stratford (1959*b*), the region most comparable with the present results (the region of constant shape factor) was specifically noted as being possibly contaminated by secondary flows. It is clear that the developmental history of the two flows is very different. For the experiment reported here the boundary-layer momentum thickness grows by a factor of 6 between the initiation of the adverse pressure gradient and the first experimental profile; in Stratford's case the corresponding ratio is about 2.5. Stratford's initial boundary layer profiles are far from being under conditions of imminent separation, for example the reported shape factor does not exceed 2.0 until the free-stream velocity ratio has fallen to 83% of its initial value. This velocity ratio represents a very substantial pressure rise.

SK claim to have produced an equilibrium boundary layer close to separation; however, their measured shape factor  $H$  is 2. In addition, the range of flow development for which they report equilibrium conditions is very short. Over this range the momentum thickness increased by only 42%, whereas for the present flow the ratio of the momentum thickness between the final and the initial stations is 2.52 for case A and exceeds 3 for case B. For an increase in  $\theta$  that is comparable to SK's even the present measurements would tend to suggest the existence of equilibrium conditions, since only the first two profiles would have been included in the analysis. Closer

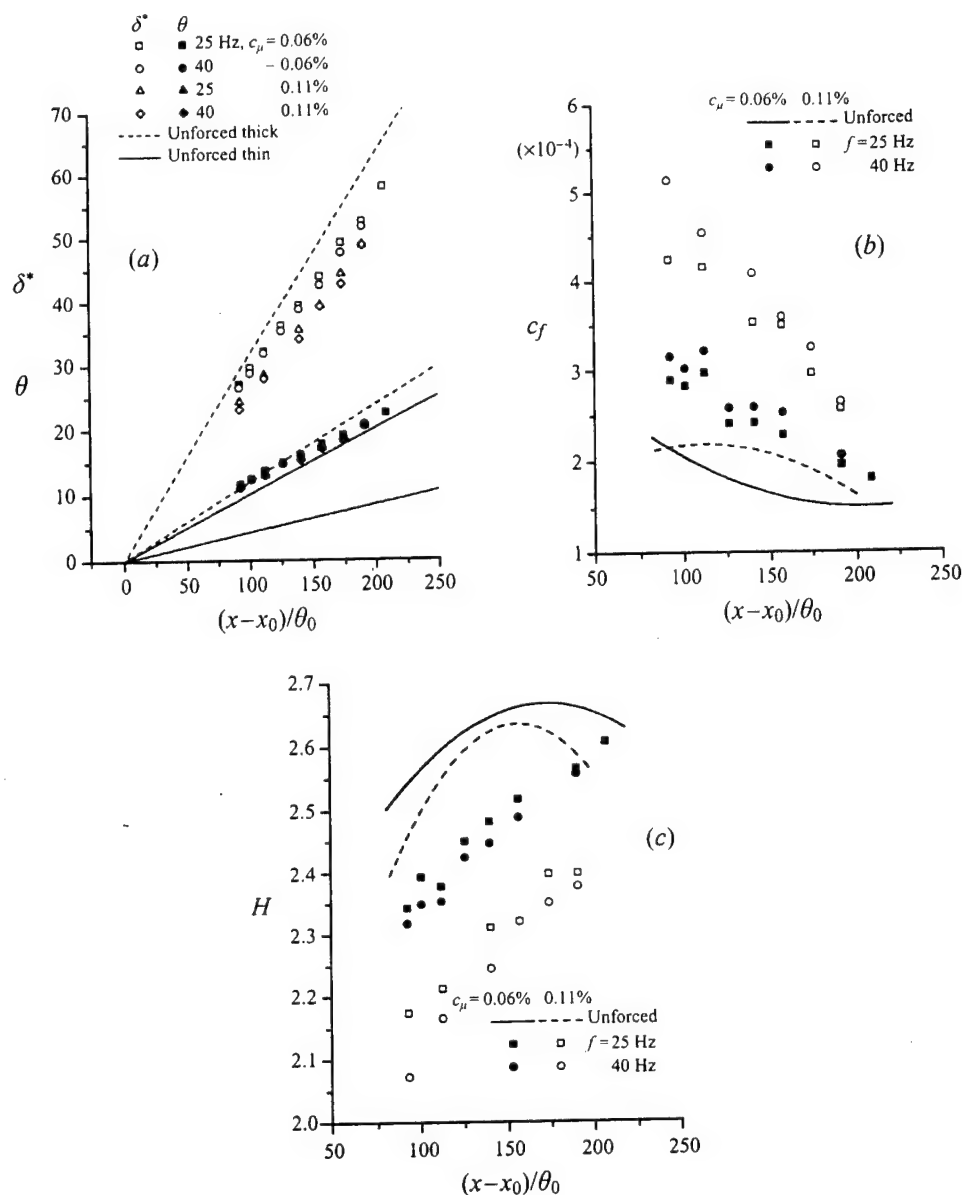


FIGURE 26. The effects of excitation on the integral parameters in case B.

observations of SK's results reveal substantial streamwise development, similar in magnitude to the changes observed over a comparable distance for the present flow.

The experiment most similar to the present investigation, in both instrumentation and procedure, is that of Spangenberg *et al.* (1967). The experimental facility was similar to the one used here but the measurements were done on a flat surface rather than on a curved wall. Provided the comparison is restricted to the region where  $(d\theta/dx)$  is constant, some results are in reasonable agreement. The exponent they used for the free-stream velocity is, however, much larger ( $-0.34$ ). The shape factors in this region are comparable ( $\approx 2.5$ ) but their maximum value of  $u_+$  was somewhat

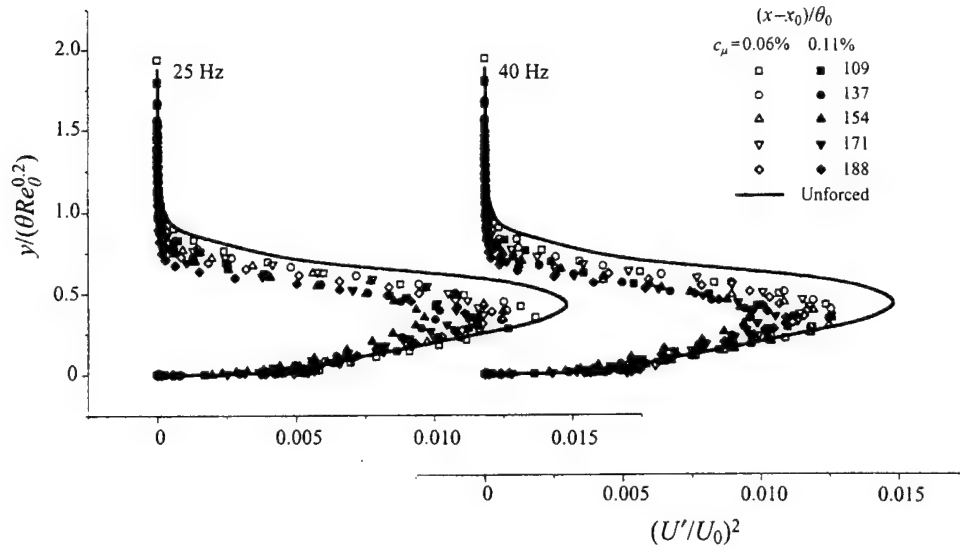


FIGURE 27. The effect of excitation on the turbulence level in case B flow.

	$\frac{u'}{U_0}$	$\frac{v'}{U_0}$
Spangenberg <i>et al.</i>	$\approx 0.08$	$\approx 0.055$
Present data	$\approx 0.10$	$\approx 0.058$

TABLE 1. Comparison of maxima in  $u'$  and  $v'$ .

lower and it never exceeded 60. The turbulent intensities show the same overall behaviour. In non-dimensional coordinates (in terms of momentum thickness) the location of the maximum intensity moves away from the surface as the flow moves downstream, while the magnitude of the peaks remain approximately constant. The magnitude of the maxima in  $u'$  and  $v'$  are in reasonable agreement with the present data, as shown in table 1. Significantly perhaps, the Reynolds stress correlation shows the same basic trend as was seen in the present experiment, tending to decrease with downstream distance.

## 9. Summary and conclusions

Measurements in a boundary layer that was maintained on the verge of separation were made in order to establish its overall statistical behaviour. This boundary layer is extremely sensitive to the upstream flow conditions and its rate of spread is proportional to its initial thickness  $\theta_0$ . The shape factor of the resulting layer was approximately 2.5, comparable with earlier attempts to produce this kind of flow. Although the flow was driven as close to separation as practicable, the region of zero wall stress predicted by Stratford (1959a) was not observed. This is because the smallest increase in the adverse pressure gradient may cause a sudden, total detachment of the flow.

The mean velocity and the turbulence intensity were found to have different

similarity scales, indicative of a lack of equilibrium. Nevertheless the proposed scaling (that is most probably not unique – see George & Castillo 1993; Castillo & George 2000) collapsed the turbulence intensities and the Reynolds stress fairly well and is consistent with the momentum equation. Spectral measurements suggested that the bulk of the flow field was affected by a single, inflectional instability mode. The presence of the solid surface had no influence on the production of turbulence and the convection velocity of the larger eddies. The loss of mean kinetic energy to turbulence production is large in this flow and it may detract from the efficiency of Stratford's concept. Most of the dissipation, however, occurs below the inflection point and attains its maximum close to the surface. The smaller eddies close to the wall are also slower than the larger ones at the edge of the boundary layer and their advection velocity seems to scale with the local free stream. External two-dimensional excitation generated eddies that can be described by an instability of the mean motion (Tumin, Likhachev & Wygnanski 1998). However, only the decaying, smaller eddies increase the skin friction by distorting the mean velocity profile near the surface. This nonlinear process needs to be investigated in the future as it may shed light on the dissipation as well. Finally, the lack of equilibrium might be attributed to surface curvature, which generates streamwise vortices due to centrifugal instability of the mean motion. Such instability is not present when one investigates a flow on the opposing, flat surface. Two-dimensional excitation may, interact and detract from the coherence of the streamwise vortices. This phenomenon is currently under investigation experimentally (P. Nishri & R. Neuendorf, private communication).

This research was supported by the Office of Naval Research, Grant # N00014-94-1, monitored by Dr Patrick Purtell. Thanks are also due to Dr O. Likhachev for his contribution to a better understanding of this experiment.

### Addendum

The present experimental results were reprocessed in a manner suggested by George & Castillo (1993), Castillo & George (2000, hereafter referred to as CG) who developed a similarity analysis for turbulent boundary layers in the presence of pressure gradient. The major conclusions are listed below:

#### A.1. The pressure gradient parameter $A$

The similarity of the mean velocity profiles is good in spite of the choice of the boundary layer thickness,  $\delta$ , to normalize the distance measured from the wall (figure 28a). The local Reynolds numbers  $Re^* = \delta u^*/\nu$  for case A vary from 450 to 750 and for case B from 700 to 1100.  $U_{so}(x)$  in CG's notation is  $U_e$ .

The pressure gradient similarity parameter,  $A$ , may be determined from the slope of either  $\delta$ ,  $\delta^*$ , or  $\theta$  when plotted against  $U_e$  (figure 28b). For case A, the average value of  $A$  is 0.204; however,  $A = 0.170$  for case B. Coupling CG's definition of  $A$  with the momentum integral equation,

$$A = \frac{\delta}{(d\delta/dx)} \frac{1}{U_e} \frac{dU_e}{dx},$$

$$\frac{d\theta}{dx} + (H + 2) \frac{\theta}{U_e} \frac{dU_e}{dx} = 0.$$

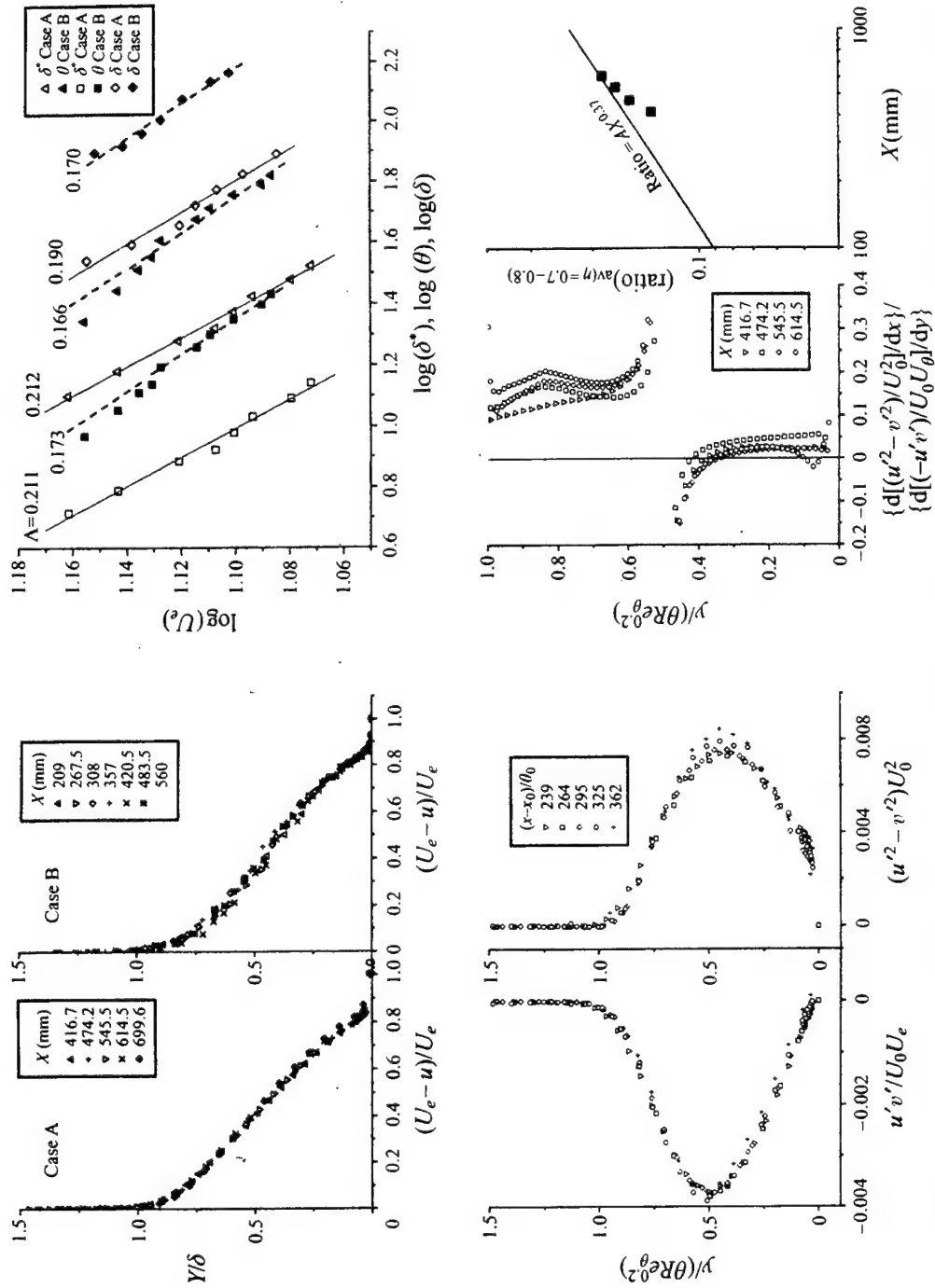


FIGURE 28. The similarity analysis: (a) mean velocity profiles, (b) pressure gradient similarity parameter, (c) Reynolds stress distribution; (d) the importance of normal stress.

Assuming  $\theta = C_1 X$ ,  $\delta = C_2 X$ , the following expression for  $A$  is derived:

$$A = \frac{1}{H + 2}.$$

For case A where  $H = 2.5$ , this results in  $A = 0.22$ . This is close to the value found using CG's procedure (figure 28*b*). The agreement with case B is less good; perhaps the rate of spread is not perfectly linear or  $C_f$  cannot be assumed to vanish.

### A.2. The significance of the normal stresses

The following discussion is limited to case A only. The normal stress (figures 10 and 11) scale differently from the shear stress (figure 13) and therefore no similarity can be obtained by normalizing these quantities by a single length scale  $\delta$ . These quantities are replotted in figure 28(*c*) in order to assess the possible significance of the normal stress to the momentum balance. The data collapses by using  $(\theta Re_\theta^{0.2})$  as a length scale and two different velocity scales,  $U_0 U_e$  for shear stress and  $U_0^2$  for the difference  $(u'^2 - v'^2)$ .

In order to differentiate the data (to assess the contribution of each term to the momentum budget), the distribution was first smoothed by fitting a Gaussian to the shear stress and a polynomial to the normal stress. The corresponding terms in the momentum equation were calculated and then their ratio was established. The distribution of the ratio between normal stress term and the shear stress term is shown in figure 28(*d*) where a small region near the wall was excluded. Nevertheless the ratio tends to infinity at the inflection point of the mean velocity profile, but otherwise it is approximately constant. It is obvious that the normal stress plays an important role in the outer region (above the inflection point), where it is equal to 20% of the shear stress. Furthermore, this ratio is increasing in the direction of streaming.

By using the scaling laws suggested in the paper one may explore the increasing significance of the normal stress terms in the direction of streaming as follows:

$$\frac{u'^2 - v'^2}{U_0^2} = \Phi(\eta), \quad u'v' = U_0 U_e \Psi(\eta),$$

where  $\eta = y/(\theta Re_\theta^{0.2}) = yv^{0.2}U_e\theta^{-1.2}$  and  $U_e = C_u X^{-0.21}$  and this leads to the expression

$$\frac{\partial}{\partial x}(u'^2 - v'^2) \bigg/ \frac{\partial}{\partial x}(-u'v') = CX^{0.37}.$$

By calculating the average ratio for  $0.7 < \eta < 0.9$  and plotting it against  $X$  the estimated exponent of 0.37 can be observed. Although the accuracy of this procedure is limited, the increasing significance of the normal stresses with  $X$  is important. A number exceeding 20% suggests that one cannot neglect the role of the normal stresses in the similarity analysis.

### A.3. A discussion of the suggested equilibrium

Although the normalized mean velocity profiles collapse fairly well (figure 28*a*) and  $A$  is almost constant in the streamwise direction, the flow is not necessarily in equilibrium. Our measurements indicate that the mean motion, the shear stress and the normal stresses require different scaling. Moreover the significance of the normal stress increases in the direction of streaming. It thus represents typical behaviour of a boundary layer that is not in a state of equilibrium.

## REFERENCES

- BRADSHAW, P., FERRISS, D. H. & ATWELL, N. P. 1967 Calculation of boundary layer development using the turbulent energy equation. *J. Fluid Mech.* **28**, 593–616.
- CASTILLO, L. & GEORGE, W. K. 2000 Similarity analysis for turbulent boundary layer with pressure gradient: the outer flow. *AIAA Paper* 2000-0913.
- CHANG, P. K. 1976 *Control of Flow Separation*. Hemisphere.
- DENGEL, P. & FERNHOLZ, H. H. 1990 An experimental investigation of an incompressible turbulent boundary layer in the vicinity of separation. *J. Fluid Mech.* **212**, 615–636 (referred to herein as DF).
- FERNHOLZ, H. H. 1993 Management and control of turbulent shear flows. *Z. Angew. Math. Mech.* **73**, 287–300.
- GAD EL HAK, M., & BUSHNELL, D. M. 1991 Separation control: review *Trans. ASME I: J. Fluids Engng* **113**, 5–29.
- GASTER, M., KIT, E. & WYGNANSKI, I. 1985 Large scale structures in a forced turbulent mixing layer. *J. Fluid Mech.* **150**, 23–39.
- GEORGE, W. K. & CASTILLO, L. 1993 Boundary layers with pressure gradient: another look at the equilibrium boundary layer. In *Near Wall Turbulent Flows* (ed. R. M. C. So et al.), pp. 901–910. Elsevier.
- HESKESTAD, G. 1965 Hot-wire measurements in a plane turbulent jet. *Trans. ASME E: J. Appl. Mech.* **32**, 721–734.
- HINZE, J. O. 1959 *Turbulence* McGraw-Hill.
- LACHMANN, G. (Ed.) 1961 *Boundary Layer and Flow Control, its Principles and Applications*, vols. I and II. Pergamon.
- LIEBECK, R. H. 1973 A class of airfoils designed for high lift in incompressible flow. *J. Aircraft* **10**, 610–617.
- LUEPTOW, M., BRUER, K. H. & HARITONIDIS, J. H. 1988 Computer-aided calibration of x-probes using a look-up table. *Exps. Fluids* **6**, 115–118.
- NISHRI, P. 1996 On the dominant mechanisms governing active control of separation. PhD thesis, Tel-Aviv University.
- PATRICK, W. P. 1987 Flowfield measurements in a separated and reattached flat plate turbulent boundary layer. *NASA CR-4052*.
- PERRY, A. & SCHOFIELD, W. H. 1973 Mean velocity and shear stress distributions in turbulent boundary layers. *Phys. Fluids*, **16**, 2068–2074.
- SIMPSON, R. L. 1989 Turbulent boundary-layer separation. *Ann. Rev. Fluid Mech.* **21**, 205–234.
- SKARE, P. E. & KROGSTAD, P. A. 1994 A turbulent equilibrium boundary layer near separation. *J. Fluid Mech.* **272**, 318–348 (referred to herein as SK).
- SPANGENBERG, W. G., ROWLAND, W. R. & MEASE, N. E. 1967 Measurements in a turbulent boundary layer maintained in a nearly separating condition. In *Fluid Mechanics of Internal Flow* (ed. G. Sovran), pp. 110–151. Elsevier.
- STRATFORD, B. S. 1959a The prediction of separation of the turbulent boundary layer. *J. Fluid Mech.* **5**, 1–16.
- STRATFORD, B. S. 1959b An experimental flow with zero skin friction throughout its region of pressure rise. *J. Fluid Mech.* **5**, 17–35.
- TOWNSEND, A. A. 1976 *The Structure of Turbulent Shear Flow*, 2nd Edn. Cambridge University Press.
- TUMIN, A., LIKHACHEV, O. & WYGNANSKI, I. 1998 On harmonic perturbations in turbulent shear flows. *Bull. APS* **43**, 2079.
- WYGNANSKI, I. 1997, Boundary layer and flow control by periodic addition of momentum. *AIAA Paper* 97-2117.





## On streamwise vortices in a turbulent wall jet that flows over a convex surface

O. Likhachev,<sup>a)</sup> R. Neuendorf, and I. Wygnanski<sup>b)</sup>

*Department of Aerospace and Mechanical Engineering, The University of Arizona, Tucson, Arizona 85721*

(Received 18 February 2000; accepted 22 February 2001)

Flow visualization and correlation measurements revealed the existence of large streamwise vortices in a turbulent wall jet that is attached to a circular cylinder. These coherent structures were not to be found near the nozzle, nor were they artificially triggered, thus the vortices could be a product of centrifugal instability. The existence and scale of this large-scale coherent motion were corroborated by stability analysis applied to the measured mean flow. © 2001 American Institute of Physics. [DOI: 10.1063/1.1366678]

The existence of streamwise vortices resulting from centrifugal instability is anticipated in turbulent shear flows (see, e.g., Tani,<sup>1</sup> So and Mellor,<sup>2</sup> Barlow and Johnston,<sup>3</sup> Patel and Sotiropoulos<sup>4</sup>) but it was not observed in an unambiguous manner. Tani, in his seminal investigation of a boundary layer over a concave surface in the absence of pressure gradient, clearly observed the production of longitudinal vortices in laminar flow but only estimated their scale in a turbulent flow. The estimate was made by determining the vertical undulations of the loci of constant mean-velocity lines across the span, in the outer part of the turbulent boundary layer. Since the wave number of these undulations and their phase did not change in the direction of streaming while the boundary layer thickness increased approximately fourfold over the corresponding distance, one cannot but wonder if these vortices were not generated by some regularly spaced, upstream protuberances. Nevertheless, when Tani replaced the viscosity in the parallel stability analysis of Smith<sup>5</sup> by a constant eddy-viscosity derived from the experiments of Clauser<sup>6</sup> he was able to correlate the spanwise scales observed in his experiment with the most amplified longitudinal vortices derived from the linearized equations of motion. In general, curvature effects in a boundary layer are intertwined with pressure gradient effects that may lead to flow separation and further complicate the analysis. Patel and Sotiropoulos,<sup>4</sup> who carefully reviewed the publications related to boundary layer flows over curved surfaces concluded that, "For concave curvature the mystery of Taylor-Görtler vortices remains unresolved, the laboratory data being inconclusive." They suggest that the flow is three dimensional and should be treated as such both in the laboratory and in numerical analysis.

A turbulent wall jet evolving over a convex surface spreads out much more rapidly than its counterpart over a straight surface, most probably due to a centrifugal instability that is akin to the one occurring in a boundary layer over

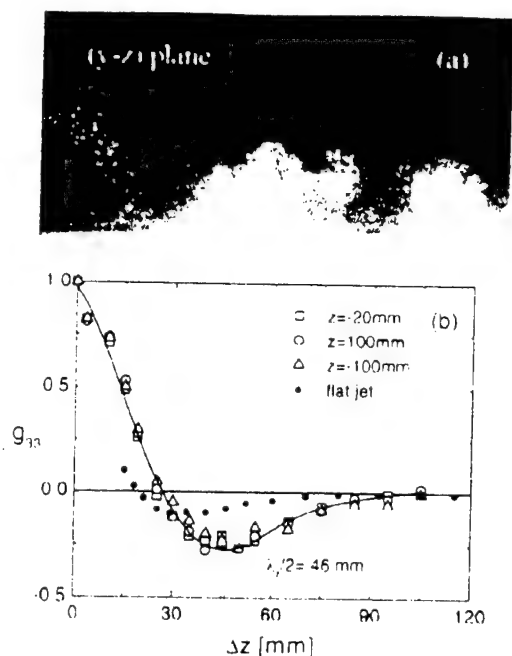
a concave wall. In the simplest configuration there is no external flow and no externally generated pressure gradient. One may even consider an equilibrium flow by tailoring the curvature of the surface to yield a constant ratio between the radius of curvature and the local width of the jet (Guitton<sup>7</sup>). However, no streamwise vortices were observed to date in this flow, in spite of the meticulous search by Guitton for the tale telling spanwise variations in the surface shear stress. Both Guitton<sup>7</sup> and Fekete<sup>8</sup> observed a great sensitivity of the flow to imperfections at the nozzle lip, which could result in such steady spanwise variations and imply a predisposition of the flow to steady streamwise vortices. Such a predisposition may be triggered by isolated roughness spots or by vortex generators in a boundary layer as well. Streamwise vortices were triggered on a curved laminar and transitional wall jet by sucking through discrete holes near the origin of the flow (Mattson<sup>9</sup>). It is hard to discern from this study whether the instability would have been triggered naturally and whether it survives in a turbulent environment.

We were also puzzled (Neuendorf and Wygnanski<sup>10</sup>) by the large differences in the spreading rate between the wall jet flowing over a circular cylinder and that over a flat surface because the normalized mean velocities in both flows are almost identical. These differences could not be attributed to pressure gradient either because the surface pressure is approximately constant up to an azimuthal angle  $\theta$  (measured from the nozzle) of  $130^\circ$ . At some locations the difference in the rate of spread of the two compared flows approaches an order of magnitude. This is particularly obvious at larger streamwise distances and it depends on the slot height, from which the jet emanates (Fig. 9 of Neuendorf and Wygnanski<sup>10</sup>). The turbulence level in the curved flow is also much higher than in the corresponding straight wall jet.

Since we could not attribute the differences listed to local roughness spots (this idea was carefully checked), centrifugal instability remained as a sole possibility and for this reason the following investigation was undertaken. The cylinder used in the investigation is highly polished and has a radius  $R = 101.6$  mm. There is a smooth contraction leading to a 2.34 mm high slot. The Reynolds number based on the

<sup>a)</sup> Author to whom correspondence should be addressed. Electronic mail: oleg@u.arizona.edu

<sup>b)</sup> Also at: Department of Fluid Mechanics and Heat Transfer, Tel-Aviv University.

FIG. 1. (a) Flow visualization and (b) cross correlation at  $(\theta - \theta_0) = 160^\circ$ 

slot height and on the velocity emanating from the slot was  $Re = 33 \times 10^4$ .

A comprehensive search for the streamwise vortices that might occur naturally in this flow was undertaken. It consisted of flow visualization, particle image velocimetry (PIV), and cross-correlation measurements using hot wire anemometry. The experimental results were backed by stability calculations. The PIV results will not be discussed in this Brief Communication. Flow visualization [Fig. 1(a)], that used smoke as tracer particles and a laser sheet that illuminated the plane normal to the flow direction, clearly revealed the existence of streamwise eddies. Figure 1(b) illustrates how the spanwise wavelength of the longitudinal vortices was determined. The measurements were made using two hot wire probes containing each a "V" type array that was capable of measuring the streamwise and spanwise components of velocity near the solid surface. The probes were separated by a spanwise distance,  $\Delta z$ , and the correlation coefficient  $g_{33}$  is defined in a conventional manner [i.e.,  $g_{33} = u'_z(z) \cdot u'_z(z + \Delta z) / \sqrt{u'^2_z(z)} \sqrt{u'^2_z(z + \Delta z)}$  where  $u'_z$  represents the spanwise velocity fluctuations]. The data presented in Fig. 1(b) were acquired at an azimuthal angle  $(\theta - \theta_0) = 160^\circ$ . Streamwise vortices would generate alternating directions in the spanwise velocity component near the surface. The  $u_z$  component provides the strongest indication for the existence of streamwise large-scale vortices since the normal component  $u_n$  vanishes near the wall and the  $u_n$  component represents a secondary effect (i.e., a downward motion brings in high-momentum fluid to the vicinity of the surface that increases the local velocity and vice versa). In the example shown, the  $g_{33}$  correlation attained a minimum value of  $-0.25$ , when the spanwise separation between the probes was approximately 46 mm. It implies that the aver-

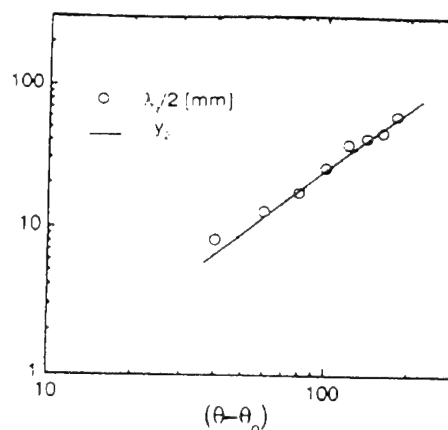


FIG. 2. Wavelength of the streamwise vortices vs downstream location

aged spanwise dimension of a counter-rotating pair of the streamwise vortices is twice as large at this streamwise location. This correlation was invariant to the spanwise,  $z$  location of the stationary probe measuring  $u'_z(z)$ . The scale of vortices shown in the above-mentioned photograph was in agreement with the scales deduced from correlation measurements. When the procedure was repeated at various azimuthal angles along the cylinder (for  $40^\circ < \theta < 180^\circ$ ), it became clear that the wavelength of the streamwise vortices,  $\lambda_z$ , increased with  $\theta$  (Fig. 2). It is most probably achieved by coalescence of like vortices since a preliminary PIV study shows that the total circulation of the averaged longitudinal vortex pattern increases with downstream location. However, the investigation of the merging process is beyond the scope of the present note. It turns out that  $\lambda_z$  scales with the local width of the flow,  $y_2$ , providing the following relationship:  $\lambda_z \approx 2y_2$ , which suggests that the vortices encompass the entire width of the jet (the solid line represents the mean length scale  $y_2$  at various downstream locations).

In order to demonstrate that the  $g_{33}$  correlation is meaningful, the same measurements were repeated in a wall jet flowing over a flat surface and also shown in Fig. 1(b). The minimum correlation recorded in this case was only  $g_{33} = -0.1$  (i.e., a factor of 2.5 smaller) and the wavelength established from this correlation did not scale with the width of the flow,  $y_2$ , but rather with a viscous length  $\Delta z \cdot U_{\max}^{-1/2}$  that is characteristic of classical wall jets.<sup>10</sup> When vortex generators were placed on the surface the spanwise correlation regained its minimum value  $g_{33} = -0.25$ , indicative of the streamwise vortices that were imposed on this flow. Thus the minimum value of  $g_{33}$  measured on the curved wall jet is also indicative of the streamwise vortices existing in this flow.

Calculations have been carried out to evaluate stability of the turbulent wall jet flowing over a circular cylinder with respect to the Görtler-type perturbations. One assumes that the longitudinal vortices generated are a manifestation of a linear centrifugal instability of the mean velocity profile. They can be presented in the form of three-dimensional, steady, spatially growing disturbances imposed on the primary mean flow and have the form

$$\begin{aligned}
(\tilde{u}, \tilde{v}) &= U_{\max} [A(\theta) [\hat{u}(\eta), v(\eta)] + O(\epsilon)] \\
&\quad \times \cos(\beta z) \exp\left(\int_{\theta_0}^{\theta} \hat{\gamma} d\theta\right), \\
\tilde{w} &= U_{\max} [A(\theta) w(\eta) + O(\epsilon)] \sin(\beta z) \exp\left(\int_{\theta_0}^{\theta} \hat{\gamma} d\theta\right), \\
\tilde{p} &= U_{\max}^2 [A(\theta) p(\eta) + O(\epsilon)] \cos(\beta z) \exp\left(\int_{\theta_0}^{\theta} \hat{\gamma} d\theta\right),
\end{aligned} \quad (1)$$

representing asymptotic expansion on the small curvature parameter,  $\epsilon = y_2/R$ , which is a ratio of two length scales that govern boundary layer type flows with streamline curvature. Here,  $(\tilde{u}, \tilde{v}, \tilde{w})$  denote components of velocity in cylindrical coordinates  $(r, \theta, z)$ ,  $\tilde{p}$  is the pressure perturbation,  $\beta = y_2 2\pi/\lambda_z$  the transverse wave number, made dimensionless with the local width of the jet,  $y_2 = C_v(\theta - \theta_0)^m$ ;  $U_{\max} = C_l(\theta - \theta_0)^n$  is the maximum velocity of the basic flow, and  $\eta = (r - R)/y_2$  denotes the nondimensional distance from the cylinder, while  $\hat{\gamma}$  is the amplification rate. Substituting solution (1) into perturbation equations and making use of the transformations  $\gamma = \epsilon \text{Re } \hat{\gamma}$ ,  $u = \epsilon \text{Re } \hat{u}$ , and  $q = \text{Re } p$ , one gets, at leading order on the small curvature parameter, the linear stability equations of the form

$$\begin{aligned}
\gamma U u + \text{Go}^2 U' v + V u' + C U (2nu - m \eta u') &= u'' - \beta^2 u, \\
\gamma U v + (V v)' + C U (nv - m \eta v') - 2U u &= -q' + v'' - \beta^2 v, \\
\gamma U w + V w' + C U (nw - m \eta w') &= \beta q + w'' - \beta^2 w, \\
\gamma u + \text{Go}^2 (v' + \beta w) + C U (nu - m \eta u') &= 0.
\end{aligned} \quad (2)$$

Here, the prime denotes differentiation with respect to  $\eta$ ,  $\text{Re} = y_2 U_{\max}/\nu$  is the local Reynolds number based on an eddy viscosity that is evaluated from experimental data<sup>10</sup> by using the Boussinesq eddy viscosity model for the turbulent stresses and averaged across the flow;  $\text{Go} = \text{Re} \sqrt{\epsilon}$  is the Gortler number;  $C = \text{Re } y_2/x$  represents the constant factor that is  $C \sim 4.8$  in the region of flow similarity  $[(\theta - \theta_0) = 40^\circ - 160^\circ]$ . Here,  $x = R(\theta - \theta_0)$  is a coordinate along a surface. The mean velocity profile,  $U/U_{\max} = (U/V/\text{Re})$ , that matched the experimental data of Neuendorf and Wygnanski<sup>10</sup> has been used in the stability analysis. One assumes here that the effect of the random turbulence on the large-scale quasisteady streamwise vortices associated with the centrifugal instability is the same as on the mean flow, leaving  $\nu$ , unaltered. The system of equations (2), that is subject to homogeneous boundary conditions,

$$\begin{aligned}
u = v = w = 0 \quad \text{at } \eta = 0, \\
u = v = w = 0 \quad \text{at } \eta \rightarrow \infty,
\end{aligned} \quad (3)$$

represents an eigenvalue problem with respect to  $\gamma(\beta, \text{Go})$ , and the Riccati factorization method was used for its solution. It is believed [Eq. (2)] that some and perhaps most of the nonparallel effects are accounted for by the local stability calculations. The amplitude function  $A(\theta)$  remains arbitrary when calculations are carried out at the leading order only. However,  $A(\theta)$  is determined by imposing the solvability

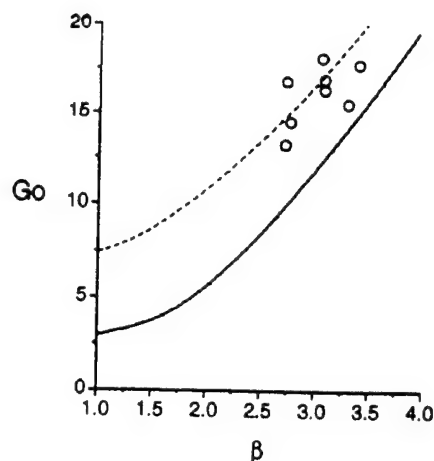


FIG. 3. Neutral stability diagram representing the longitudinal vortices in the turbulent wall jet around a circular cylinder. The symbols correspond to experimental data.

conditions at the next level (see, e.g., Ref. 11). It is established that the nonparallel correction to the amplification rate,  $\hat{\gamma}$ , due to the slight divergence of the mean flow, is inversely proportional to  $\text{Re}$  for boundary-layer-type flows. It was neglected in the present stability analysis, since  $\text{Re} \sim 50$ .

Solutions to the system of Eq. (2) do not depend explicitly on the curvature parameter or on the Reynolds number; however, the growth rate and scale of the velocity perturbations in the direction of streaming depend on a particular experimental setup even for the same value of the Gortler number. The calculated neutral stability curve,  $\hat{\gamma} = 0$ , is denoted in Fig. 3 by the solid line. The symbols represent scale of vortices measured at various streamwise locations depicted in Fig. 2. The neutral curve calculated in the classical manner of Gortler, by equating the factor  $C$  and consequently the divergence velocity,  $V$ , to zero, is also shown in Fig. 3 by the dashed line. One notes that the divergence of the wall jet has a strong destabilizing effect, even if it was not fully accounted for in the present calculations as discussed previously. The present calculations support the hypothesis that the observed vortices are a manifestation of a centrifugal instability.

The large coherent structures observed in turbulent shear flows such as the mixing layer, the wall jet, or the turbulent boundary layer in an adverse pressure gradient can be viewed as predominant instability modes. This point of view provides a basis for the enhancement of mixing, and control of separation by periodic excitation. The present communication reveals that stationary, streamwise vortices generated by surface curvature can also be predicted by stability considerations; in this case a centrifugal instability.

## ACKNOWLEDGMENTS

The authors are grateful to M. D. Zhou and H. Zhou for the cross-correlation data obtained for the wall jet over a flat plate.

- <sup>1</sup>I. Tani, "Production of longitudinal vortices in the boundary layer along a concave wall," *J. Geophys. Res.* **67**, 3075 (1962).
- <sup>2</sup>R. M. C. So and G. L. Mellor, "Experiment on turbulent boundary layers on a concave wall," *Aeronaut. Q.* **26**, 25 (1975).
- <sup>3</sup>R. S. Barlow and J. P. Johnston, "Structure of a turbulent boundary layer on a concave surface," *J. Fluid Mech.* **191**, 137 (1988).
- <sup>4</sup>V. C. Patel and F. Sotiropoulos, "Longitudinal curvature effects in turbulent boundary layers," *Prog. Aerosp. Sci.* **33**, 1 (1997).
- <sup>5</sup>A. M. O. Smith, "On the growth of Taylor-Görtler vortices along highly concave walls," *Q. Appl. Math.* **13**, 233 (1955).
- <sup>6</sup>F. H. Clauser, "The turbulent boundary layer," *Adv. Appl. Mech.* **4**, 1 (1956).
- <sup>7</sup>D. E. Guitton, "Two-dimensional turbulent wall jets over curved surfaces," Report No. 64-7, McGill University, Department of Mechanical Engineering, 1964.
- <sup>8</sup>G. I. Fekete, "Coanda flow of a two-dimensional wall jet on the outside of a cylinder," Report No. 63-11, McGill University, Department of Mechanical Engineering, 1963.
- <sup>9</sup>O. J. E. Matsson, "Experiments on streamwise vortices in curved wall jet flow," *Phys. Fluids* **7**, 2978 (1995).
- <sup>10</sup>R. Neuendorf and I. Wygnanski, "On a turbulent wall jet flowing over a circular cylinder," *J. Fluid Mech.* **381**, 1 (1999).
- <sup>11</sup>M. Gaster, "On the effects of boundary-layer growth on flow stability," *J. Fluid Mech.* **66**, 465 (1974).

September 13, 2001

## ON LARGE STREAMWISE STRUCTURES IN A WALL JET THAT FLOWS OVER A CIRCULAR CYLINDER.

R. Neuendorf, L. Lourenco and I Wygnanski

### 1. Introduction

The effects of streamline curvature on turbulence generated in mixing layers were investigated by Margolis & Lumley [1965] and by Wyngaard *et al.* [1968]. Bradshaw [1969] and more recently Patel & Sotiropoulos [1997] reviewed the available literature concerned with the effects of streamline curvature on the turbulence in both wall bounded and free, turbulent shear flows. In his opening statement Bradshaw wrote: "Streamline curvature ... produces surprisingly large changes in the turbulent structure of shear layers. These changes are usually an order of magnitude more important than ... explicit terms appearing in the mean motion equations for curved flows."

Similar observations were made by Neuendorf & Wygnanski [1999, thereafter referred to as N&W] in their experimental investigation of the turbulent wall jet flowing over a circular cylinder (this flow is often referred to as the Coanda-Effect). They showed that:

- (i) The pressure distribution over the cylinder is approximately constant over one third of its circumference (i.e. from the nozzle where  $\theta = 0^\circ$  to  $\theta = 120^\circ$ , thereafter the pressure increases until it attains the ambient pressure where the flow separates around  $\theta = 220^\circ$ ).
- (ii) The normalized mean velocity profile is almost identical in the constant pressure region to its counterpart on a flat surface but the rate of spread of the flow over the cylinder is much larger.
- (iii)

The turbulent intensities are not in equilibrium with the mean motion, in contrast to the plane wall jet where they clearly are in such equilibrium. They continuously amplify under the influence of curvature, with the streamwise and radial normalized components ( $\sqrt{u'^2}/U_{\max}$ ,  $\sqrt{v'^2}/U_{\max}$ ) increasing their value within the constant pressure region by more than 50% over and above the plane flow. The spanwise component, ( $\sqrt{w'^2}/U_{\max}$ ) on the other hand, is not directly affected by curvature and increases near the surface due to second order effects. The comparison was made at corresponding locations determined by the mean velocity in the jet (i.e. at identical  $y/y_2$ , where  $y_2$  represents the width of the jet).

- (iv) The mean velocities measured close to the separation location do not contain new inflexion points as they do in boundary layers approaching separation. Since the mean flow is two-dimensional one may speculate that the separation may be occurring in cells that are not stationary in time.

The mean velocity profile, the rate of spread of the jet and the distribution of two transverse components of turbulent intensity, are re-plotted here for the sake of completeness (fig. 1 through 4). They provide the "raison d'être" for the present investigation although three of these plots (with the exception of  $\sqrt{w'^2}/U_{\max}$ ) appear in N&W.

Examination of the Reynolds averaged transport equations describing the production of each of the three components of the turbulent intensity and of the Reynolds stress do not provide an adequate explanation of the observations made. On the other hand, the presence of quasi-stationary streamwise vortices could generate three-dimensional distortions in the mean flow that could give rise to the large differences observed between the plane and the curved wall jets. The existence of streamwise vortices resulting from centrifugal instability is anticipated in curved turbulent shear flows (Tani 1962, Patel *et al.* 1997) but they were not observed in an unambiguous manner. Tani in his seminal investigation of a boundary layer over a concave surface in the absence of pressure gradient, observed the existence of longitudinal vortices in laminar flow, but he could only estimate their scale if they were to prevail in turbulent flow. In this case, one could also suspect that the vortices inferred from a velocity signal, were generated by some regularly spaced, upstream protuberances. To date, streamwise vortices were not

observed in a wall jet flowing over a convex surface, in spite of the meticulous search by Guitton [1970] for the tale telling spanwise variations in the surface shear stress. Both Guitton (1970) and Fekete (1963) also observed the great sensitivity of the flow to imperfections at the nozzle-lip that could result in steady spanwise variations and imply a predisposition of the flow to steady streamwise vortices. Such a predisposition may exist in a boundary layer as well resulting in streamwise vortices that are triggered by isolated roughness spots or by vortex generators.

Two point correlation measurements accompanied by flow visualization that followed (O. Likhachev, R. Neuendorf, and I. Wygnanski, 2001), suggested the presence of streamwise vortices in the Coanda-type flow but these observations could not define quantitatively the size and strength of these vortices. Multi-point correlation techniques in general, that evolved around the hot-wire anemometer, enable one to construct a simple model of a time averaged eddy consistent with the measurements, but they provide no proof for the existence of such an eddy at any moment in the flow (see Townsend 1956 & 1973). For this reason an investigation using a particle image velocimeter (hereafter referred to as PIV) was initiated as it provides instantaneous information about the state of the flow in a plane that is illuminated by a laser-light-sheet. It may therefore map the vortices seen.

## 2. Brief Description of the Experimental Apparatus

The experiments were performed in a facility built at McGill University by Professors Newman and Fekete and described in N&W. It was evident from the beginning that flow quality depends significantly on the design of the facility. Many experimental setups favored an external settling chamber and nozzle that interfered with the wall jet after the latter turned  $180^\circ$  around the surface of the cylinder. As a consequence, the flow developed early three-dimensionalities that resulted in a shorter constant pressure region and earlier flow separation.

The cylinder was mounted in a steel framework, about 1.30 m above the floor, inside two large end-plates that allowed rotating the cylinder about its axis in order to vary the downstream location of the measurements. The large clearance between the cylinder and the floor or the ceiling helped to establish a steady outer boundary condition of  $U_\infty = 0$  regardless of the rotational angle of the cylinder. The independence of the flow field from the angle of rotation was established by repeated surface pressure measurements and hot-wire measurements at constant distance from the nozzle,  $\theta$ , but at various angles of nozzle relative to fixed laboratory coordinates. No effect on either pressure or velocity was observed. The two-dimensionality of the mean flow throughout the self-similarity region ( $\theta = 40^\circ - 120^\circ$ ) was checked and validated by a momentum balance (see N&W).

The concept of PIV is fairly simple. The fluid is seeded with small tracer particles and illuminated twice by a thin sheet of monochromatic light. The light scattered by the tracer particles is recorded on a CCD, cross-correlation camera. The information stored can be extracted at a later time.

The optical set-up used for this investigation consisted of two Spectra-Physics Quanta-Ray GCR series Nd:Yag lasers, a DANTEC light-guide system and light-sheet optics. Each pulse has a duration of 6-7ns, and a total energy of 650mJ. The pulse energy stability is good with a variance that is smaller than 3%. By mounting all optical components onto a single rigid base-plate a long term beam overlap and pointing stability is ensured. The optimum pulse repetition rate is 3 Hz. The delay between the two laser pulses is controlled by electronic delay circuitry and verified by measuring the Q-switch synchronization of the laser power supplies. The recording system consisted of a KODAK MEGAPLUS Camera, Model ES 1.0 which captures up to 30 eight-bit images per second with a spatial resolution of over one million pixels. The heart of the camera is a CCD (charge coupled device) interline transfer sensor which has a pixel array of 1,008(H) x 1,018(V) with progressive scan readout. Each pixel measures nine microns square with a 60 percent fill factor using a microlens. Image enhancement circuitry assures maximum image uniformity. In contrast to the more common interline transfer CCD sensor this sensor is capable of shuttering and storing the entire array of pixels, not just every other line. Thus, this sensor offers full vertical resolution when the CCD is used in shuttered mode. Two different lenses of 105mm and 50mm focal length were used. The distortion and magnification of the system was measured by recording test images of known size and shape. Within the accuracy of the system the results showed no errors.

Oil droplets were used as tracer particles. They were generated in a six-jet atomizer made by TSI (Laskin nozzle). High-pressure air that is injected into the seeding liquid forms small droplets that are released by the atomizer. Larger particles, on the other hand, are captured by an impact sphere located in front of the jet-nozzle. The atomizer incorporates built-in dilution air, useful in establishing an output



particle concentration range. Several liquids were tested and the best results were achieved with a solution of one part polyethylene-glycol (PEG600) dissolved in 5 parts water. The average particle diameter was approximately  $1\mu\text{m}$ . The mean diameter depends largely on the type of liquid being atomized. There is little sensitivity to the operational pressure of the atomizer. The advantage of PEG is that it remains suspended in air at rest for a very long time ( $>1\text{hour}$ ) and it is non-toxic.

The goal of good flow seeding is to obtain uniform seeding density in the region of interest. Unfortunately, two essential features of the curved wall jet complicate uniform seeding throughout the whole flow field. These are, respectively, strong entrainment and separation of the jet from the wall. The seeding, introduced into the jet was quickly diluted by mixing with entrained ambient fluid. To prevent this dilution the whole experiment was enclosed in a plastic tent that was big enough and did not alter the free boundary conditions yet it was small enough to fill up quickly with smoke. The seeding was initiated approximately 2-3 minutes prior to the data acquisition in order to obtain a uniform seeding density.

To produce a high resolution displacement field from the digital image pairs an image-matching approach described by Lourenco & Krothapalli *et al.* (1998) was employed. This algorithm enabled us not only to resolve accurately large gradients in the velocity field but also permitted measurements close to the surface. For further information refer to Krothapalli *et al.* (1999).

### 3. Pattern Recognition Technique

Coherent structures in turbulent shear flows are assumed to be a product of the leading instabilities. They therefore, dominate the turbulent transport of momentum and heat across the flow and alter, to a large extent, the mean (time averaged) character of the flow. In general, instability occurs because an equilibrium among external forces is disturbed. These forces are many: inertia, viscous, centrifugal, buoyancy, to mention a few. Some linear (mostly initial) instabilities, are time dependent (e.g. Tollmien Schlichting instability) while other generate stationary spatial undulations (Gortler instability). Most second order instabilities contain perturbations of both categories because second order products give rise to harmonics and to mean flow distortion concomitantly.

In order to describe time dependent periodic coherent structures in turbulent flow statistically, one has to ensemble average the data collected in a meaningful way. This can be achieved by introducing small amplitude periodic perturbations into the basic flow at a priori known, or assumed to be known dominant mode. The seeds for technique were sown by Schubauer and Skramstad (1948) who introduced periodic perturbations in a laminar boundary layer to trigger a theoretically known instability, i.e. to initiate T.-S. waves. This breakthrough technique became a major diagnostic tool for studying flow-stability and it was extended to free turbulent shear flows, like the mixing layer by Oster *et al* (1978) and by Gaster *et al* (1985). By using the external excitation as a diagnostic tool one may minimize some major problems stemming from imperfect periodicity, phase jitter, and variation in size and in shape of the individual structures. Furthermore, it provides a phase reference enabling the subsequent triple decomposition of the data into time-mean, coherent and random constituents.

In order to chart an unknown turbulent coherent structure (e.g. a turbulent spot in a laminar boundary layer), Schubauer and Klebanoff (1956) used an impulse emanating from a point in the flow. Since the impulse had to be both short and powerful they used an electric discharge (a spark) to destabilize the flow in time and in space. A less powerful impulse helped Gaster & Grant (1975) to map the evolution of a wave packet in a boundary layer in which the initially dominant, linear instabilities were superimposed. This method triggers both periodic in time and spatially evolving instabilities. It helped to prove the existence of very large coherent structures in a turbulent boundary layer in an absence of pressure gradient and curvature (Zilberman *et al* 1977). However, since most externally introduced perturbations, enhance the amplitude of the pre-selected instabilities above and beyond the level that they would have achieved naturally, they also modify the flow. This is the essence behind "active flow control" that enables the delay of separation and enhancement of mixing in turbulent flows.

A curved wall jet contains time dependent large structures that are identified with Kelvin-Helmholz instability in the outer region and T.S. near the wall but it may also contain spanwise distortions associated with a centrifugal instability of the Gortler type. The inner, boundary layer might be unstable when the surface is concave while the outer, jet like flow is unstable when the surface is convex. Therefore it is not a priori clear what instability dominates the flow without external intervention and triggering it by adding external perturbations might be artificial and therefore erroneous. Such attempts were made on a concave surface by Matsson (1995). He used jets at prescribed spanwise intervals to trigger longitudinal structures. Other methods used to initiate such structures include small roughness elements, vortex generators or

surface film heaters. In the present case where the local width of the flow changes with distance from the nozzle the structures resulting from a centrifugal instability may change in scale thus the imposition of fixed vortices may be artificial. Consequently, a different, less intrusive method was required. Thus pattern recognition in combination with a PIV became the system of choice as it is totally non-intrusive. Pattern recognition methods consider only the basic data itself out of which, via certain criteria, the structure of interest is deduced. The employed technique is described below.

The first step in recognizing the pattern requires enhancement of the acquired image. This is the most subjective part of the pattern recognition process and requires a cautious design of the enhancement operator. The effectiveness of enhancement process depends on the extent and accuracy of the prior knowledge that defines the nature of the data and the reasons for its degradation. The spectral characteristics of a signal are especially important for designing a filter and these characteristics can be easily obtained by the application of a Fourier transform to the signal acquired. In order to separate the waveform of the coherent structure from the noise, a narrow band-pass filter must be applied at the given peak frequency. The same procedure is followed now to the two-dimensional, PIV vorticity picture. The two-dimensional Fourier transform and its inverse transform are defined below:

$$F(\zeta_2, \zeta_3) = \int_{-\infty}^{\infty} \int_{-\infty}^{\infty} f(y, z) \exp[-j2\pi(y\zeta_2 + z\zeta_3)] dy dz \quad (1)$$

$$f(y, z) = \int_{-\infty}^{\infty} \int_{-\infty}^{\infty} F(\zeta_2, \zeta_3) \exp[-j2\pi(y\zeta_2 + z\zeta_3)] d\zeta_2 d\zeta_3 \quad (2)$$

where  $F$  represents a two-dimensional Fourier Transform and  $f$  represents its inverse. Since the units of  $\zeta_2$  and  $\zeta_3$  are also reciprocals of  $y$  and  $z$ , just as the frequency  $\omega$  is reciprocal of the time  $t$ ,  $\zeta_2$  and  $\zeta_3$  are also referred to as frequencies. They are spatial frequencies and describe changes per unit length. The independent variables  $y, z, \zeta_2$  and  $\zeta_3$  in the equation above are chosen to be consistent with the coordinate system of the PIV data. Furthermore, the spatial frequency  $\zeta_3$  is proportional to  $1/\lambda_z$ , where  $\lambda_z$  is the spanwise wavelength of the most probable streamwise structure. Figures 5 and 6 show an instantaneous vorticity contour image  $f(y, z)$  and its Fourier transform  $F(\zeta_2, \zeta_3)$ , respectively. The Fourier transform  $F(\zeta_2, \zeta_3)$  is plotted in wrap-around order with the origin - mean vorticity of the whole image - in the center of the plot. It can be seen in figure 6 that the vorticity has most of its energy concentrated in a small region in the frequency domain near the origin and along the  $\zeta_2$  and  $\zeta_3$  axis. One reason for the energy concentration near the origin is that the velocity field data typically have large regions where the vorticity changes slowly (the fluid is viscous). This is to some extent because of the weak nature of the observed longitudinal structures, which do not create any significant gradients in the flow. Note also the vorticity concentration along the  $\zeta_2$  and  $\zeta_3$  axis due to the rectangular window used to obtain a finite-extent of the image. The total energy contained in these artifacts is, however, small and does not affect the more important low frequency regions in the image. Therefore, it will not be necessary to apply a window function to the data prior to the transformation. A more quantitative presentation for the result of the Fourier transform  $F(\zeta_2, \zeta_3)$  is given in figure 7. It shows the positive axis of a cut through the origin in  $\zeta_2$ -direction. This information is most helpful for the proper design of the filter as it shows the vorticity spectrum as a function of the spanwise frequency  $F(\zeta_3)$  at  $\zeta_2 = 0$ , which is in the spanwise direction  $z$ . The dashed line in the same figure represents the Fourier transform of the single realization presented in figure 5. The solid line shows the mean curve for the complete data-set containing 500 images. Analogously to the one-dimensional example presented above, a finite impulse response (FIR) filter is used to reduce the influence of random noise on the image. After the filter was designed, it was applied to the images. Instead of using a numerically cumbersome convolution of the impulse response of the filter function  $h(y, z)$  with the individual images  $f(y, z)$ , the convolution theorem suggested that the filtering is the convolution of both functions

The advantage of this method stems from its reduced computational effort. In the present case of a  $64 \times 64$  array the improvement is approximately two orders of magnitude. Figure 8 shows the result of the



low-pass filter for the example chosen and plotted in figure 5. The difference between these two images is apparent. The vorticity distribution in the unfiltered image exhibits a large number of very strong and small vortices while the low-pass filtered data (see figure 8) show fewer but larger vortices. Apparently, the latter agrees better with the somewhat subjective definition of vortices, see figure 5. Overlaid on top of the contours are ellipses, representing the approximate size, shape and location of several vortices, reconstructed from the vector field. Note for example that vortex A exhibits two strong vorticity peaks in the unfiltered image although the velocity field suggests the presence of a large single vortex. Although the filter reduces the peak levels of vorticity in the image, the final image of the longitudinal structures will not be affected as this stage of the pattern recognition only enhances the signal-to-noise ratio for the follow-on "Feature Extraction" procedure. After all the images were low-pass filtered, vorticity levels that were less than 20% of the maximum were set to be zero. This "noise clipping" was performed to provide additional immunity from noise. Similarly to the previous design of the low-pass filter the level of clipping depends on the extent and accuracy of our prior knowledge about the noise characteristics of the data. Fine-tuning to fit the data is required. Several tests with threshold values ranging from 5% to 50% of the maximum value were therefore performed. Two criteria that are important for the following *Feature Extraction* were considered. First, the shape of the vortex had to be well represented by the remaining vorticity and second, a separating line to the neighboring islands was necessary, see figure 9. The tests showed that a threshold of about 20% of the maximum value fulfilled those requirements best.

#### 4. Cross Sectional Mean Flow Distribution

In contrast to the conventional PIV setup with the illumination plane being in the direction of streaming, it was necessary for the present work to place the light sheet in the jet cross-flow plane. The jet is thereby orthogonal to the laser sheet. The PIV measurements were conducted at four equally spaced streamwise locations. The first three stations were in the self-similar region at  $\theta = 40^\circ$ ,  $80^\circ$ , and  $120^\circ$ , the final station was in the adverse pressure gradient region where the local surface pressure had increased by 25% relative to its constant value upstream, i.e. at  $\theta = 160^\circ$ . Unfortunately, the experimental setup did not allow data acquisition at any location further downstream. 500 images were acquired at each measuring position and averaged to ensure convergence of the results. The measurements yielded two component of mean velocity  $\bar{v}$ ,  $\bar{w}$ , and three components of the Reynolds stress tensor  $\sqrt{\bar{v}^2}/U_{\max}$ ,  $\sqrt{\bar{w}^2}/U_{\max}$ , and  $\bar{v}'w'/U_{\max}^2$ . Based on the measurement of the  $\bar{v}$  and  $\bar{w}$  components of velocity the streamwise component of the mean vorticity  $\Omega_x$  was computed using central differences. Most of the PIV results will be presented in contour form; see, for instance, figure 12a. The horizontal axis represents the cylinder surface and the origin at (0,0) coincides with the center of its span. The profile next to the contour plot, when given, represents the spanwise average of the plotted component - in the case of figure 10b it is  $\bar{v}/U_{\max}$ . The velocities are normalized by the local maximum velocity,  $U_{\max}$ , and the length-scales by the local half-width,  $y_2$ .

Before discussing the streamwise development of the flow, the accuracy of the PIV data was assessed by comparison with hot-wire measurements made at the same  $\theta$  location. Hot wire and PIV data is shown for  $\theta = 80^\circ$ , where the hot-wire measurements were made along the center span of the cylinder. Single wire data, X-wire or V-wire data were used for this comparison. The two different dual-wire probes were used to minimize the influence of the mean velocity gradient in the wall boundary layer. The mean vorticity,  $\Omega_x$ , contours and the local mean velocity vectors in the cross-sectional plane ( $\theta = 80^\circ$ ) are plotted in figure 10a. Note that in the outer part of the wall jet ( $y/y_2 > 1$ ) the entrained flow, having  $\bar{v} < 0$ , is nearly perfectly two-dimensional. Most of the velocity vectors are of equal length across the span, they are parallel and directed towards the wall. The vectors in the boundary layer are oriented in the opposite direction. A  $\bar{v}$ -component "stagnation line" between those two regions is formed at approximately  $y/y_2 = 1$ . The term "stagnation line" might be misleading as it applies to the cross-plane flow only, but it is used here to emphasize the region where the secondary velocities,  $\bar{v}$  and  $\bar{w}$ , equal zero. The strong entrainment in the outer shear layer becomes more apparent in figure 10b where the averaged velocity profile  $\bar{v}/U_{\max}$  is shown. Note that the radial component  $\bar{v}$  exceeds 5% of  $U_{\max}$  even far beyond  $y = 2y_2$ . The streamwise component  $\bar{u}$ , measured with a PIV (with illumination in the  $R, \theta$  plane) almost vanished at this location (figure 11). A significant discrepancy in the results for the radial velocity component

generated by the two measurement systems is also shown in figure 11 (more details about the hot-wire technique used here see Neuendorf & Wygnanski 1999). The differences reflect the well-known problems of hot-wire anemometry in highly intense turbulent flows. The large errors in the outer shear layer region stem from the fact that both  $\bar{v}/\bar{u}$  and  $\bar{u}'/\bar{u}$  are of order unity. This may even lead to rectification of the hot-wire signal or exceedance of the calibration table. The mean velocities calculated from the continuity equation (black solid triangles) are plotted in the same figure and are based on single wire probe measurements of the streamwise velocity component  $u$  and the assuming that the mean flow is two-dimensional. The PIV results agree quite well with the calculated data up to  $y/y_2 = 1.8$ , thereafter the two curves diverge due to the shortcomings of the hot wire anemometry (fig. 11). The PIV is a better instrument in this case, as long as the seeding is sufficiently homogeneous and the velocity component normal to the plane of illumination is small.

Contours of the normalized turbulence intensities,  $\sqrt{v'^2}/U_{\max}$  and  $\sqrt{w'^2}/U_{\max}$ , are shown in figure 12, contours of  $v'w'/U_{\max}^2$  were measured but their value was too small to be of significance. The mean secondary shear stress averaged over the span,  $\overline{v'w'}/U_{\max} = 0$  across the flow. There is an excellent uniformity of the turbulent intensities along the span in the outer region while some non-uniformity emerges in the wall boundary layer. One has to bear in mind, however, that the results represent an average of 500 images only. This number represents an ensemble average that is less than one percent of the typical time series used in creating averages with a hot wire anemometer. The hot-wire measurements taken in the mid span plane are plotted in figures 12b and d for comparison. The agreement between the two methods of measurement is good although differences occur in the outer and inner extremities of the flow. In the outer region the CTA is mostly in error while in the inner region it is probably the PIV. The discrepancy in the wall region may be attributed to lower spatial resolution of the PIV system and to surface reflections that could not be eliminated. Surface reflections prevented the gathering of useful data near the wall. The hot-wire systems using V-wire probes is useful near the surface. Since the focus of this study pertains to the development of large-scale longitudinal structures, the apparent deficiencies of the PIV system in the vicinity of the wall are inconsequential.

## 5. Spatial Triple-Decomposition of PIV Data

The large effects of curvature on the evolution of the wall jet that were discussed in the introduction are attributed to the existence of longitudinal structures that directly increase the production of  $\overline{v'^2}$ ,  $\overline{w'^2}$ . The increase of the streamwise component,  $\overline{u'^2}$ , is thought to be a second order effect attributed to the longitudinal structures as well. However, the ensemble-averaged results from the PIV system did not show "significant" spanwise non-uniformities in mean velocities and in turbulent intensities. These results may even suggest that spatially steady longitudinal structures are absent in this flow. Two-point-cross-correlation measurements using a "V" type probe and theoretical considerations suggest otherwise (Likhachev, Neuendorf, and Wygnanski, 2001). Apparently, these counter-rotating longitudinal structures are sufficiently unsteady so as not to produce any spanwise variation in the mean but regular enough to generate significantly negative correlation.

In order to map the longitudinal structures in this turbulent wall jet and assess their contribution to the flow, pattern recognition methods were used. Since the PIV provides instantaneous information in the plane of illumination the decomposition of the equations of motion has to take advantage of this fact. The conventional Reynolds-averaging or double-decomposition (DD) of the equations of motion does not discriminate between coherent large-eddies and incoherent ones. It describes an instantaneous variable  $\xi$  in terms of its mean,  $\bar{\xi}$ , and a fluctuating  $\xi'$  components.

$$\xi(x, y, z, t) = \bar{\xi}(x, y, z) + \xi'(x, y, z, t) \quad (3)$$

In order to extract the coherent constituent of the signal from the stochastic background of a turbulent flow field one has to sample and compare the recurrent events that have a certain similarity. Pattern extraction from a sequence of sampled data can fulfill this requirement. Zhou *et al.* (1996), for instance, introduced a pattern recognition technique to provide detailed information about the mechanisms involved in a turbulent

energy cascade occurring in a plane wall jet. Their technique was tailored to the needs of processing temporal information generated at a single point in space (i.e. acquired by a hot-wire probe). The key to their method is the application of pattern extraction in the time (frequency) domain, where all the significant Fourier components of an individual realization were extracted from a relatively short sample of data instead of the entire duration of the available time series. Unfortunately, this technique is not suited for processing instantaneous information in space and only such information can currently be provided by a PIV. Therefore, the temporal type of triple decomposition, (TTD), had to be replaced by a spatial triple decomposition (STD) assuming that the flow is stationary. Regardless of the differences between the TTD and the STD, the traditional notation will be used for the triple-decomposition of an instantaneous variable  $\xi$ , as suggested by Hussain (1983)

$$\xi(x, y, z, t) = \bar{\xi}(x, y, z) + \tilde{\xi}(x, y, z, t) + \xi'(x, y, z, t) \quad (4)$$

and define the STD as

$$\xi(x, y, z, t) = \bar{\xi}(x, y, z) + \tilde{\xi}(x, y, z) + \xi'(x, y, z, t) \quad (5)$$

The first term on the right-hand side  $\bar{\xi}$  is the stationary component of the variable that  $\xi$ ,  $\langle \xi \rangle = \bar{\xi} + \tilde{\xi}$  that represents the sum of the stationary and the coherent components of  $\xi$  is defined differently for TTD and STD. In the former case the flow is usually artificially excited to provide a time reference signal. If the excitation is periodic  $\langle \xi \rangle$  represents the phase locked average; if the excitation is provided by a pulse then the time delay from the initiation of the pulse may be used to generate the ensemble average. Otherwise some temporal pattern recognition is required to be followed by VITA (variable integration time average) technique (see Blackwelder & Kaplan 1972). In the STD case a spatial pattern recognition method, that is analogous to the VITA technique has to be used. In both cases  $\xi'$  is the remainder and it represents the random (not recognized as coherent) constituent. As a consequence of the different decomposition and pattern recognition criteria, the various **coherent and random** constituents resolved by TTD and STD will be different. The reason for this is that the flow in TTD notation is viewed as by an observer fixed in space while in the STD notation, the observer moves with the core of the recognized structure (or in this case a streamwise vortex). The vortex core stands still and only its strength and its size varies in space. The advantage of this representation is obvious; it enables one to discriminate between the high frequency small scale turbulence and the low frequency meander of large longitudinal structures. The latter will appear in the second term on the right-hand side.

The following figures represent but a fraction of the actual measurement window selected for the sake of clarity. They represent an approximate spanwise domain  $\Delta z = 2.2y_2$  around the centerline of the cylinder (e.g. figure 13). The absolute width of the measured region was increased with increasing downstream location,  $\theta$ , to account for the growth of the structures and was equivalent on the average to  $\Delta z \approx 6y_2$ . The velocity vectors overlaid on top of the contours represent the sum of the stationary and coherent (thereafter referred to as S&C) ensemble averaged velocity vectors in the yz-plane (with the exception of figure 14). The profiles in the accompanying figures represent chosen cross sections through the counter-rotating vortices and between them as well as the spanwise averaged constituent of the quantity considered.

Figure 14(a) represents contours of ensemble averaged streamwise vorticity  $\langle \omega_x \rangle$  while the velocity vectors plotted superimposed on it represent the sum of the stationary mean radial velocity,  $\bar{v}/U_{\max}$ , and the radial velocity induced by the streamwise vortices,  $\tilde{v}$ . The sign of the latter depends on its spanwise location relative to a particular vortex core and it is capable of overwhelming  $\bar{v}/U_{\max}$  in the downwash region between the two vortices (marked by a  $\square$  in figure 13). To the left of the vortex rotating in a counter clockwise direction (i.e. containing  $\langle \omega_x \rangle > 0$ ), the downwash flow (where  $\bar{v}/U_{\max} < 0$ ) is brought to stagnation around  $y/y_2 = 0.3$  while to the right of it, it stops only at  $y/y_2 = 1.3$  (figure 13b). This is because the vortex-induced-flow changes its direction along the span while the mean outflow and inflow in

the wall and outer regions respectively are almost constant at all spanwise locations. Since the core of the average streamwise vortices is located at  $y/y_2 = 0.75$ , the interaction between the streamwise vortices and the mean flow is biased toward the inner region where  $y/y_2 \leq 1$ .

The purely coherent constituent of this flow is obtained by subtracting the stationary component  $\bar{v}/U_{\max}$  obtained by the simple averaging of the PIV data. Consequently, the spanwise-averaged coherent part of the radial velocity component,  $\tilde{v}$ , must vanish everywhere across the jet and it actually does so (figure 14b). Other plots of  $\tilde{v}$  across the cores of the vortices resemble the classical velocity distributions in a Rankine vortex that are dominated by a solid-body rotation within the core and a potential flow far from it.

In chapter 4 (figure 12) we presented the mean and fluctuating components of the cross flow velocities obtained by conventional double decomposition. This presentation lumped all the non-stationary data into one turbulent constituent. Therefore, double decomposition is not capable of distinguishing between typically random turbulence and the undulating, unsteady yet coherent flow (e.g. the longitudinal counter rotating structures discussed above). For example, because the mean velocities induced by the streamwise vortices change sign across each vortex the meander of these vortices results in a temporal variation of the local velocity field that contributes to the time dependent component or turbulence. In other words, vortices that are sufficiently unsteady so as not to cause spanwise variation in the mean flow simply contribute to the Reynolds stresses in the double decomposition (DD). For this reason, the turbulence intensities

$\sqrt{v'^2}/U_{\max}|_{DD}$  and  $\sqrt{w'^2}/U_{\max}|_{DD}$  attain excessive values in a spatially fixed coordinate system. If the data are to be decomposed into three constituents (stationary, coherent, and random), the random turbulence intensities,  $\sqrt{v'^2}/U_{\max}|_{STD}$  and  $\sqrt{w'^2}/U_{\max}|_{STD}$ , averaged along the span must be lower in comparison (figures 15b and 16b). The difference between the maxima obtained by the two methods of decomposition (DD & STD) is approximately 25% for both velocity components.

The highest intensity of the random,  $\sqrt{v'^2}/U_{\max}|_{STD}$  fluctuations measured relative to the core of the streamwise vortices occurs between the counter rotating pair of vortices that transports fluid from the surface outward (figure 15(a)  $y/y_2 = 0.9$ ;  $z/y_2 = \pm 1$ ), while the zone between the pair of vortices that transport fluid toward the surface contains a significantly lower level of random  $\sqrt{v'^2}/U_{\max}|_{STD}$  fluctuations ( $z/y_2 = 0$ ). The core of the streamwise vortices is rather quiescent regardless of the sign of their rotation. This suggests that differences among the individual vortices in terms of size and intensity contribute to  $\sqrt{v'^2}/U_{\max}|_{STD}$ . The selective location of the maximum in  $\sqrt{v'^2}/U_{\max}|_{STD}$  implies that the highest velocity fluid (that resides in the mean around  $y/y_2 = 0.2$ ) is pushed outward by the streamwise vortices increasing the local rate of strain at  $0.5 < y/y_2 < 1$  and thus turbulence production at this height above the surface. A similar correlation exists between the spanwise component of random fluctuations  $w'$  and the large streamwise vortices. The distribution of the secondary shear stress  $\overline{v'w'}/U_{\max}^2|_{STD}$  is not presented because of its extremely low levels. The intensity profiles shown in figures 15(b) & 16(b) represent a cross section through a core of the vortex and in the up-wash region between two vortices.

## 6. The Longitudinal Structures

Thus far, we have provided evidence for the presence of streamwise vortices in the turbulent curved wall jet. The next step is it to analyze their development in the direction of streaming and assess their size and strength. The best characterization of a vortex is by its circulation,  $\Gamma$ . If it is not altered by a specific mechanism, it should remain approximately constant throughout the flow. The circulation was determined by evaluating the surface integral of the streamwise vorticity field  $\omega_x$ . Vorticity values lower than 20% of the maximum were set to zero in order to reduce the influence of noise. Even at downstream locations

where the structures were relatively weak, this method provided stable and consistent results. Several convergence tests showed that the average of individual sub-samples (one third of the whole data record) typically agreed to within 5% with the result of the total record. Clockwise and counter-clockwise rotating vortices were averaged separately.

Four experiments were conducted at equally spaced downstream locations, ranging from  $\theta = 40^\circ$  to  $160^\circ$ . The results for both signs of the streamwise circulation  $\pm\Gamma_x$  are given in figure 17 using two definitions: (i) is the streamwise circulation per wavelength  $\pm\Gamma_{x,\lambda}$  and (ii) is the streamwise circulation per unit span  $\pm\Gamma_{x,\Delta z}$ . The circulation per unit span  $\pm\Gamma_{x,\Delta z}$  (labeled by open squares) stays approximately constant with increasing distance from the nozzle whereas the circulation per wavelength is doubled every  $\Delta\theta = 40^\circ$  (solid circles). A possible explanation for this increase is an amalgamation of vortices having the same sign. Consequently, the scale of the structures, but not their strength, increases proportionally to the width of the flow. This implies that the vortices observed are not amplified in the linear sense, but they do so due to vortex amalgamations that may represent a secondary instability. Earlier findings using cross-correlation measurements that (Likhachev, Neuendorf & Wygnanski) that were confirmed by the present PIV data (figure 18) support this notion. The results show that the spacing of the streamwise structures grows proportionally to the jet width. For the PIV data the mean spanwise spacing was calculated by dividing the span interrogated by the average number of the vortices identified.

The increase of the streamwise circulation  $\pm\Gamma_{x,\lambda}$  and the increase in  $\lambda_z$  with increasing distance from the nozzle is continuous (figures 17 and 18). This is in contrary to Plesniak's *et al.* (1994) observation that was made in a curved turbulent mixing layer. They describe a step-wise increase in spacing and in circulation. Such a behavior is known from mixing layers at low Reynolds number (Moser and Rogers, 1993). In fully turbulent flows a smooth development is more likely due to the meander of the structures and due to their variation in size and strength. In other words, in a fully turbulent flow (without external excitation), amalgamation of coherent structures can occur at any location and at any time. A regular and repeatable amalgamation of streamwise vortices is unlikely in a fully turbulent flow because clusters of positive and negative vorticity appear irregularly in space and time. Therefore, the row of vortices illustrated in figure 14 represents an average only.

More contours of the coherent streamwise structures measured at  $\theta = 40^\circ, 80^\circ, 120^\circ$ , and  $160^\circ$  are not plotted because they reveal little information. It is worth mentioning that the average distance of the vortex cores from the surface increases from  $0.7y_2$  at  $\theta = 80^\circ$  to approximately 1 at  $\theta = 120^\circ$ . This suggests that the vortex cores get squeezed out due to their growth in the fixed span experiment or they rotate outward with increasing distance in the direction of streaming. This rotation might be caused by the maximum velocity located at  $y/y_2 \leq 0.2$ , that advects the vorticity near the surface faster than the one away from it. Such rotation of the streamwise vortices, if it is proven to exist, would contribute to  $\Omega_y$  that might lead to the proposed cellular separation. The  $\theta = 120^\circ$  location coincides with the beginning of the adverse surface pressure region which leads eventually to the separation of the wall jet (see Neuendorf & Wygnanski (1999)).

## 7. Some Preliminary Effects of Two - Dimensional Excitation

When the flow emanating from the slot was excited in a two dimensional, harmonic manner, it triggered large spanwise eddies that crossed periodically a given streamwise location. Furthermore the forced input provided the phase reference (i.e. trigger input to the laser) required for phase averaging the data. This enabled one to examine the effect of periodic excitation on the large spanwise and streamwise vortices coexisting simultaneously in the flow. The distribution of spanwise vorticity and and streamwise velocity over the cylinder are provided by illuminating the flow in the  $(R,\theta)$  plane. Four phase locked and ensemble averaged spanwise vorticity contours,  $\langle\omega_z\rangle$ , are plotted in figure 19, together with the corresponding velocity profiles  $\langle u \rangle / U_{\max}$  measured at  $\theta = 80^\circ$ . They are separated by a phase difference of  $\Delta\phi = \pi/2$ . The mean velocity profile is plotted on the same figures for comparison. The maximum velocities at  $\phi = 0$  and  $\pi$  are approximately the same and they are equal to the mean maximum velocity,  $U_{\max}$ . The

streamlines that are superposed on the vorticity contours, converge toward the surface at  $\phi = 0$  and they diverge away from the surface at  $\phi = \pi$ . The flow accelerates between  $\phi = \pi/2$  and  $\phi = 3\pi/2$  increasing the rate of strain during this half of the forcing cycle and with it the absolute values of  $\|\langle \omega_z \rangle\|$  near the surface as well as in the outer region. The flow decelerates during the other half of the cycle with opposite effects on  $\|\langle \omega_z \rangle\|$ .

Illumination in the cross plane at  $\theta = 80^\circ$  provided phase locked data for the streamwise vortices discussed earlier. When these PIV results were processed through the pattern recognition and alignment procedure, regular arrays of counter rotating vortices emerged. Their contour plots are not shown because they do not differ from those plots shown in figures 13 through 16. At first sight the streamwise vortices appear to oscillate up and down at the frequency of excitation changing their core location from a minimum of  $y_{core}/y_2 = 0.55$  occurring at  $\phi = 0$  to  $y_{core}/y_2 = 0.8$  corresponding to  $\phi = \pi$  (figure 20). This correlates well with the divergence or convergence of the streamlines in the outer part of the wall jet where the cores of the streamwise vortices reside. Calculating the circulation in these streamwise vortices  $\Gamma_x$  per spanwise wavelength revealed that the latter is tied to the acceleration within the wall jet and has similar behavior to the maximum velocity (figure 20).

An example of the phase averaged streamwise vorticity is plotted in figure 20. The phase selected was,  $5\pi/4$  because then the large spanwise eddy just rolled over the illuminated plane at  $\theta = 80^\circ$  (figure 21c). This stretched and regulated the streamwise vortices that became apparent even in the absence of pattern recognition. Although the perceived intensity of the ensemble-averaged vortices is weaker and they seem to be stretched in the vertical direction, they provide clear evidence to the spanwise inhomogeneity in the flow. The weakness of the ensemble averaged contours stems in part from the dispersion in height of the various vortices relative to the surface. The histogram of vortex core locations above the surface is also shown in figure 21b suggesting that the mean location of the streamwise eddies is around  $y/y_2 = 0.7$ . The meandering of the streamwise vortices along the span is not stopped by the excitation since their preferred spanwise location changes depending on the phase at which the data was taken. Thus in the mean even the forced flow remains two-dimensional.

## 8. Summary and Conclusions

PIV measurements undertaken at several cross-sectional planes, ranging from  $\theta = 40^\circ$  to  $160^\circ$  revealed the existence of counter rotating vortex pairs in a wall jet flowing over a circular cylinder. Pattern recognition techniques had to be used in order to describe these vortices in a statistical manner and to separate the data into stationary, coherent, and random constituents. Freed from the high frequency background turbulence and their own low frequency meander, the vortices mapped provided a new insight into the effects of curvature and possibly centrifugal instability in highly turbulent shear flows. The results suggest that the longitudinal structures are not stationary and thus do not contribute to mean spanwise distortions, but they are strong enough to augment the Reynolds stresses and thus increase the rate of spread of the flow and its turbulent intensities. Their spanwise wavelength  $\lambda_x$ , might have determined the width of the jet as it was found to scale with the local width  $y_2$ , providing the relationship  $\lambda_x \approx 2y_2$ . Finally, the circulation of the individual structures  $\Gamma_{x,\lambda}$  doubled every  $\Delta\theta = 40^\circ$ , yet their number per unit span halved in each interval leaving the circulation per unit span  $\Gamma_{x,\Delta x}$  approximately constant. This would suggest that the vortices are increasing their strength through amalgamation and not through amplification, implying that a linear stability approach to their development may be wrong. Also the interaction between these streamwise vortices and the spanwise ones generated by a Kelvin-Helmholtz instability that was enhanced by periodic excitation was not a simple one, though it decreased the meandering of the former along the span. This interaction might be used in the future as a diagnostic tool.



## 9. References

- BLACKWELDER, R.F. and KAPLAN, R.E., 1972: "The intermittent structure of the wall region in a turbulent boundary layer". Proc. of the 12th IUTAM International Congress of Applied Mechanics Moscow
- BRADSHAW, P. 1969 Effects of streamline curvature on turbulent flow. *AGARDograph* 169.
- FEKETE, G.I. 1963 Coanda flow of a two-dimensional wall jet on the outside of a cylinder. Dept. of Mech. Eng., Rep. 63-11, McGill University.
- GASTER, M., & GRANT, T. 1975 An experimental investigation of the formation and development of a wave packet in a laminar boundary layer. *Proc. Roy Soc.* **347**, 253-269.
- GASTER, M., KIT, E. and WYGNANSKI, I., 1985 "Large-scale strictures in a forced turbulent mixing layer", *J. of Fluid Mech.*, **150**, 23-39.
- GUITTON, D.E. 1970 Some contributions to the study of equilibrium and non equilibrium turbulent wall jets over curved surfaces. PhD. Thesis Dept. of Mech. Eng., McGill University.
- HUSSAIN, A.K.M.F. 1983 Coherent structures - reality and myth. *Phys. Fluids* **26**, 2816.
- KROTHAPALLI, A., RAJKUPERAN, E., ALVI, F. & LOURENCO, L. 1999 Flow field and noise characteristics of a supersonic impinging jet. *J. Fluid Mech.* **392**, 155-181.
- LIKHACHEV, O., NEUENDORF, R. & WYGNANSKI, I. 2001, On streamwise vortices in a turbulent wall jet that flows over a convex surface. *Phys Fluids*. **13**, 1822-1825
- LOURENCO, L. & KROTHAPALLI, A. 1998 Mesh-free second order accurate algorithm for PIV processing. *PROC. Intl. Conf. On Optical Technology and Image Processing in Fluid, Thermal and Combustion Flows, Yokohama, Japan, December 1998*, 224
- MARGOLIS, D.R. & LUMLEY, J.L. 1965 Curved turbulent mixing layer. *Phys. Fluids* **8**, 1775-1784
- MATSSON, O.J.E. 1995 Experiment on streamwise vortices in curved wall jet flow. *Phys. Fluids* **8**, 2978-2988.
- NEUENDORF, R. & WYGNANSKI, I. 1999 On a turbulent wall jet flowing over a circular cylinder. *Jour. Fluid Mech.* **381**, 1-25
- OSTER, D., WYGNANSKI, I., DZIOMBA, B., FIEDLER, H., 1978 "The Effect of Initial Conditions on the Two-Dimensional ,turbulent Mixing Layer" in Structure and Mechanics of Turbulence, H. Fiedler ed. (Lecture Notes in Physics vol. 75, 48) Springer-Verlag, Berlin.
- PATEL, V.C. & SOTIROPOULUS F., 1997, Longitudinal curvature effects in turbulent boundary layers. , *Prog. Aerospace Sc.* **33**, 1-70.
- PLESNIAK, M.W., MEHTA, R.D. & JOHNSTON, J.P. 1994 Curved two-stream turbulent mixing layers: three-dimensional structure and streamwise evolution. *J. Fluid Mech.* **270**, 1-50.
- SCHUBAUER, G. B. and KLEBANOFF, P.S., 1956 Contributions to the mechanics of boundary layer transition, *NACA Report* number 1289
- SCHUBAUER, G. B. and SKRAMSTAD, H. K., 1948 "Laminar Boundary Layer Oscillations and Transition on a Flat Pate" NACA Rep 909.
- TANI, I., 1962: Production of longitudinal vortices in the boundary layer along a concave wall, *J. Geophys. Res.* **67**, 3075-3081.
- TOWNSEND, A.A., 1956, 1973 "*The structure of turbulent shear flows*" Cambridge University Press, London
- WYNGAARD, J.C., TENNEKES, H., LUMLEY, J.L. & MARGOLIS, D.P. 1968 Structure of Turbulence in a Curved Mixing Layer. *Phys. Fluids* **11-6**, 1251-1253.
- ZHOU, M.D., HEINE, Chr. & WYGNANSKI, I. 1996 The effect of excitation on the coherent and random motion in a plane wall jet. *J. Fluid Mech.* **310**, 1-37.
- ZILBERMAN, M., WYGNANSKI, I., and KAPLAN, R., 1977 "Transitional B.L. Spot in a Fully Turbulent Environment," *Physics of Fluids* **20**, 258-270.

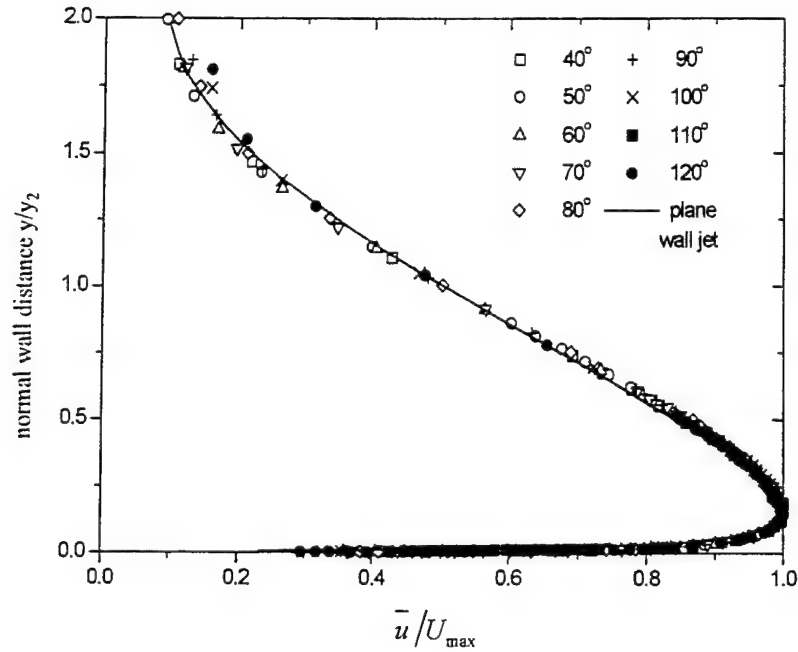


Figure 1: A comparison between mean velocity profiles in the constant pressure region of the curved and the plane wall jet. Scaled with the half width,  $y_2$  and  $U_{\max}$ . The Reynolds number  $Re_N = 33\,000$  and the slot width  $b = 2.34$  mm.

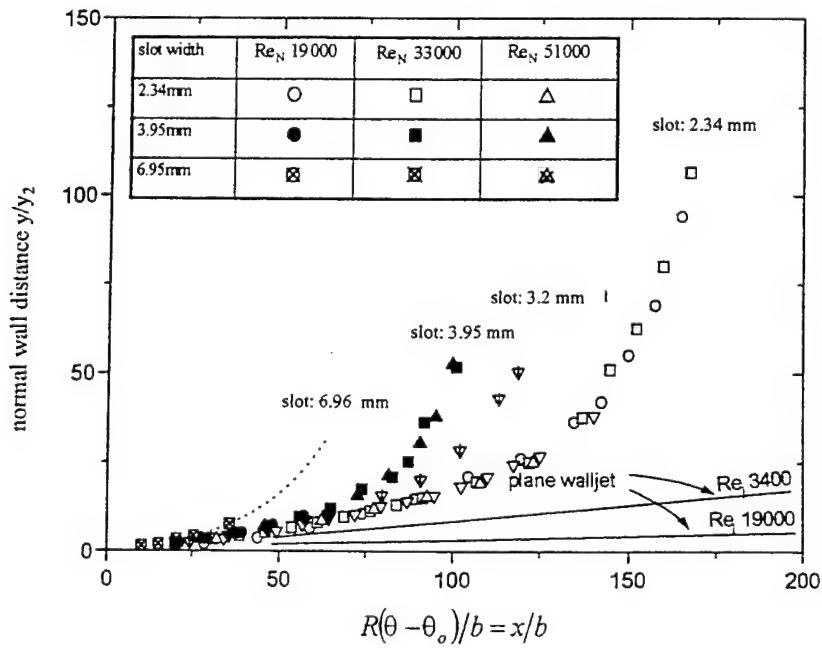


Figure 2: The radial rate of spread in the direction of streaming at various  $Re_N$ , ranging from 19 000 to 51 000. The scaling is based on the jet exit velocity  $U_{jet}$  and the slot width  $b$ .



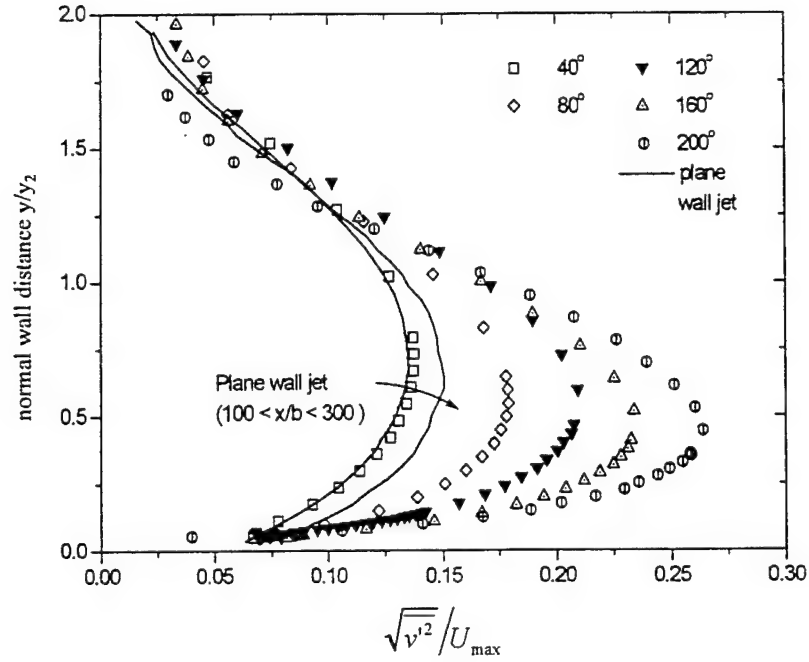


Figure 3: A comparison of the radial component of turbulence intensities in the plane and curved wall jet.

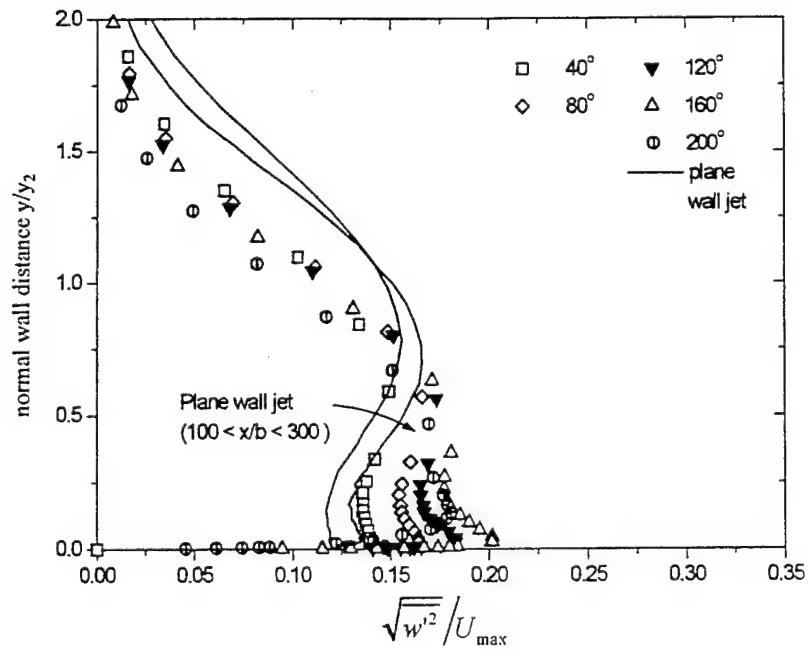


Figure 4: A comparison of the spanwise component of turbulence intensities in the plane and curved wall jet.

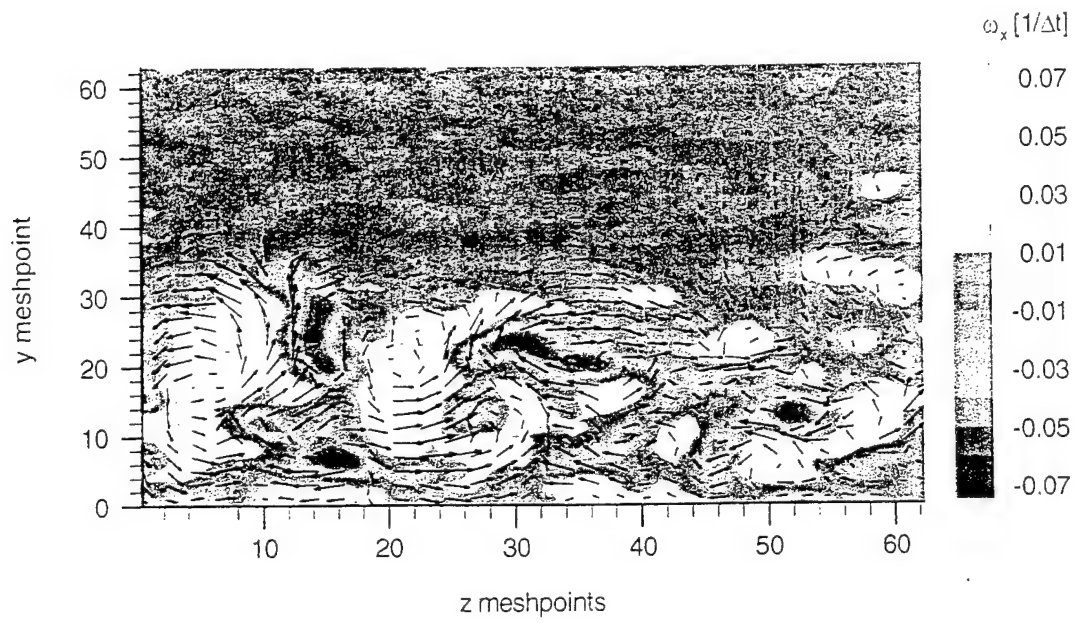


Figure 5: Vorticity contours of an instantaneous PIV image  $\omega_x(y,z)$

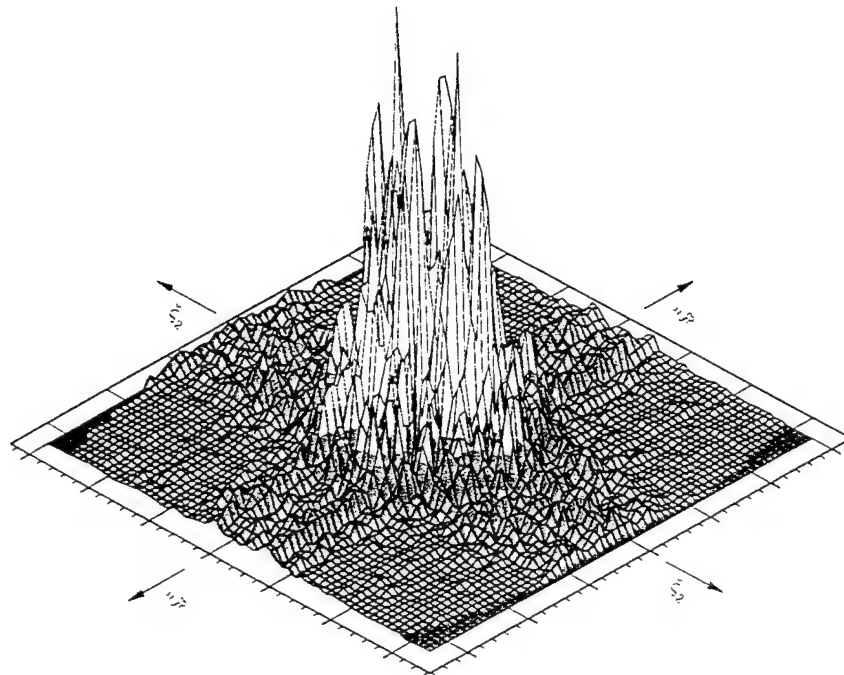


Figure 6: Fourier Transformation  $F(\zeta_2, \zeta_3)$  of the instantaneous PIV image  $\omega_x(y,z)$  (see figure 5)

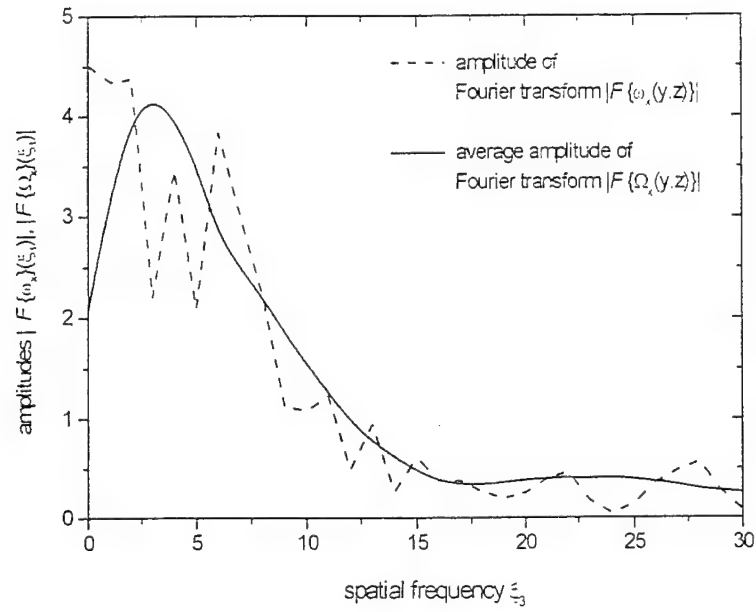


Figure 7: Amplitude of the Fourier transformation  $F(\zeta_2, \zeta_3)$  for positive  $\zeta_3$  and  $\zeta_2 = 0$

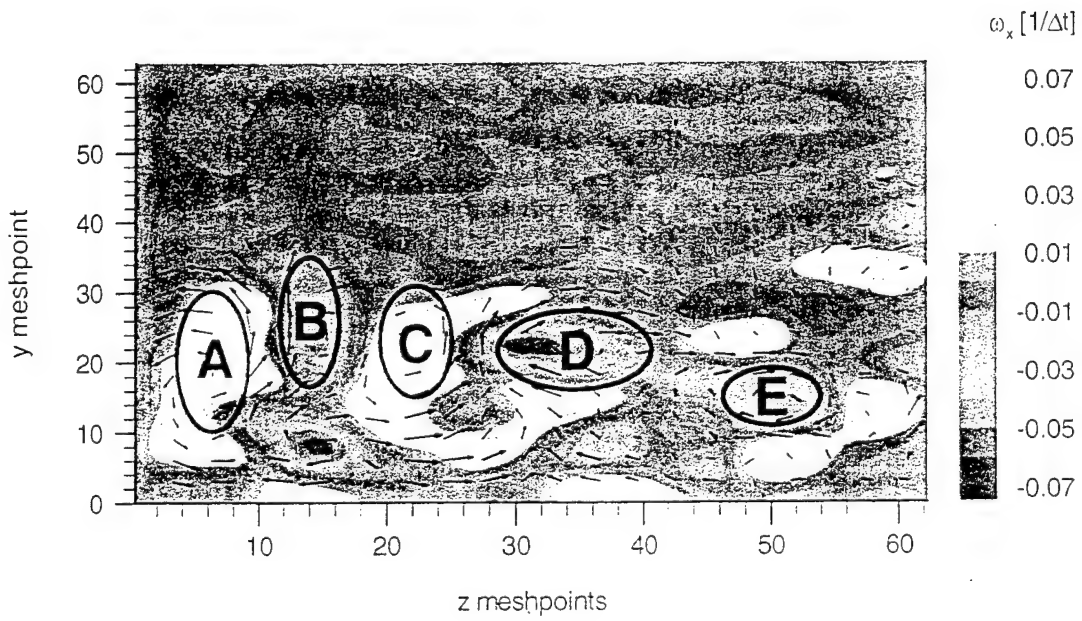


Figure 8: Low-pass filtered vorticity contours of an instantaneous PIV image  $\omega_x(y,z)$  (see figure 5)

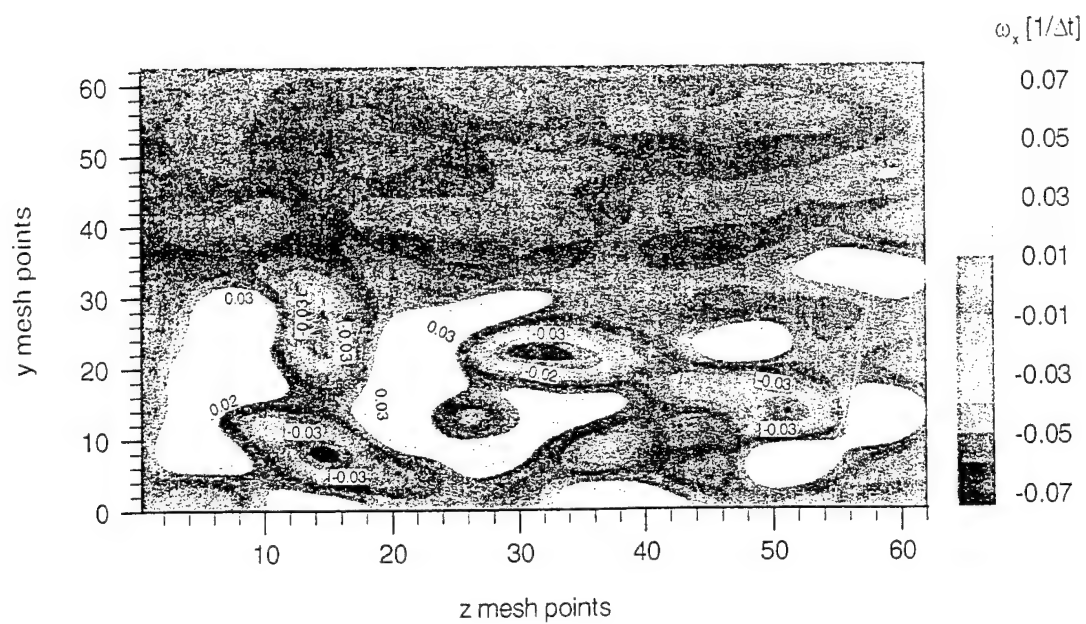


Figure 9: Low-pass filtered and threshold clipped vorticity contours of an instantaneous PIV image  $\omega_x(y,z)$  (see also figure 5 and 8)

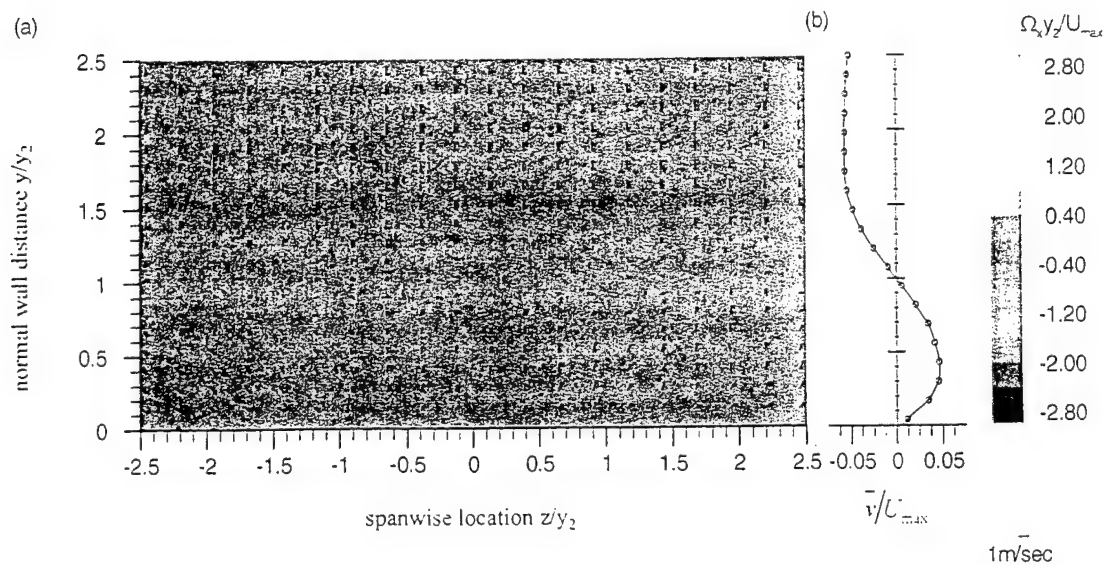


Figure 10: (a) Contours of streamwise mean vorticity  $\Omega_x y_2 / U_{max}$  and (b) the corresponding spanwise averaged radial velocity component  $\bar{v}/U_{max}$  at the downstream location  $\theta = 80^\circ$ .

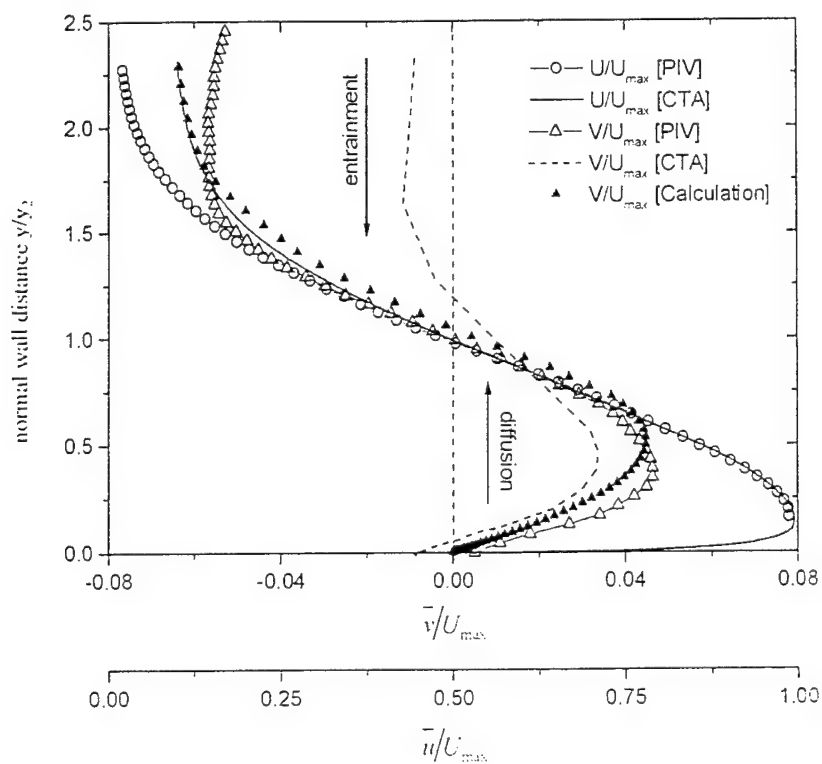


Figure 11: A comparison of hot-wire and PIV measurements at the downstream location  $\theta = 80^\circ$ .

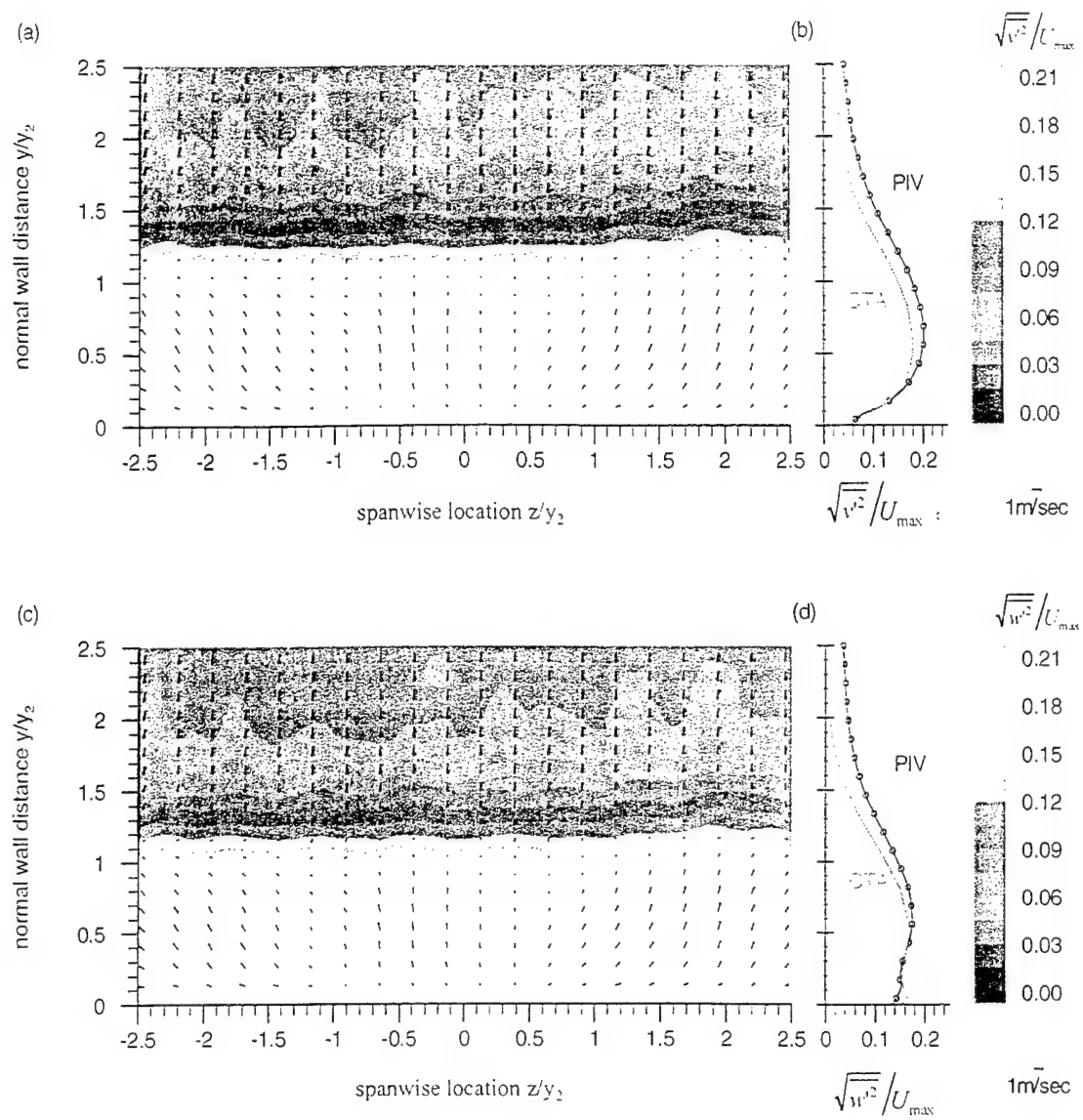


Figure 12: (a), (c) Turbulence intensity contours of the transverse Reynolds stresses  $\sqrt{\langle v'^2 \rangle} / U_{\max}$  and  $\sqrt{\langle w'^2 \rangle} / U_{\max}$  and (b), (d) the corresponding spanwise averaged turbulence intensity profiles at the downstream location  $\theta = 80^\circ$ .

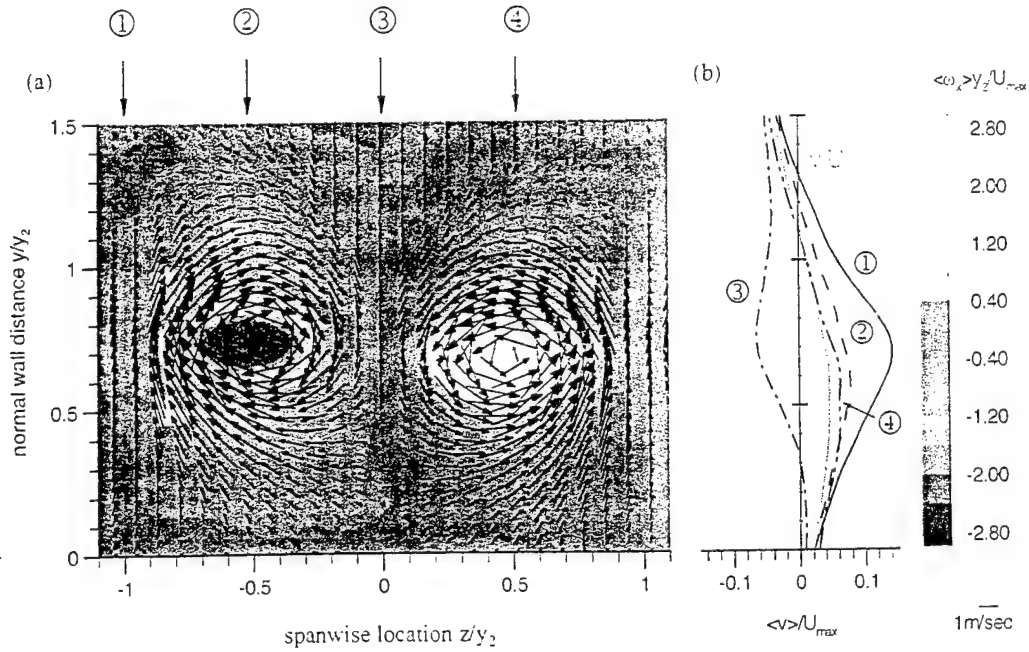


Figure 13: (a) Contours of phase averaged streamwise vorticity  $\langle \omega_x \rangle y_2 / U_{\max}$  and (b) the corresponding profiles of the spanwise averaged radial velocity component  $\langle v \rangle / U_{\max}$  at the downstream location  $\theta = 80^\circ$ . The profiles ① through ④ represent the phase averaged radial velocity components  $\langle v \rangle / U_{\max}$  at the cross sections  $z/y_2 = -1, 0.5, 0$ , and  $0.5$ , respectively.

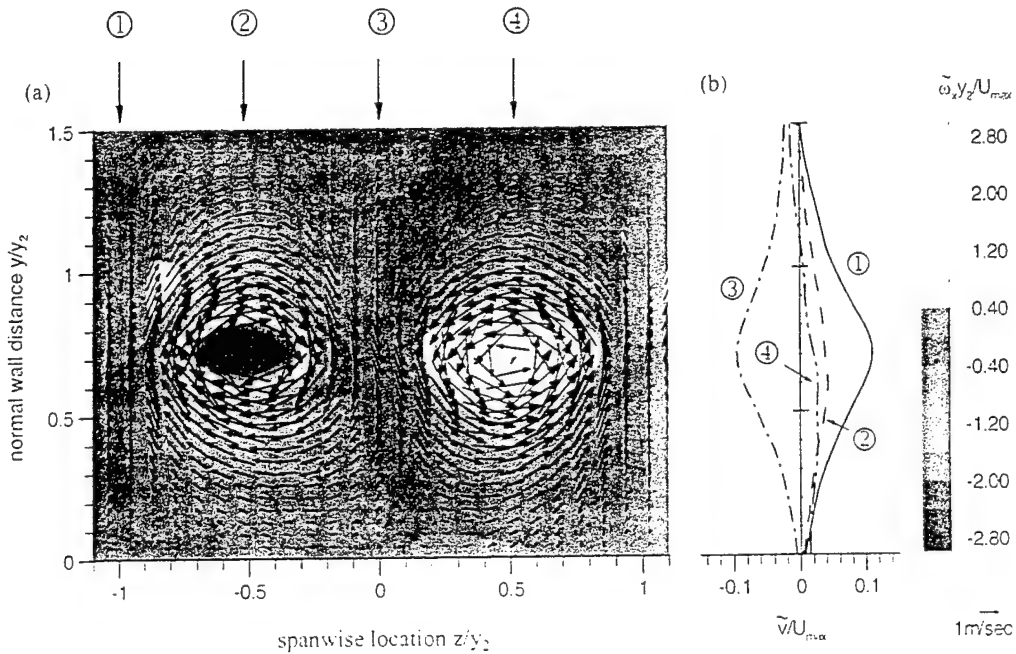


Figure 14: (a) Contours of coherent streamwise vorticity  $\tilde{\omega}_x y_2 / U_{\max}$  at the downstream location  $\theta = 80^\circ$ . The profiles ① and ④ represent the phase averaged coherent radial velocity components  $\tilde{v} / U_{\max}$  at the cross sections  $z/y_2 = -1, 0.5, 0$ , and  $0.5$ , respectively.

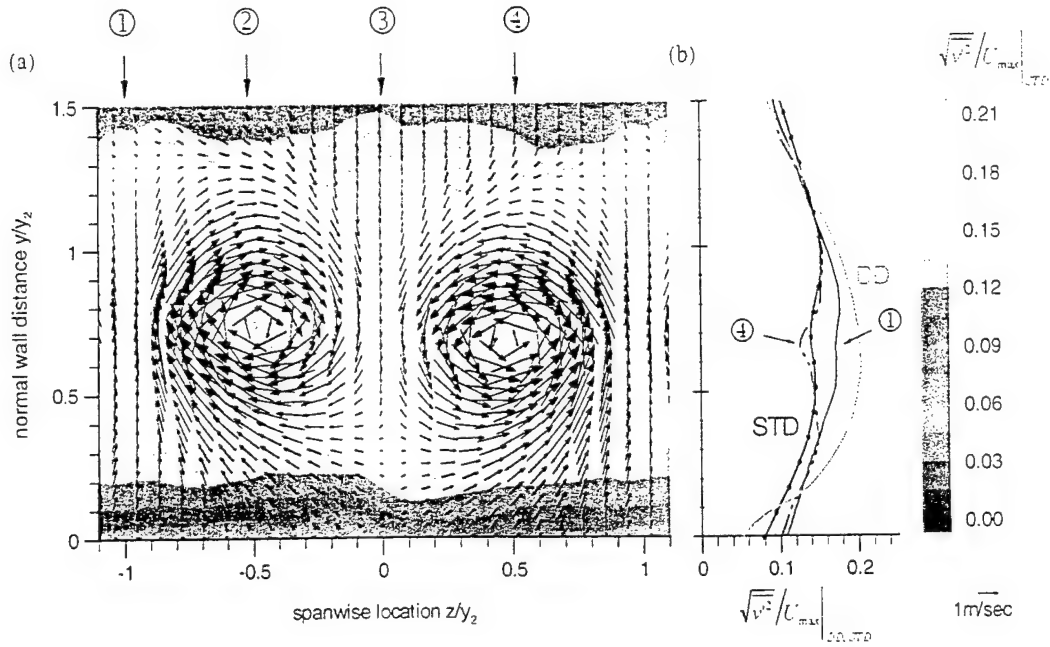


Figure 15: (a) Contours of the radial turbulence intensity component  $\sqrt{v'^2}/U_{max}|_{STD}$  for STD and (b) comparison of the corresponding spanwise averaged turbulence intensity profiles for STD and DD at the downstream location  $\theta = 80^\circ$ . The profiles ① and ④ represent the turbulence intensities for STD at the cross section  $z/y_2 = -1$  and  $0.5$ .

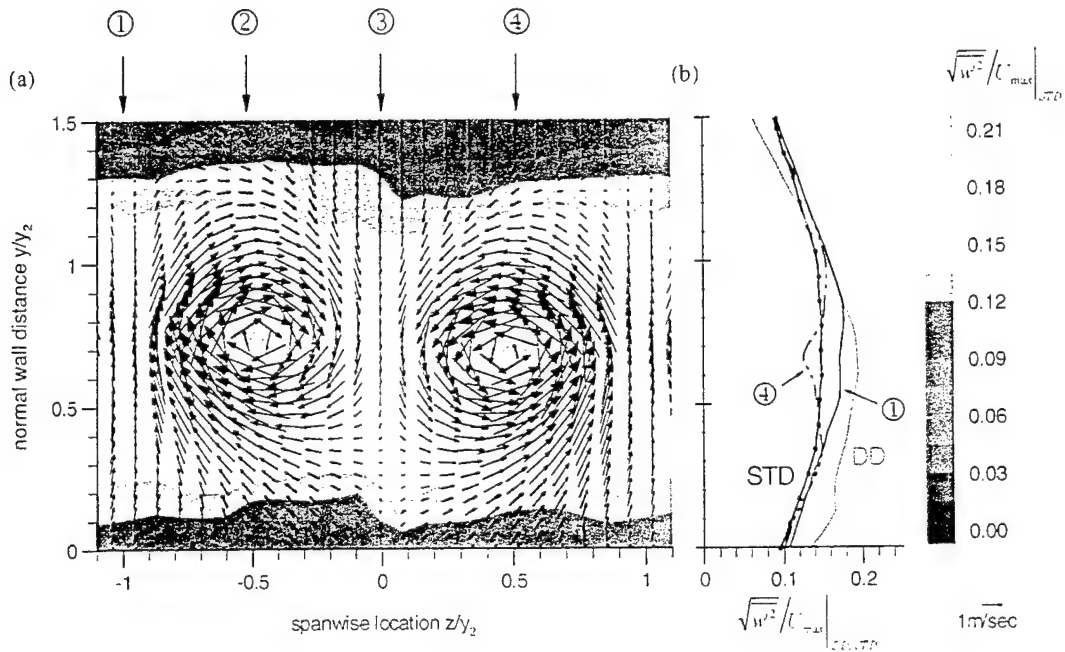


Figure 16: (a) Contours of the radial turbulence intensity component  $\sqrt{w'^2}/U_{max}|_{STD}$  for STD and (b) comparison of the corresponding spanwise averaged turbulence intensity profiles for STD and DD at the downstream location  $\theta = 80^\circ$ . The profiles ① and ④ represent the turbulence intensities for STD at the cross section  $z/y_2 = -1$  and  $0.5$ .



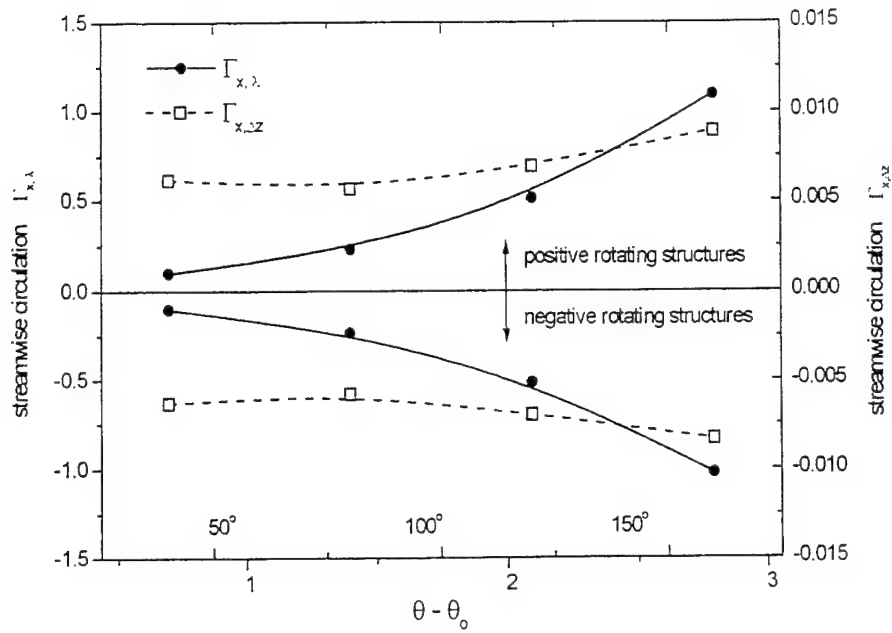


Figure 17: The development of the streamwise component of circulation  $\Gamma_x$  in the direction of streaming.

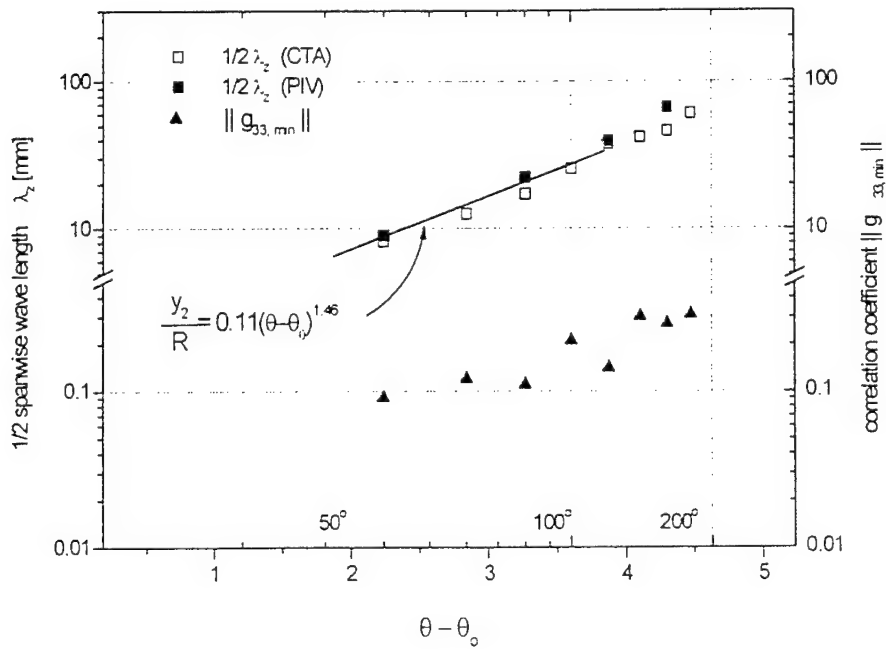


Figure 18: The development of the spanwise wave length  $\lambda_z$  and the minimum correlation Coefficient  $g_{33}$  in the direction of streaming.

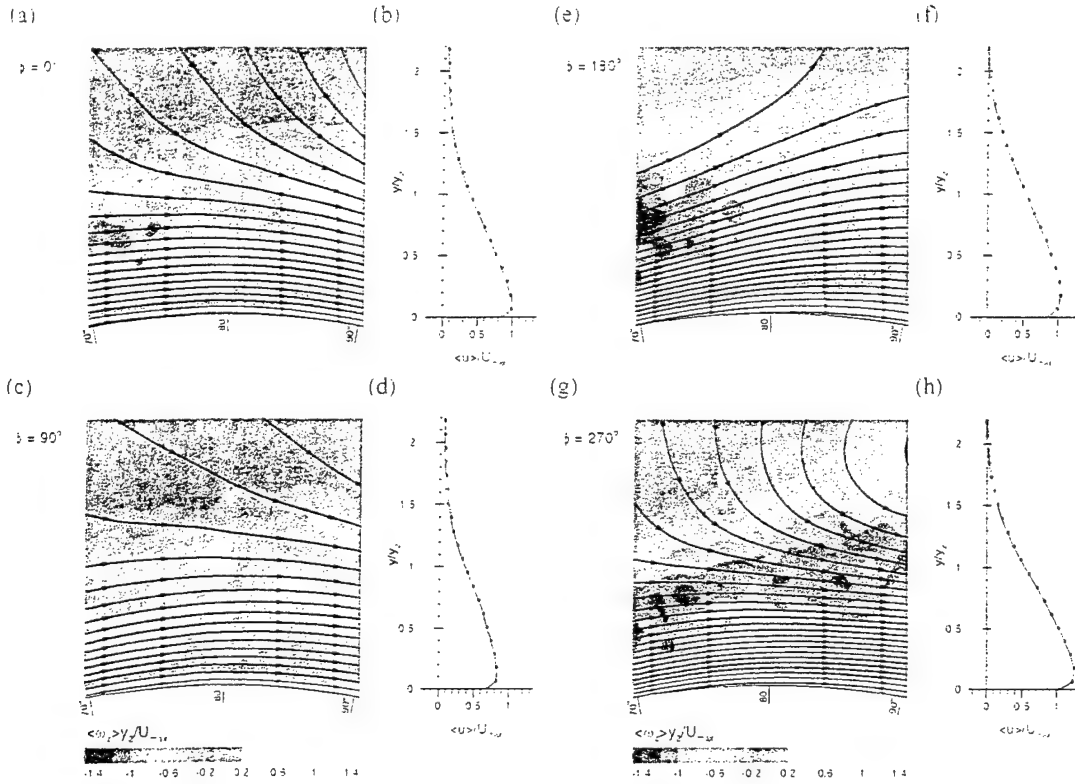


Figure 19: (a), (c), (e), and (g) Sequence of phase averaged spanwise vorticity contours  $\langle \omega_z \rangle y_2 / U_{\max}$  and (b), (d), (f), and (h) the corresponding profiles of the spanwise averaged radial velocity component  $\langle u \rangle / U_{\max}$  at the downstream location  $\theta = 80^\circ$  for  $\phi = 0, \frac{1}{2}\pi, \pi$ , and  $\frac{3}{2}\pi$ .

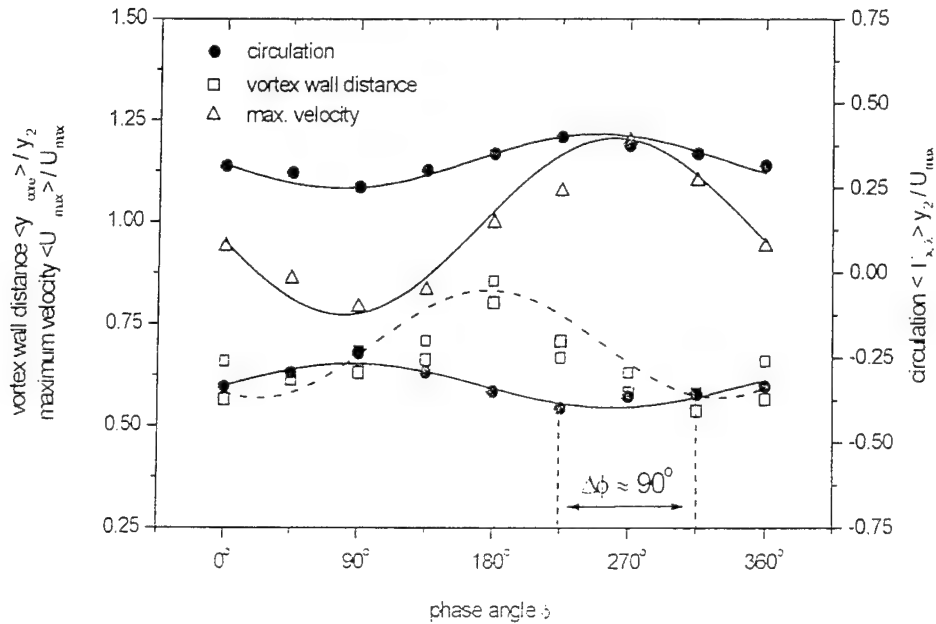


Figure 20: The development of the phase averaged vortex wall distance  $\langle y_{\text{core}} \rangle / y_2$ , the maximum phase average velocity  $\langle u \rangle_{\max} / U_{\max}$  and maximum phase averaged vorticity  $\langle \omega_z \rangle_{\max}$  with the phase angle  $\phi$ .

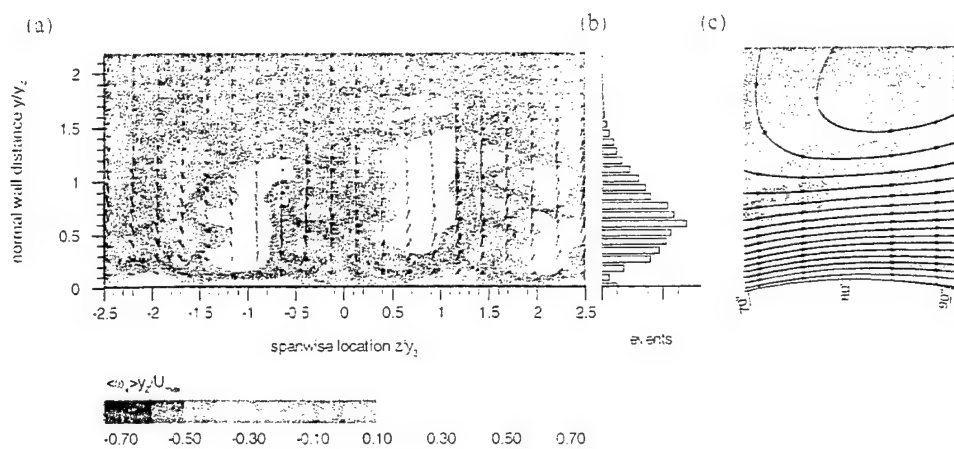


Figure 21: (a) Contours of phase averaged streamwise vorticity  $\langle \omega_x \rangle y_2 / U_{\max}$ , (b) core location probability distribution  $\langle y_{core} \rangle / y_2$ , and (c) contours of phase averaged spanwise vorticity  $\langle \omega_z \rangle y_2 / U_{\max}$  for  $\phi = 5/4\pi$  at the downstream location  $\theta = 80^\circ$  (without pattern recognition).

# A technical note on the ONR project N00014-99-1-0883

by  
Oleg Likhatchev

## Stability analysis of laminar and turbulent boundary layers with streamline curvature.

One notices a plethora of theoretical analyses devoted to the problem while reviewing the literature. However, the existing uncertainty in theoretical modeling of the Gortler instability and the obvious disparity between the theoretical predictions and experimental data forced me to develop my own model of the phenomenon. The existing approaches will not be reviewed. The analysis begins with the equations of continuity and motion in orthogonal body-oriented coordinate system

$$\begin{aligned} \frac{\partial u}{\partial x} + \frac{\partial hv}{\partial y} + \frac{h\partial w}{\partial z} &= 0 \\ u \frac{\partial u}{\partial x} + hv \frac{\partial u}{\partial y} + hw \frac{\partial u}{\partial z} + \frac{uv}{R} &= -\frac{\partial p}{\rho \partial x} + \nu \left\{ \frac{\partial^2 u}{h \partial x^2} + \frac{\partial}{\partial y} \left( h \frac{\partial u}{\partial y} \right) + h \frac{\partial^2 u}{\partial z^2} + O(R^{-2}) \right\} \\ u \frac{\partial v}{\partial x} + hv \frac{\partial v}{\partial y} + hw \frac{\partial v}{\partial z} - \frac{u^2}{R} &= -h \frac{\partial p}{\rho \partial y} + \nu \left\{ \frac{\partial^2 v}{h \partial x^2} + \frac{\partial}{\partial y} \left( h \frac{\partial v}{\partial y} \right) + h \frac{\partial^2 v}{\partial z^2} + O(R^{-2}) \right\} \\ u \frac{\partial w}{\partial x} + hv \frac{\partial w}{\partial y} + hw \frac{\partial w}{\partial z} &= -h \frac{\partial p}{\rho \partial z} + \nu \left\{ \frac{\partial^2 w}{h \partial x^2} + \frac{\partial}{\partial y} \left( h \frac{\partial w}{\partial y} \right) + h \frac{\partial^2 w}{\partial z^2} + O(R^{-2}) \right\} \end{aligned} \quad (1)$$

here  $h = 1 + y/R$ . There are two length scales that govern boundary layer type flows with streamline curvature: the radius of curvature  $R(x)$  and the boundary layer thickness  $\delta(x)$ . The ratio of these scales is the curvature parameter,  $\varepsilon = \delta/R$ , and usually is used as a small parameter in the order-of-magnitude analysis. The major assumption is that the centrifugal instability results in a *secondary steady flow* imposed onto the primary boundary layer. Analysis of this coherent steady small intensity motion can be carried out along lines similar to the regular similarity approach used for the initial boundary layer. Three-dimensional, steady, spatially growing disturbances imposed onto the mean flow have the form

$$\begin{aligned} (\tilde{u}, \tilde{v}) &= U_\infty \{ A(X) [\hat{u}(\eta), v(\eta)] + \varepsilon [\hat{u}_2(X, \eta), v_2(X, \eta)] + O(\varepsilon^2) \} \cos(\beta z) \exp \left( \int_{X_0}^X \hat{\gamma} dX \right) \\ \tilde{w} &= U_\infty [A(X) w(\eta) + \varepsilon w_2(X, \eta) + O(\varepsilon^2)] \sin(\beta z) \exp \left( \int_{X_0}^X \hat{\gamma} dX \right) \\ \tilde{p} &= (U_\infty)^2 [A(X) p(\eta) + \varepsilon \hat{p}_2(X, \eta) + O(\varepsilon^2)] \cos(\beta z) \exp \left( \int_{X_0}^X \hat{\gamma} dX \right) \end{aligned} \quad (2)$$

where  $dX = dx/R$ ;  $\eta, z$  are curvilinear coordinates at right angles to a fixed surface and in spanwise direction, made dimensionless with the length scale  $\delta(x) = C_\delta x^m$ ;  $U_\infty(x) = C_U x^n$  is the free-stream velocity;  $\hat{\gamma}$  the amplification rate, and  $\beta$  the dimensionless spanwise wavenumber. The only difference from the most advanced approach of Saric and Florian<sup>1</sup> is that at the first order of magnitude on the curvature

parameter the solution is assumed to be a self-similar one. It means that one should remember that  $\eta$  is an implicit function of  $x$ . Substituting the solution (2) into the linear perturbation equations in body-oriented co-ordinates and introducing the following transformations:  $u = \varepsilon \operatorname{Re} \hat{u}$ ,  $q = \operatorname{Re} p$ , and  $\gamma = \varepsilon \operatorname{Re} \hat{\gamma}$ ; one gets, at the leading order on the small parameter,  $\varepsilon \ll 1$ , the stability equations of the form

$$\begin{aligned} \gamma U u + Go^2 U' v + \operatorname{Re} V u' + \operatorname{Re} \delta / x U (2 m u - m \eta u') &= u'' - \beta^2 u \\ \gamma U v + \operatorname{Re} (V v)' + \operatorname{Re} \delta / x U (n v - m \eta v') - 2 U u &= -q' + v'' - \beta^2 v \\ \gamma U w + \operatorname{Re} V w' + \operatorname{Re} \delta / x U (n w - m \eta w') &= \beta q + w'' - \beta^2 w \\ \gamma u + Go^2 (v' + \beta w) + \operatorname{Re} \delta / x U (n u - m \eta u') &= 0 \end{aligned} \quad (3)$$

where the prime denotes derivatives with respect to  $\eta$ . It is well established that for both laminar and turbulent boundary layers  $V \propto \delta/x$ , while the product  $\operatorname{Re} \delta/x = \text{const.}$ . Hence, the set of equations (3) depend explicitly neither the coordinate  $x$  nor the Reynolds number. The modified amplification rate,  $\gamma = \gamma(\beta, Go)$ , is a function of the Gortler number,  $Go = \operatorname{Re} \sqrt{\varepsilon}$ , and the spanwise wavenumber,  $\beta = 2\pi/\lambda_z \cdot \delta$ . It is seen from (3) that the nonparallel effects are taken into account already at the first order of the small parameter  $\varepsilon$ . To validate the approach, a comparison was made between the theoretical predictions on the stability of the laminar boundary layer with respect to the centrifugal instability and available experimental data and is shown in Fig.1. The solid line represents the new theory and the dashed line is due to the classical Gortler theory that differs only slightly from the results of Saric and Florian<sup>1</sup> (they also considered nonparallel effects in the first order, but had taken into account only divergence of the mean flow). The new theory fits very well the data, since, contrary to the existing models, it predicts the "ideal" preferable spanwise wavenumber observed experimentally. In case of the laminar boundary layer a wavelength of Gortler's vortices is constant along the surface, hence, the perturbation downstream track in the stability diagram is represented by the line  $Go \propto \beta^{3/2}$ , shown by the dotted line. The similar calculations were done for the Stratford ramp flow for two cases: with a constant at given cross section of the boundary layer eddy viscosity evaluated from experimental data, and with the eddy viscosity as a function of the transfer coordinate obtained from the mean momentum equations, which are consistent with the data. The corresponding stability diagram is shown in Fig.2. The dotted line represents the parallel approach, the dashed line the new nonparallel model with a constant eddy viscosity, and the solid line corresponds to the new model with the non-constant eddy viscosity. The latter neutral curve only slightly differs from the one for the constant viscosity. The experimental observations of the Gortler vortices in turbulent boundary layers are also shown in the plot. The theoretical result is consistent with the observations. The majority of the studies reported observation of the structures at  $Go \approx 4$ . In our case of the Stratford ramp, the Gortler number varies along the test section in the diapason,  $Go = [0.8 : 2]$ , since the experimental turbulent Reynolds number is almost constant,  $Re \sim 37$ , and the measured curvature parameter along the surface is shown in Fig. 3, along with the corresponding radius of curvature. However, the amplification/decay rates of the perturbations are very small, it means that,

if some longitudinal vortices are embedded into the flow, they will be observed far downstream.

So, we have obtained the solution of the classical linear stability problem, at the lowest order on the small parameter  $\varepsilon$ . The amplitude function  $A(\kappa)$  is arbitrary at this order, however, it is determined by imposing the solvability condition at the next order. By using the notation

$$\{\varphi_{1j} : j = 1, \dots, 6\} \Rightarrow \{v, u, w, p, Du, Dv\} \quad (4)$$

equations (2) can be rewritten in the compact form

$$D\varphi_{1j} - \sum_{k=1}^6 a_{jk}\varphi_{1k} = 0 \quad \text{for } j = 1, \dots, 6 \quad (5)$$

where  $D = \partial/\partial\eta$ . Making use of (1) the next order problem is written as follows

$$D\varphi_{2j} - \sum_{k=1}^6 a_{jk}\varphi_{2k} = E_j(dA/dX) + G_j A \quad \text{for } j = 1, \dots, 6 \quad (6)$$

where the  $E_j$  and  $G_j$  are known functions of the mean flow quantities and the parameters of the external excitation. Since the homogeneous parts of (6) are the same as (5) and since the latter have a nontrivial solution, the inhomogeneous equations (6) have a solution if and only if the homogeneous parts are orthogonal to every solution of the adjoint homogeneous problem, that is

$$\int_0^\infty \sum_{j=1}^6 [E_j(dA/dX) + G_j A] \zeta_j^* d\eta = 0 \quad (7)$$

where the  $\zeta_j^*(\eta)$  are solutions of the adjoint homogeneous problem

$$\begin{aligned} D\zeta_j^* + \sum_{k=1}^6 a_{kj}\zeta_k^* &= 0 \quad \text{for } j = 1, \dots, 6 \\ \zeta_4^* = \zeta_5^* = \zeta_6^* &= 0 \quad \text{at } \eta = 0 \\ \zeta_4^*, \zeta_5^*, \zeta_6^* &\rightarrow 0 \quad \text{as } \eta \rightarrow \infty \end{aligned} \quad (8)$$

The equation for the amplitude  $A(X)$  comes from the solvability condition (7)

$$M(X)dA/dX + N(X)A = 0 \quad (9)$$

where

$$M(X) = \int_0^\infty \sum_{j=1}^6 E_j \zeta_j^* d\eta, \quad N(X) = \int_0^\infty \sum_{j=1}^6 G_j \zeta_j^* d\eta. \quad (10)$$

Thus an expression for the disturbances to leading order has the form

$$\tilde{q} \propto A_0 q(\eta) \exp \left[ \int_{X_1}^X (\hat{\gamma} - N/M) dX \right] \quad (11)$$

where  $q(\eta)$  is the eigenvector of the problem (5) is calculated for the given  $x$ -location and  $A_0$  is an arbitrary constant due to the linearity of the problem. One possible definition of the stability criteria is given by the value of the integrated energy of the downstream velocity perturbation across the flow. This integral, when obtained with the slightly divergent model, has the form

$$E(x) = \int_0^{\infty} E_0 |u(x, y)|^2 \exp \left\{ 2 \int_{x_1}^x \left[ \hat{\gamma}(x') - \frac{N(x')}{M(x')} \right] dx' \right\} dy. \quad (12)$$

The preliminary calculations were carried out for a constant Gortler number,  $Go = 4.4$ , and the initial dimensionless wavenumber  $\beta = 0.2$ . A downstream development of the energy  $u$ -component is shown in Fig. 4. The program is ready for a comparison of the calculated characteristics with experimental data.

## References

- <sup>1</sup> Floryan, J. M., and Saric, W. S., 1982, "Stability of Gortler Vortices in Boundary Layers," *AIAA Journal*, **20**, 3, p. 316.
- <sup>2</sup> Tani, I., 1962, "Production of Longitudinal Vortices in the Boundary Layer Along a Concave Wall," *Journal of Geophysical Research*, **67**, p. 3075.
- <sup>3</sup> Finnis, M. V., and Brown, A., 1989, "Stability of a Laminar Boundary Layer Flowing Along a Concave Surface," *Transactions of the ASME, Journal of Turbomachinery*, **11**, p. 376.
- <sup>4</sup> Winoto, S. H., and Crane, R. I., 1980, "Vortex Structure in Laminar Boundary Layers on a Concave Wall," *International Journal of Heat and Fluid Flow*, **2**, 4, p. 221.
- <sup>5</sup> Crane, R. I., and Sabzvari, J., 1984, "Laser-Doppler Measurements of Gortler Vortices in Laminar and Low-Reynolds-Number Turbulent Boundary Layers," *1st Int. Symp. on Applications of Laser-Doppler Anemometry to Fluid Mechanics, Lisbon*; also in *Laser Anemometry in Fluid Mechanics*, R. J. Adrian et al., eds., Ladoan-Inst. Sup. Tec., Lisbon, p. 19.
- <sup>6</sup> R. M. C. So and G. L. Mellor, 1975 "Experiment on turbulent boundary layers on a concave wall." *Aero. Q.* **26**, p. 25.
- <sup>7</sup> Barlow, R. S. and Johnston, J. P. 1988 "Structure of a turbulent boundary layer on a concave surface." *J. Fluid Mech.* **191**, p. 137.
- <sup>8</sup> Jeans, A. H. and Johnston, J. P. 1982 "The effects of concave curvature on turbulent boundary layer structure." *Rept. MD-40*. Thermosciences Div., Dept. of Mech. Engng. Stanford University.
- <sup>9</sup> Shizawa, T. and Horami, S. 1985 "Experiments on turbulent boundary layers over a concave surface - response of turbulence to curvature." Presented at the 5th Symposium on Turbulent Shear Flows, Cornell University, Ithaca, NY.
- <sup>10</sup> Muck, K. C. 1982 "Turbulent boundary layers on mildly curved surface." PhD thesis, Imperial College, London.
- <sup>11</sup> Jeans, A. H. and Johnston, J. P. 1983 "The effects of concave curvature on turbulent boundary layer structure." *IUTAM Symposium on Structure of Complex Turbulent Shear Flow* (ed. R. Dumas and L. Fulachier), p. 89. Springer.

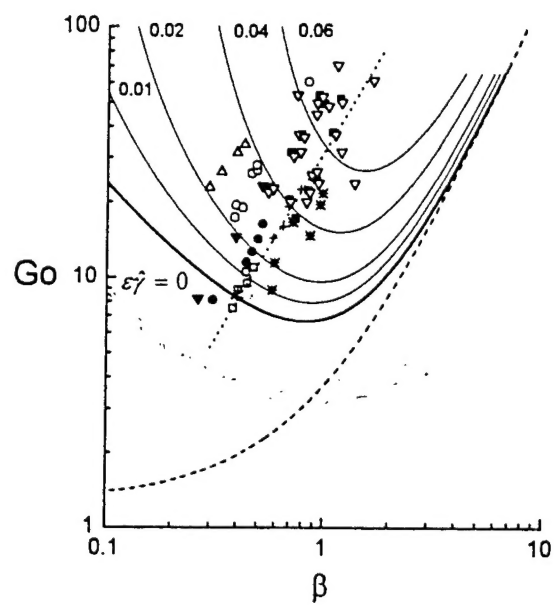


Fig. 1

- Gortler's approach
- the present model
- , • , ▼ , ○ , △ - Tani (1962)
- ✕ , + - Finnis & Brown (1989)
- - Winoto & Crane (1980)
- ▼ - Crane & Sabzvari (1980)
- .....  $Go \sim \beta^{3/2}$



# Stratford Ramp

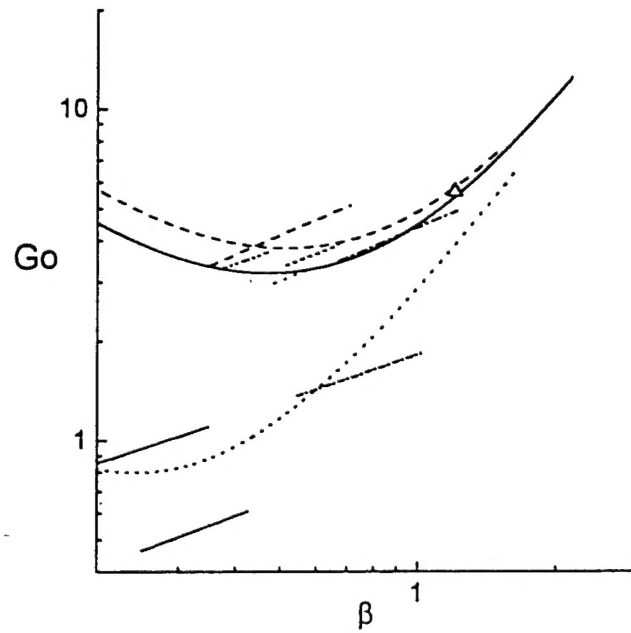


Fig. 2

- ..... Parallel
- Non-parallel
- So & Mellor (1975)
- So & Mellor (1978)
- Shizawa & Honami (1985)
- Jeans & Johnston (1982,1983)
- Barlow & Johnston (1985)
- Tani (1962)
- Tani (1962)
- Muck (1982)
- Nonparallel with Eddy Viscosity
- △ DNS (Zhang and Fasel, 1999)

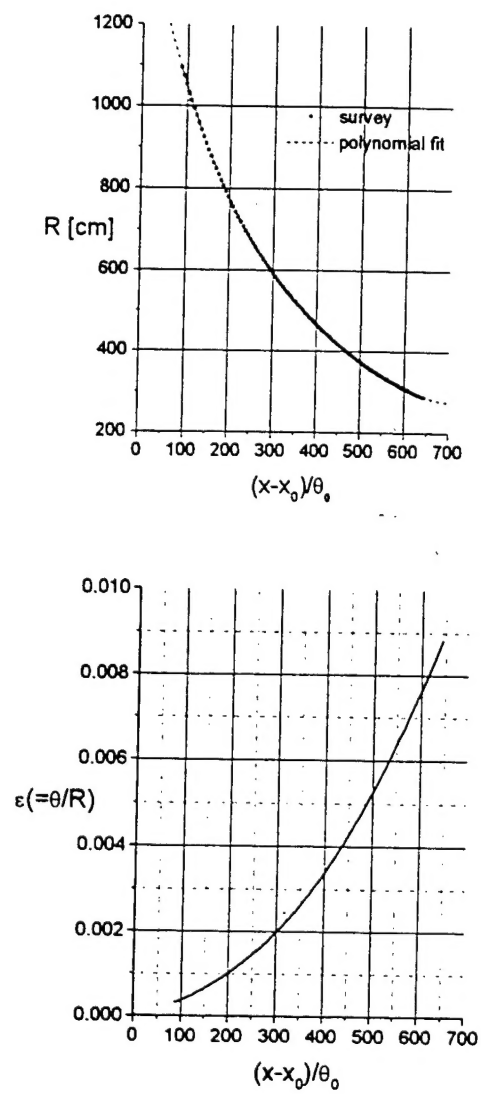


Fig. 3

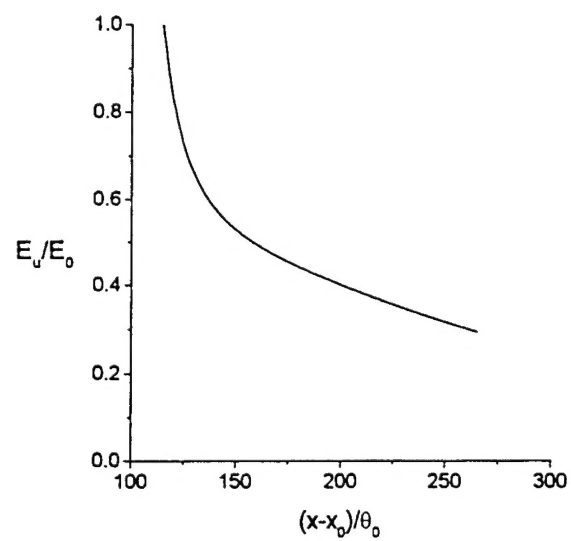


Fig.4